

REPORT DOCUMENTATION PAGE					<i>Form Approved OMB No. 0704-0188</i>	
<small>The public reporting burden for this collection of information is estimated to average 1 hour per response, including the time for reviewing instructions, searching existing data sources, gathering and maintaining the data needed, and completing and reviewing the collection of information. Send comments regarding this burden estimate or any other aspect of this collection of information, including suggestions for reducing the burden, to Department of Defense, Washington Headquarters Services, Directorate for Information Operations and Reports (0704-0188), 1215 Jefferson Davis Highway, Suite 1204, Arlington, VA 22202-4302. Respondents should be aware that notwithstanding any other provision of law, no person shall be subject to any penalty for failing to comply with a collection of information if it does not display a currently valid OMB control number.</small> PLEASE DO NOT RETURN YOUR FORM TO THE ABOVE ADDRESS.						
1. REPORT DATE (DD-MM-YYYY) 20-10-2011		2. REPORT TYPE Final Performance Report			3. DATES COVERED (From - To) From 21-03-2008 To 20-10-2011	
4. TITLE AND SUBTITLE DEVELOPMENT AND SIMULATION STUDIES OF A NOVEL ELECTROMAGNETICS CODE					5a. CONTRACT NUMBER	
					5b. GRANT NUMBER FA9550-08-1-0160	
					5c. PROGRAM ELEMENT NUMBER	
6. AUTHOR(S) Dr. Mark Hess					5d. PROJECT NUMBER	
					5e. TASK NUMBER	
					5f. WORK UNIT NUMBER	
7. PERFORMING ORGANIZATION NAME(S) AND ADDRESS(ES) INDIANA UNIVERSITY RESEARCH FOUNDATION Indiana University, 205C Bryan Hall, 105N Indiana Ave., Bloomington, IN 47405-1106					8. PERFORMING ORGANIZATION REPORT NUMBER	
9. SPONSORING/MONITORING AGENCY NAME(S) AND ADDRESS(ES) AFOSR / RSE 875 North Randolph Street, Suit 325 Room 3112 Arlington, Virginia 22203-1768					10. SPONSOR/MONITOR'S ACRONYM(S) AFOSR / RSE	
					11. SPONSOR/MONITOR'S REPORT NUMBER(S) AFRL-OSR-VA-TR-2012-0915	
12. DISTRIBUTION/AVAILABILITY STATEMENT 1) DISTRIBUTION STATEMENT A: Approved for public release; distribution is unlimited						
13. SUPPLEMENTARY NOTES						
14. ABSTRACT This is the final performance report for our grant entitled "Development and Simulation Studies of a Novel Electromagnetics Code". The main purpose of this research program is to develop novel simulation tools for the design and study of high-power microwave sources. One of the most challenging aspects of high-power microwave source physics is understanding and correctly modeling the generation and subsequent effects of spacecharge fields in the source. The accurate modeling of these fields is one of the key components of this research program. Moreover, the subject of high-power microwave sources, as a whole, has been of great interest and value to the Air Force for many years. Hence, this research program is of great relevance for the Air Force.						
15. SUBJECT TERMS DEVELOPMENT AND SIMULATION STUDIES OF A NOVEL ELECTROMAGNETICS CODE						
16. SECURITY CLASSIFICATION OF:			17. LIMITATION OF ABSTRACT UU	18. NUMBER OF PAGES	19a. NAME OF RESPONSIBLE PERSON John W. Luginsland, RSE (Program Manager)	
a. REPORT U	b. ABSTRACT U	c. THIS PAGE U			19b. TELEPHONE NUMBER (Include area code) 703.588.1775	

Final Performance Report

AFOSR Grant Number: FA9550-08-1-0160

Grant Title: “Development and Simulation Studies of a Novel Electromagnetics Code”

**Grantee Institution: Indiana University, 205C Bryan Hall,
105N Indiana Ave., Bloomington, IN 47405-1106**

Principal Investigator: Mark Hess

I. Objectives

This is the final performance report for our grant entitled “Development and Simulation Studies of a Novel Electromagnetics Code”. The main purpose of this research program is to develop novel simulation tools for the design and study of high-power microwave sources. One of the most challenging aspects of high-power microwave source physics is understanding and correctly modeling the generation and subsequent effects of space-charge fields in the source. The accurate modeling of these fields is one of the key components of this research program. Moreover, the subject of high-power microwave sources, as a whole, has been of great interest and value to the Air Force for many years. Hence, this research program is of great relevance for the Air Force.

The research program has four facets:

1. Develop novel theoretical/numerical tools for modeling electromagnetic fields due to space-charge dominated electron beams in high-power microwave sources
2. Utilization of high-speed computational methods to maximize the computational efficiency of these algorithms
3. Benchmarking of these codes to determine the accuracy of the numerical methods as well as to identify the primary errors which are present in the methods
4. Training of graduate students in the techniques of theoretical/computational electromagnetics

II. Status of Effort

Within the past three years, we have made significant progress in our development/implementation/benchmarking of novel electromagnetic algorithms for use in high-power radiation source simulations. Specifically, we have successfully developed a state-of-the-art space-charge solver that can be utilized to model space-charge fields due to high-current electron beams in either cylindrical or rectangular waveguides. Such a formalism is ideally suited for modeling the drift sections of klystrons and the interaction regions of free electron lasers. This formalism is based on a time-dependent Green's function method, and has the primary advantage that it is dispersion free. Dispersion errors are commonly found in grid based electromagnetic solvers, such as the Yee algorithm, and can contribute to unwanted errors in simulations, such as numerical Cherenkov radiation. The reason why our method is dispersion free and does not suffer from these unwanted errors is because the Green's functions are constructed from solutions to the Helmholtz equation. Solutions of the Helmholtz wave equation have exactly the correct dispersion properties. Hence, any linear combination of these solutions, such as the Green's function, also has the correct dispersion properties. An additional advantage of our method is that since the Green's function is generated from delta function sources in time and space in the wave equation, it can be readily used to model the space-charge fields of arbitrarily small beam bunches. This is ideal for modeling small electron bunch lengths in klystrons, or even microbunching instabilities which are commonly found in free-electron lasers.

The two main challenging aspects of this work was the theoretical development of the Green's function method and the computational requirements for running Green's function based algorithms. In the course of this research program, we have discovered that the Green's function method, while extremely powerful for certain simplified conductor geometries, has the limitation that it is not apparent how to extend these methods to arbitrary conductor geometries. During this research program, we were able to develop and implement Green's function based schemes for circular and rectangular conductor pipe geometries. This has led to a highly accurate description of space-charge effects in these geometries, which has applications to a variety of high-power microwave source problems, such as beam dynamics in drift sections of klystrons. However, the problem of how to extend Green's function methods to conductor geometries, such as the A-6 magnetron, is still an open question. The computational requirements for this scheme have also shown to be quite challenging. Unlike in a typical grid based scheme which only utilizes the values of electric and magnetic fields, as well as charge density and current density, from the previous time step, the Green's function method uses the values of fields and charge and current densities from all previous points in time. These requirements lead to significant challenges on determining the optimum algorithm design.

Our significant accomplishments have led to the publication of a paper in IEEE Transactions on Plasma Science entitled "Exact Space-Charge Field Solutions for Cylindrically Symmetric Beam Currents in a Circular Conductor Pipe", the training of five graduate students in computational electromagnetics, and the completion of a Ph.D.

thesis of one graduate student, Chong Shik Park. Our specific scientific achievements include the development of space-charge field solvers for cylindrical and rectangular conductor geometries, and the benchmarking of these schemes. We have also developed a parallelized version of the cylindrical field solver method using MPI (Message Passing Interface) scheme. This enables our Green's function based algorithms to operate over a large number of simultaneous processors. Finally, we have also performed a novel calculation and initial numerical study of a dispersion free FEL (free-electron laser) model for beams in a rectangular waveguide. We believe that this result may be of great interest to the Air Force for future FEL applications.

III. Accomplishments/New Findings/Future Work

Throughout the course of our research program, we have made a number of important accomplishments regarding the development and implementation of novel space-charge field solvers. Our first major accomplishment was the theoretical development of the Green's function based algorithm. This work was largely outlined in our IEEE Transactions on Plasma Science publication in 2010, as well as Chong Shik Park's Ph.D. thesis. For a cylindrical conductor geometry, we were able to calculate the exact electromagnetic space-charge fields given an arbitrary cylindrically symmetric charge and current density, which satisfies the continuity equation. This work is an enormous theoretical feat, since it required the derivation of space-charge fields from arbitrary sources, which is a highly nonlinear problem. However, the beauty of this scheme is that by writing down the solution one can immediately implement it numerically to calculate the space-charge fields for a given charge and current density.

We utilized this scheme to investigate the space-charge fields of a bunched beam in a pipe, which was undergoing radial oscillations. These oscillations could be caused by a TM_{01} mode in the 1 GHz range having a characteristic transverse radial electric field of 14 MV/m, which is interacting with the beam. This calculation served two purposes, one it allowed us to explore the importance of fully electromagnetic space-charge field solvers versus electrostatic solvers, as well as to act as a benchmark between the electrostatic method and our electromagnetic Green's function method.

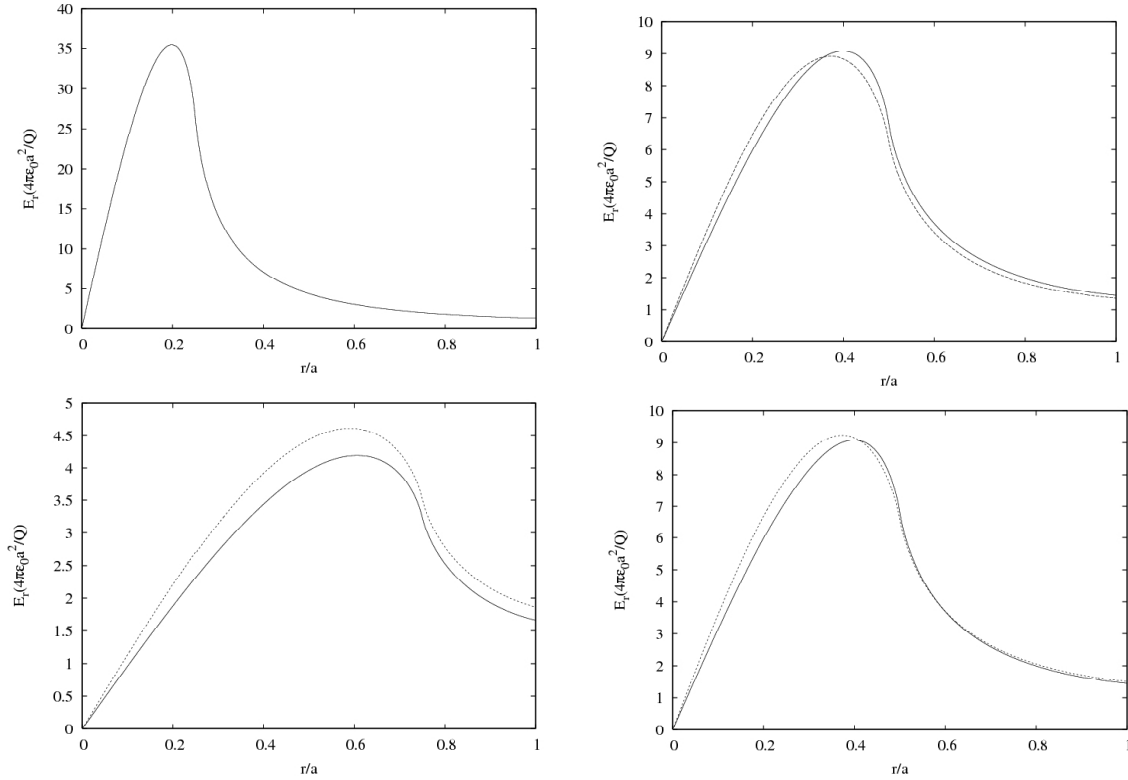


Figure 1

Figure 1 shows plots of the normalized radial electric field versus a normalized radius for the Green's function electromagnetic method (dotted) and a Green's function based electrostatic method (solid), at different points during the radial beam oscillation, $t=0$, $t=0.25T$, $t=0.50T$, and $t=0.75T$, where T is the period of oscillation. Details of the electrostatic model and the numerical calculation are given in our IEEE paper, as well as C.S. Park's Ph.D. thesis. We found for these parameters that the difference in electrostatic and electromagnetic space-charge methods can vary as much as 10%. This may be significant for problems involving space-charge dominated beam transport including high-current klystron beams in a drift section.

As mentioned before, the Green's function method has a significant challenge compared to other schemes, such as the Yee algorithm, in that it requires the calculation of integrals over charge and current densities for all previous time steps. This implies that for a large number of simulation time steps, N_T , the total computational time scales as N_T^2 . In order to improve the computational efficiency of this scheme, we developed a Green's function based algorithm which utilizes the Message Passing Interface (MPI) scheme.

The MPI scheme enables one to distribute the computational problem over many processors. The way we accomplished this is by implementing a grid into our code. The only purpose for this grid is to keep an inventory of the charge and current densities for all time. Since we are not solving the space-charge fields using a gridded algorithm, our code still maintains its dispersion free property. Each processor is "responsible" for a certain range of cells in the longitudinal direction. Specifically, each processor performs integrations over the charge and current densities in its range of cells. Figure 2 shows a plot of the speed up of the algorithm using the MPI scheme as a function of the number of processors. One can immediately see that we can achieve excellent performance with the MPI scheme, and the effects of crosstalk between processors does not seem to be a major limitation for our algorithm.

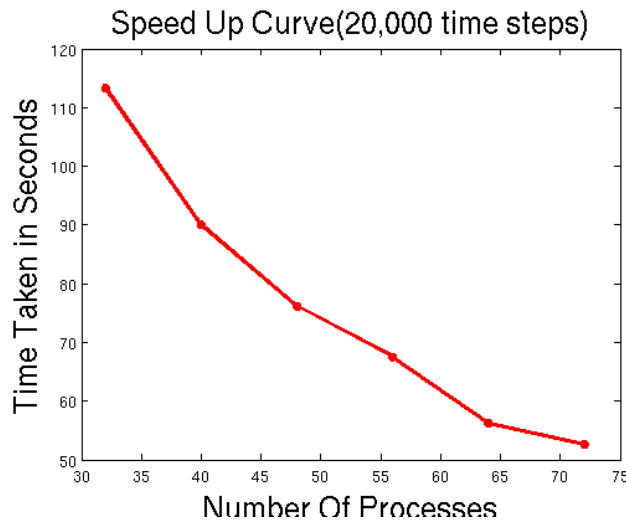


Figure 2

In addition, we have also recently tested the usage of Green's function based space-charge field solvers for modeling free electron laser systems within a rectangular waveguide structure. Specifically, we have developed a model for electron beam motion through an undulator magnet, and used our dispersion free methodology to calculate the space-charge fields within the beam. Figure 3 shows a simulation plot of the space-charge electric field in the x-direction for a highly relativistic electron beam moving in the z-direction with an energy of 17.5 GeV, a bunch charge of 1.0 nC, a bunch length of 25 μm , and a transverse emittance of 1.4 mm-mrad. The undulator magnet has a maximum magnetic field of 1.0 T and an undulator period of 35.6 mm. Although these initial code test parameters are associated with the design of a future X-ray FEL, such as the European XFEL experiment, it is straightforward to modify the parameters in our formalism to model millimeter wavelengths that are more pertinent to the Air Force. The space-charge field is plotted in the beam rest frame as a function of normalized x and z. Utilizing our dispersion free scheme, we are able to obtain highly accurate space-charge field calculations for FEL systems. This may prove very useful for future Air Force free electron laser design studies.

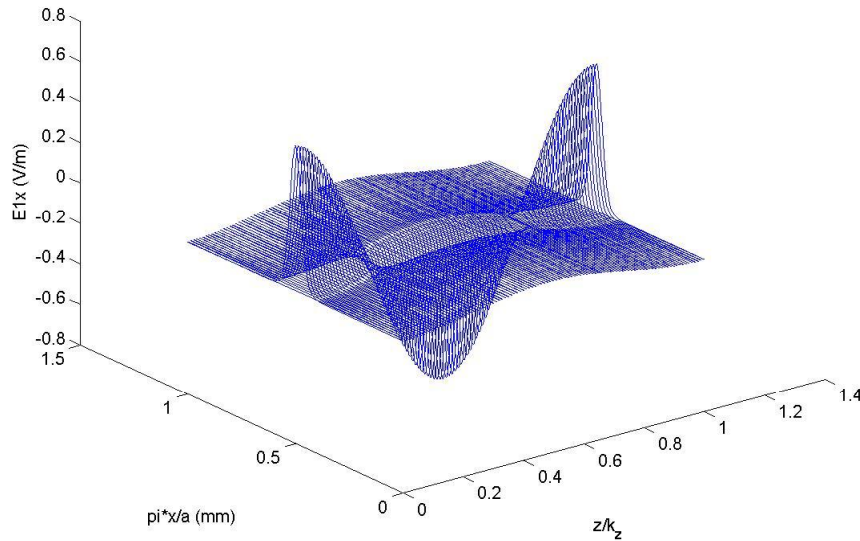


Figure 3

Finally, our research group has successfully utilized this project for the training of graduate students at Indiana University. This project has supported Chong Shik Park, who recently received his Ph.D. in 2009, Vivek Krishna, who received his M.S. degree in computer science, Abhijeet Kodgire who was a computer science student, Adarsh Yoga, who received his M.S. in computer science, and Rohith Goparaju, who received his M.S.

in computer science. Dr. Park was heavily involved in the development of the dispersion free theoretical methods and numerical implementation of these methods. Mr. Krishna was primarily involved in developing the grid-based algorithm for tracking beam charge and current densities while simultaneously utilizing our dispersion free methodology for computing the space-charge fields. A short time after Dr. Park and Mr. Krishna graduated we again utilized this grant to begin supporting two exceptional computer science graduate students, namely Adarsh Yoga and Abhijeet Kodgire. Mr. Yoga was responsible for benchmarking our dispersion free methods against a finite-difference-time-domain (Yee) method. Mr. Kodgire was responsible for implementing the MPI framework within the existing grid-based algorithm. Mr. Kodgire left our group in September 2010, and in January 2011, we began supporting Rohith Goparaju. Mr. Goparaju was responsible for completing the MPI implementation of our code.

IV. Personnel Supported

Each year this grant has included funding for one faculty member (M.Hess) for two months summer salary, as well as two graduate students, with stipend and fee remission. One graduate student supported by this grant, Chong Shik Park, has recently graduated with a Ph.D. in physics at Indiana University. Dr. Park was funded at the start of phase 1 on this grant until May 2010. Another graduate student supported by this grant, Vivek Krishna, has graduated with a M. S. degree in computer science. Mr. Krishna had been funded since the start date of Phase 2 of this grant, i.e. Jan. 1, 2009, and his support ended on May 2010. In May 2010, two additional graduate students in the computer science department were supported by this grant, Adarsh Yoga and Abhijeet Kodgire. In September 2010, Mr. Kodgire's support ended on this grant. In January 2011, another computer science student, Rohith Goparaju, was added to this grant. Mr. Yoga and Mr. Goparaju's support from this grant ended on May 2011.

V. Publications

Peer Reviewed Journals

M. Hess and C. S. Park, "Exact Space-Charge Field Solutions for Cylindrically Symmetric Beam Currents in a Circular Conductor Pipe", IEEE Trans. Plasma Sci., 38, pp. 1584-1591, 2010

Thesis

C.S. Park, "Investigations of Electromagnetic Space-Charge Effects in Beam Physics", Indiana University, Ph.D. Thesis 2009.

VI. Interactions/Transitions

a.

Talks:

M. Hess and C.S. Park, “Three-dimensional Space-Charge Modeling of Intense Beams in a Circular Conducting Pipe”, APS Division of Plasma Physics Meeting 2009.

M. Hess and C.S. Park, “Simulating Space-Charge Physics of High-Current Beams with a Green's Function Approach”, APS Division of Plasma Physics Meeting 2008.

Poster:

M. Hess, A. Yoga, R. Goparaju, V. Krishna, A. Kodgire, and C.S. Park, “Development and Benchmarking of a Novel Grid Based Space-Charge Field Solver”, International Conference on Plasma Science 2011.

M. Hess, C.S. Park, V. Krishna, and A. Kodgire, "A Dispersion Free Method for Modeling Space-Charge Physics in a Circular Pipe", International Conference on Plasma Science 2010.

M. Hess, “A Dispersion Free Methodology for Modeling Intense Charged Particle Beams”, APS Division of Plasma Physics Meeting 2010.

M. Hess and C.S. Park “A Dispersion Free Three-Dimensional Space-Charge Modeling Method”, Particle Accelerator Conference 2009.

b. There were no consultative or advisory functions to other laboratories or agencies performed.

c. There were no technology assists, transitions, or transfers performed.

VII. New Discoveries / Inventions / Patent Disclosures

None.

VIII. Honors/Awards

None.

INVESTIGATIONS OF ELECTROMAGNETIC SPACE-CHARGE EFFECTS IN BEAM PHYSICS

Chong Shik Park

Submitted to the faculty of the University Graduate School
in partial fulfillment of the requirement
for the degree
Doctor of Philosophy
in the Department of Physics,
Indiana University

December 2009

Accepted by the Graduate Faculty, Indiana University, in partial fulfillment of the requirement for the degree of Doctor of Philosophy.

Doctoral
Committee

Mark H. Hess, Ph.D.

Shyh-Yuan Lee, Ph.D.

Steven A. Gottlieb, Ph.D.

August 24, 2009

Rex Tayloe, Ph.D.

Copyright ©2009 by
Chong Shik Park
ALL RIGHTS RESERVED

*To My Parents,
Soon Lim Hur and Hee Jin Park*

Acknowledgments

Looking back on my graduate school experience, I realize that I could not have reached this point without all the help that I have received in the process.

First and foremost, my deepest gratitude must go to my advisor Professor Mark Hess, for his steadfast support and guidance of this dissertation study. I cannot thank him enough for the academic training and encouragement that I got from him through all the phrases of my graduate school life. He is one of the greatest physicists who I have ever known. From him, I learned his enthusiasm for the field of physics. I am also thankful for his kindness and patience in correcting my English.

I would like to extend my deepest gratitude to Professor S.Y. Lee for his valuable advice in my research and various aspects of life as a physicist. His brightness in Accelerator Physics has encouraged me to study more. I am also thankful to Professor Steve Gottlieb and Professor Rex Tayloe for serving as my dissertation committee members and for reading my humble thesis.

I thank Dr. John Power and Dr. Wei Gai at Argonne National Laboratory, for their informative discussions and helpful supports on my study of the ANL AWA rf photoinjector. More thanks to all the instructors from USPAS (United States Particle Accelerator School). From the training in USPAS, I learned various fields of Accelerator Physics, which had made me more brilliant.

I also thank my fellow graduate students in the Accelerator Physics Group at Indiana University, especially, Dr. Lingyun Yang, Waiming Tam, and Jeff Kolski. I will never forget the fun and happy moments we studied together and discussed our field. I would like to thank my best friends from South Korea: Dr. Seung-Ku Lee, Professor Kwonbum Jung, and Jang-Il Kim. They encouraged me and made me feel happy from a distance, either from South Korea or from another state in the US.

I would like to thank my family for their enormous support and constant encouragement. My parents have always supported me and shown their trust in me ever since I can remember. Special thanks to my proud sister, Sun Jae and her family, who helped me with all kinds of big and small things. I know I cannot thank my family enough for their endless love in this limited space. However, I will show my gratitude by making my dream come true afterwards.

Very Special thanks to my beloved, Hyun-jin Kim, for her love and supports. Without her supports, I could not have completed my graduate study in Bloomington. She always made me proud of being her boyfriend.

Chong Shik Park

INVESTIGATIONS OF ELECTROMAGNETIC SPACE-CHARGE EFFECTS IN BEAM PHYSICS

In order to achieve high quality charged particle beams for electron sources, such as rf photoinjectors, and high-power microwave sources, such as klystrons, the effects of space-charge need to be addressed. In these systems, the beam energy is relatively low while the beam charge is relatively high leading to important space-charge physics. While there have been a number of previous works which have analyzed the physics of space-charge, most of these studies have looked at the problem assuming that the space-charge physics was either purely electrostatic so that analytical techniques could be applied or fully electromagnetic using only computational methods, such as the Yee-PIC algorithm, for simulating these effects. The present study is unique in that it incorporates novel theoretical techniques using time-dependent Green's functions for computing the fields and modeling the space-charge physics analytically and numerically.

This work presents the calculations of time-dependent electromagnetic space-charge fields for a perfectly conducting pipe with and without a cathode. Using a Lorenz gauge formalism within Maxwell's equations, the beam space-charge fields are computed from a time-dependent Green's function method. In this method, the correct conductor boundary conditions are implemented such that the effects of image charges and image currents due to the cathode and cavity walls are included.

In order to simulate the beam dynamics and electromagnetic space-charge effects in the rf photocathode gun, a new code called IRPSS (Indiana Rf Photocathode Source Simulator), has been developed. The results of IRPSS are compared with

electrostatic codes, such as a time-independent Green's function based space-charge algorithm, as well as known beam physics codes, such as PARMELA. We highlight the important numerical challenges and computational limits which we have analyzed during the development of IRPSS. In addition, we compare IRPSS results to an experimental beam loss measurement performed on the Argonne Wakefield Accelerator rf photocathode gun.

We also show how the code can be extended to include important physics for beams with non-negligible transverse currents, such as those found in high-power microwave sources.

Mark H. Hess, Ph.D.

Shyh-Yuan Lee, Ph.D.

Doctoral
Committee

Steven A. Gottlieb, Ph.D.

August 24, 2009

Rex Tayloe, Ph.D.

Contents

Acceptance	ii
Acknowledgments	v
Abstract	vii
1 Introduction	1
1.1 RF Photoinjector	3
1.2 Main Contributions of the Thesis	5
1.3 Outline of the Thesis	7
2 Theoretical Space-Charge Modeling	9
2.1 Existing Space-Charge Algorithms	10
2.1.1 SCHEFF Algorithm (PARMELA and ASTRA)	10
2.1.2 Lienard-Wiechert Potentials (TREDI)	13
2.1.3 Yee/PIC Method (MAFIA)	14
2.2 Green's Function Approaches	16
2.2.1 Mode Analysis and Series Expansions	16
2.2.2 Analytical Method with Green's Function	18
3 Space-Charge Modeling of the RF Photoinjector	19

3.1	Electromagnetic Space-Charge Potentials and Fields	19
3.1.1	Arbitrary Pipe Cross-Section with Longitudinal Currents . . .	22
3.1.2	Circular Pipe Cross-Section with Longitudinal Currents . . .	27
3.1.3	Rectangular Pipe Cross-Section with Arbitrary Currents . . .	31
3.2	Numerical Implementation	34
3.2.1	Development of IRPSS Code	34
3.2.2	Eigenmode Summation	38
3.2.3	Numerical Time Integration	39
3.2.4	Multi Slice Bunch Simulation Method	45
3.2.5	Benchmark Modeling and Comparison	49
3.3	Discussion	54
4	Application to the RF Photoinjector Experiments	55
4.1	Simulation Set-Up for the RF Photoinjector	56
4.1.1	Prescribed Trajectory	56
4.1.2	External Fields	58
4.1.3	Equations of Motion	61
4.2	Space-Charge Fields and Beam Dynamics	62
4.2.1	Calculations of Space-Charge Fields	62
4.2.2	Beam Dynamics with Space-Charge Effects	72
4.3	Experimental Measurements	78
4.4	Discussion	81
5	Transverse Current Modeling	82
5.1	Electromagnetic Field for Circularly Symmetric Sources	82
5.1.1	Expansions of Charge and Current Densities	83
5.1.2	TE Mode Space-Charge Fields	84

5.1.3	TM Mode Space-Charge Fields	86
5.2	Numerical Implementation	89
5.2.1	Description of the System	89
5.2.2	Derivations of the Space-Charge Fields	89
5.2.3	Numerical Requirements	96
5.2.4	Space-Charge Fields with Transverse Current	100
6	Conclusions and Future Plans	104
6.1	Space-Charge Modeling of the RF Photoinjector	105
6.2	Application to the RF Photoinjector	106
6.3	Transverse Current Modeling	106
6.4	Future Plans	107
	Appendix	109
A	Electromagnetic Space-Charge Fields	109
A.1	Scalar and Vector Potentials	110
A.2	Transverse Electric and Magnetic Fields	111
A.3	Longitudinal Electric Field	112
A.3.1	Derivation of E_z	112
A.3.2	Analytic form of E_z	116
B	Electrostatic Space-Charge Fields	117
B.1	Electrostatic Space-Charge Fields with Delta-Function Source	117
B.2	Electrostatic Fields with a Constant J_z	119
B.3	Electrostatic Spacecharge Fields with the finite size bunch length	121
	Bibliography	123

List of Tables

3.1	The rf photoinjector beam parameters of the BNL 2.856 GHz and the ANL AWA 1.3 GHz guns	35
-----	---	----

List of Figures

1.1	Schematic diagram of the rf photoinjector. By exciting the photocathode using the laser (green), the electron beam (red) is emitted. The beam is accelerated by the rf field (black), which is operating in a TM_{010} π -mode. The solenoid magnetic fields are provided to reduce the emittance growth [12]	4
2.1	The SCHEFF method models the electron bunch (a) as a collection of macro-particles, and (b) breaks into concentric annular rings. Each ring is assumed to contain a uniform charge distribution. (d) The ring can be described on a 2-d grid where each cell is the intersection of a ring with a radial plane (constant θ) [31]	11
2.2	Discretization of the system into cubes and the position of field components on the grid.	16
3.1	Schematic of an electron source showing a planar cathode at $z = 0$, a surrounding pipe which has an arbitrary cross section but is axially uniform for $z > 0$, and ac accelerating electron beam	20
3.2	Plots of E_r vs. r and z , for $t = 0.25a/c$	30
3.3	Plots of E_z vs. r and z , for $t = 0.25a/c$	30

3.4	The plots of the beam distribution function with different beam sizes. The original function is plotted without the expansion, and rmn is the radial eigenmode number.	37
3.5	E_r vs. r for different eigenmode number, rmn	40
3.6	Plots of the arguments of the time integration for 1 (red), 10 (green), 100 (blue), 500 (pink), 1000 (light blue), and 2000 (yellow) eigenmode numbers.	42
3.7	E_r vs. r for different numerical integration time steps: $d\tau' = cdt'/a = 10^{-4}$, 10^{-5} , and 10^{-6}	43
3.8	E_z vs. z for different numerical integration time steps: $d\tau' = cdt'/a = 10^{-4}$, 10^{-5} , and 10^{-6}	44
3.9	E_r vs. z at $r = r_b$ for different numbers of slices	46
3.10	E_z vs. z at $r = 0$ for different numbers of slices	47
3.11	E_z vs. z at $r = r_b$ for the different number of slices	48
3.12	(a) IRPSS simulation of a disk bunch of charge emitted at time $t = 0$ from the cathode surface moving uniformly with speed v (b) Analytical model of two disks of charge moving uniformly in opposite directions for all time and intersecting at $t = 0$	51
3.13	Plots of E_r vs. r at the bunch location $z/a = 0.225$, showing the numerical scheme (solid line) and the benchmark example (dashed line).	52
3.14	Plots of E_z vs. z , showing the numerical scheme (solid line) and the benchmark example (dashed line).	53
4.1	The trajectory, velocity, and acceleration of a particle in ANL AWA 1.3 GHz rf photoinjector are plotted as functions of $\tau = ct/a$ with the rf peak field of 77 MV/m.	57

4.2	The external rf (dark blue) and solenoid (green) fields are plotted in the schematic diagram (light blue) of the ANL AWA 1.3 GHz rf photoinjector. For comparison, the rf fields (orange) calculated from SUPERFISH and those of TM_{010} mode are presented.	59
4.3	The longitudinal space-charge fields at $r = 0.0$ and $z = 0.0$ computed by IRPSS (red) and electrostatic methods(blue)	67
4.4	Percentage difference between critical electromagnetic and electrostatic E_z space-charge fields for different beam radii	68
4.5	Electromagnetic (IRPSS) and electrostatic space-charge fields for different times: F_r/Q vs. r at the center of the beam	69
4.6	The longitudinal electromagnetic (IRPSS) and electrostatic space-charge fields for different times: F_z/Q vs. z at $r = 0.0$	71
4.7	Phasespace plots with zero space-charge field	73
4.8	Phasespace plots for $Q = 100\text{ pC}$	74
4.9	Phasespace plots for $Q = 500\text{ pC}$	75
4.10	Normalized rms transverse emittances	77
4.11	Experimental set up for beam loss measurements	79
4.12	Experimental results of bunch charge vs. laser pulse intensity for different bunch lengths.	80
5.1	Plots of r_b and $\frac{dr_b}{dt}$ as functions of time.	90
5.2	Plots of the normalized radial electric field at $z = 0$ and $t = 0.25T$ are plotted using 5 radial modes (red:solid), 10 modes (green:dashed), 50 modes (blue:dotted), and 100 modes (pink:dashed-dotted) (rmn is the radial eigenmode number).	97
5.3	Plots of the percentage error of the normalized radial electric field at $z = 0$ and time $t = 0$	98

5.4	Plots of the normalized radial electric field at $z = 0$ and at time (a) $t = 0$, (b) $t = 0.25T$, (c) $t = 0.5T$, (d) $t = 0.75T$, and (e) $t = T$ computed electrostatically (red:solid) and electromagnetically (blue:dashed). . .	101
5.5	Plots of the normalized longitudinal electric field at (a) $r = 0$ and (b) $r = 0.25a$ for times $t = 0$, $t = 0.25T$, $t = 0.5T$, $t = 0.75T$, and $t = T$ computed electrostatically (red:solid) and electromagnetically (blue:dashed).	103

Chapter 1

Introduction

In most of electron accelerator systems, such as FELs (Free Electron Laser) [1, 2] and Colliders [3, 4], the high “quality” electron beam has been critically required. For example, the FEL needs an electron beam with a short wavelength and dense phasespace density to generate coherent radiation sources. In the high energy physics area, the e^+e^- colliders demand a high number of possible events at IPs (Interaction Points). In these applications, it is very important to achieve a bunched beam to a small spot size, i.e., high quality beam.

The beam quality can be described in various ways, however, the beam “brightness” is a figure of merit to measure the beam quality for the electron beam. Qualitatively, the brightness is a measure of the ability of a beam to be focused in 6-dimensional phasespace. The brightness of the beam, \mathcal{B} , is defined as the density of particles in the 6-D phasespace [5]:

$$\mathcal{B} = \frac{\text{spectral flux of the beam}}{\text{transverse phasespace area}} = \frac{2I_{peak}}{\epsilon_{n,x}\epsilon_{n,y}}, \quad (1.1)$$

where I_{peak} is the peak current of the beam, and $\epsilon_{n,x}$ and $\epsilon_{n,y}$ is the normalized transverse emittances. Eqn. (1.1) tells us that the larger peak current and the lower emittances of the beam, the higher the beam brightness could be achieved.

The emittance in Eqn. (1.1) is the area occupied by the beam distribution in each transverse phasespace plane. These show how the beam is focused in that plane. The term, normalized, includes the information of the beam's energy. The normalized beam emittance, for example in the horizontal direction, is given by

$$\epsilon_{n,x} = \beta\gamma\epsilon_x \quad (1.2)$$

where $\beta = v/c$, γ is the relativistic Lorentz factor. Eqn. (1.3) shows the normalized rms emittance. which is used more often since it can provide the information of the beam regardless of the particle's distribution [6].

$$\epsilon_{n,x}^{\text{rms}} = \sqrt{\langle x^2 \rangle \langle x'^2 \rangle - \langle xx' \rangle^2}. \quad (1.3)$$

The FEL is a coherent radiation source driven by an electron beam. In the FEL, the electron beam traverses a series of alternating magnets, such as a wiggler or undulator, and radiates light at wavelengths depending on the electron's energy, wiggler period, and magnetic field. In order to get coherent radiation, the electron bunch must be focused to a small spot size less than or equal to the radiation wavelength. This requires that the transverse emittances of the beam must be small. For example, SASE-FEL (Self Amplified Spontaneous Emission FEL) demands the normalized emittance on the order of 2 *mm-mrad*, and the requirement for the brightness is $9 \times 10^{13} \text{ A/m}^2\text{rad}^2$ [7]. The 4th generation of X-ray light sources needs much smaller emittances ($< 0.1 \text{ mm-mrad}$) and much higher brightness ($> 10^{17} \text{ A/m}^2\text{rad}^2$) [8].

In high energy and nuclear physics, accelerators have been very important tools for verifying their theories and models. For example, the Standard Model has been successfully proved by various experiments using particle colliders. There are comprehensive efforts to find the Higgs particle to complete this model. Current studies believe that it requires higher than 100 *GeV* of center of mass energy. Recently, there is international collaborative efforts to design and construct the ILC (International

Linear Collider) at a center of mass energy of $0.5 \sim 1 \text{ TeV}$ [9]. This machine requires that $\epsilon_{n,x} \simeq 10 \text{ mm-mrad}$, $\epsilon_{n,y} \simeq 0.02 \text{ mm-mrad}$, and $\mathcal{B} \simeq 10^{13} \text{ A/m}^2\text{rad}^2$. These parameters are very challenging, and the design efforts are still progressing.

1.1 RF Photoinjector

Various electron sources are used to satisfy the requirements for parameters of applications. Usually, the rf photoinjectors are widely used to produce high-brightness beams, since it can generate a bunched beam without the buncher or other bunching devices and the electron beams are rapidly accelerating using the high accelerating gradient due to the rf field. It also has an advantage of generating an initially small emittance beam which is determined by the wavelength of the laser.

The rf photoinjector consists of three main parts, the photocathode, the laser system, and rf cavities. The electron beams are generated by hitting the laser light to the photocathode, and they are accelerated by the rf electric fields. By using the high gradient rf field, the beam is accelerated more rapidly than with a DC field. The first rf gun was tested at Los Alamos [10], and it is now widely used in numerous laboratories as electron sources.

The rf photoinjector is often times operated in a TM_{010} mode of a pillbox cavity, and the fields in each cavity are out of phase by 180 degrees, i.e., π -mode. Figure 1.1 shows the schematic diagram of the rf photoinjector. The electron beam in the rf photoinjector is accelerated under the influence of both rf and space-charge fields. In general, space-charge fields can cause significant emittance growth. In many papers, people have tried to analyze the space-charge effects in the rf photoinjector.

K.-J. Kim first studied the analytical calculations of effects due to rf and space-charge fields in beam dynamics [11]. He presented that (1) the acceleration process due to the rf field, (2) the effects of the rf acceleration on transverse dynamics, and

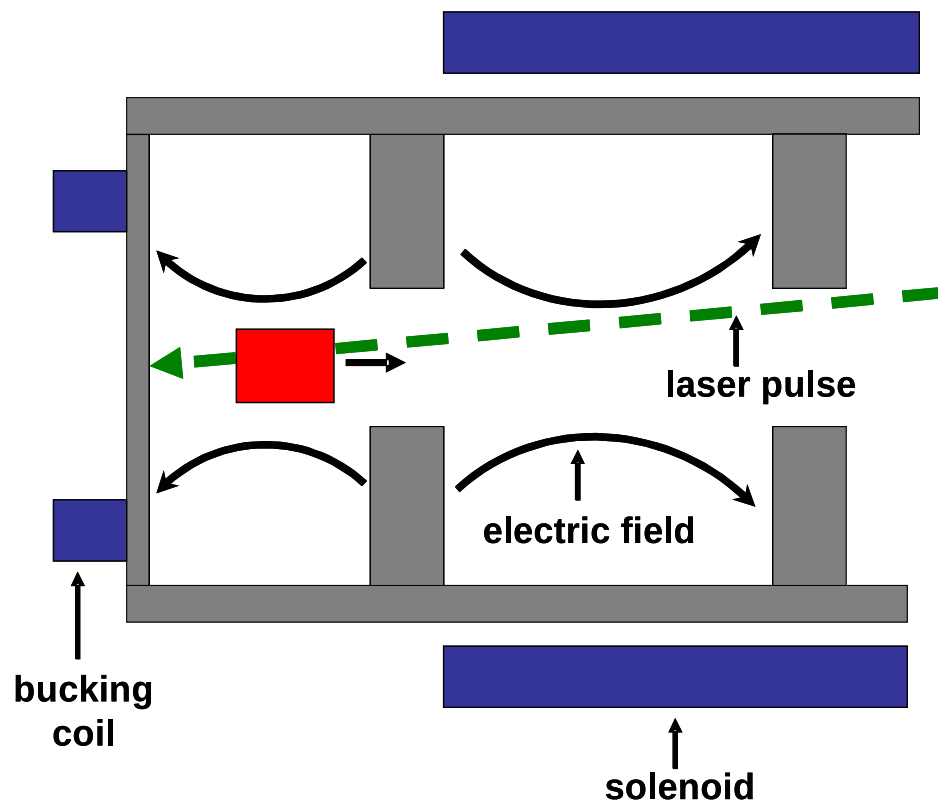


Figure 1.1: Schematic diagram of the rf photoinjector. By exciting the photocathode using the laser (green), the electron beam (red) is emitted. The beam is accelerated by the rf field (black), which is operating in a TM_{010} π -mode. The solenoid magnetic fields are provided to reduce the emittance growth [12]

(3) the transverse and longitudinal emittances resulting from the space-charge effects. His analyses were done by deriving the energy scaling of the field components under assumptions of a quasi-electrostatic approximation in the rest frame of the beam and a $1/\gamma^2$ dependence of the space-charge force.

There is another analytical approach to investigate the space-charge effects called K-V envelope theory, which is named after its discoverers, Kaphchinskij and Vladimirskij [13]. Sacherer calculated the space-charge effects in the accelerator system using K-V envelope theory [14]. This theory can predict the size of the beam with both space-charge and external forces. The envelope analysis for the rf photoinjector can be found in the paper of Serafini *et al* [15]. Although it can provide an excellent description of the beam, however, it does not address the emittance growth resulting from the z-dependence of the rf and space-charge fields, as well as wakefields, due to the discontinuities of the cavity geometry.

1.2 Main Contributions of the Thesis

The fully analytical treatments of the electromagnetic space-charge fields in the rf photoinjector have not been developed. Since the beam is emitted with low energy and is accelerated to a relativistic energy in a few *cm*, its beam dynamics are strongly affected by the space-charge fields. In this thesis, our goal is to investigate the space-charge effects in beam systems. Specifically, we will focus on rf photoinjectors and high-power microwave sources. The analytical and numerical solutions of electromagnetic space-charge fields will be presented in the presence of a conducting wall and flat cathode.

Many computational codes, such as PARMELA [16], ASTRA [18], TREDI [17], and MAFIA [19], are capable of simulating the photoinjector. However, most of them utilize Particle-In-Cell (PIC) methods to calculate the fields generated by the beam.

In order to understand the motion of the beam in the photoinjector, we need to be able to analyze the electromagnetic fields, since the space-charge fields strongly depend on time. However, the PIC algorithms have limitations for analyzing the space-charge fields. And there are unphysical effects, which arise in PIC codes, for example, the numerical grid dispersion and numerical Cherenkov radiation [20, 21].

Numerous papers have studied space-charge effects in the rf photoinjector. For example, E. Colby *et al* showed that the electrostatic space-charge induced beam dynamics for a 10 *psec* bunch with a beam radius of 1 *mm* disagrees with electromagnetic calculations by 20% at locations which are a few centimeters from the cathode [22]. These results were further verified by A. Candel *et al* which showed these differences and found that the discrepancy can be larger at distances beyond 5 cm for the LCLS gun [23]. Other results, such as by J.-M. Dolique *et al*, suggest the importance of the self-generated magnetic space-charge field in beam dynamics within the rf gun, even for long bunch lengths, i.e., 100 *psec* [24]. Near the cathode, one expects to find significant differences between electrostatic and electromagnetic space-charge solvers. And a full investigation of these differences near the cathode is important for a complete physics understanding of the rf gun.

There are several studies which analyzed the electromagnetic fields based on Green's function methods [25, 26, 21]. These references [25, 26] utilize the Fourier *k*-space in the longitudinal direction and Bessel function expansion in the transverse directions. They assumed that the beam has a uniform density and is accelerated uniformly. But the uniform density beam is not entirely correct during the acceleration process, and the beam is not accelerated uniformly since the rf field is varying in time.

In an effort to improve the modeling capability in the rf photoinjector, we have developed the computational code, IRPSS (Indiana University RF Photoinjector Source Simulator), for computing the electromagnetic space-charge fields based on Green's

function methods. This code calculates the electromagnetic space-charge potentials and fields numerically.

In application for high-power microwave sources, an extended Green's function technique will be discussed in Chapter 5. This method will include the effect of transverse currents of bunched charged particle beams. We have used our Green's function method to numerically simulate the space-charge field of a bunched electron beam undergoing "radial breathing mode oscillations" which can occur in a high-power klystron drift tube.

1.3 Outline of the Thesis

Chapter 2 will present the various numerical algorithms, which are capable of modeling the space-charge fields of the electron beam in the conducting cavity, especially, the rf photoinjector. First, we will show the existing and mostly used algorithms, such as SCHEFF, Lienard-Wiechert potentials, and Yee/PIC, for comparisons with our work. As mentioned previously, another Green's function approach from Salah *et al* will be discussed.

Chapter 3 will show how to calculate the electromagnetic space-charge fields in an arbitrary cross-section conducting pipe with longitudinal beam currents in the presence of the cathode at $z = 0$, using Green's function methods. For specific cases, we will present examples of the circular pipe cross-section with longitudinal currents and the rectangular pipe cross-section with arbitrary currents.

For the case of the circular pipe with longitudinal currents, which is an example of the rf photoinjector, the simulation code, IRPSS, has been developed. In Chapter 3, we will describe the computational requirements for the space-charge field calculations using IRPSS. The benchmark study will be presented to check the validity of our Green's function technique and numerical implementations

In Chapter 4, we apply Green's function techniques to compute the space-charge fields in the rf photoinjector. The parameters of the ANL AWA 1.3 GHz rf photoinjector [27] are used for the simulation in this chapter. We will discuss how the electromagnetic space-charge fields near the cathode are different from the electrostatic space-charge fields in time. With these space-charge fields, beam dynamics simulations are conducted. Specifically, we will track the radial phasespaces for both cases. We also describe the results of an experimental beam loss measurement which attempts to distinguish the fully electromagnetic space-charge offsets in the longitudinal direction from the electrostatic space-charge models.

Chapter 5 presents the space-charge field solutions in the presence of transverse currents in circular conducting pipe, which were ignored in the previous chapter. The electromagnetic fields are derived using the Bessel function series expansions of charge and current densities and components of the space-charge fields. These solutions can be also utilized for the rf photoinjector. As an example, we will see how the space-charge fields are varying for a radially oscillating beam in a circular conducting pipe.

Finally, in Chapter 6, we will conclude this dissertation work. And we will discuss the future plan for improving our work.

Chapter 2

Theoretical Space-Charge Modeling

There have been numerous codes and methods developed to accurately compute the space-charge effects in the accelerator system. Especially, in order to design the rf photoinjector, PARMELA (Phase And Radial Motion in Electron Linear Accelerators) [16] is a workhorse code and is widely used for various examples. It can simulate the beam dynamics within the external fields, such as the rf and solenoid fields. However, it can only calculate space-charge fields electrostatically. TREDI (Three-Dimensional Injectors) [17] is fully 3-dimensional simulation code for charge particles in the electron source. The space-charge fields are computed using Lienard-Wiechert potentials. PIC (particle-in-cell) is the one of the most commonly used methods to simulate the beam dynamics, and fully electromagnetic PIC codes, such as MAFIA [19], compute the space-charge fields in the arbitrary conducting boundaries by using grid based field solving methods, for example, Yee algorithm [28]. There are also analytical approaches to compute space-charge fields directly from Maxwell's equations using either Lorenz or Coulomb gauge condition [25, 26]. In this chapter,

we present commonly used existing space-charge algorithms, especially, for designing the rf photoinjector system. And we briefly explain our space-charge algorithm.

2.1 Existing Space-Charge Algorithms

2.1.1 SCHEFF Algorithm (PARMELA and ASTRA)

PARMELA and ASTRA, which are widely used codes for modeling the rf photoinjector, use an electrostatic based space-charge field ring algorithm called SCHEFF (Space CHarge EFfect) [29]. In PARMELA, the SCHEFF algorithm has two versions, SCHEFF (2D), and SPCH3d. In this present work, since we concentrate on the cylindrically symmetric system, we will not discuss the SPCH3d code, which is a 3-D PIC routine, and calculates the field solutions based on a convolution of the charge density and the Green's function of the potential [30]. There are also advanced modifications for the elliptically symmetric system [31]. The 2-dimensional SCHEFF algorithm assumes that the system is azimuthally symmetric. The SCHEFF algorithm breaks up the macro-particles, which are in the beam volume, into a set of annular rings, and integrates trajectories of these rings through the fields using the phase (time) as an independent variable. Figure 2.1 shows how these rings are represented in the grid cells.

In order to include relativistic effects of accelerating beams in the SCHEFF algorithm, the electrostatic space-charge fields are calculated with rings in the average rest system of the bunch, and transformed back into the laboratory frame, again. The electric components are calculated at each observation point by performing a two-dimensional integration in (r, z) space, where each element of integration is a circular ring of charge that intersects the cell. The electric field components at the

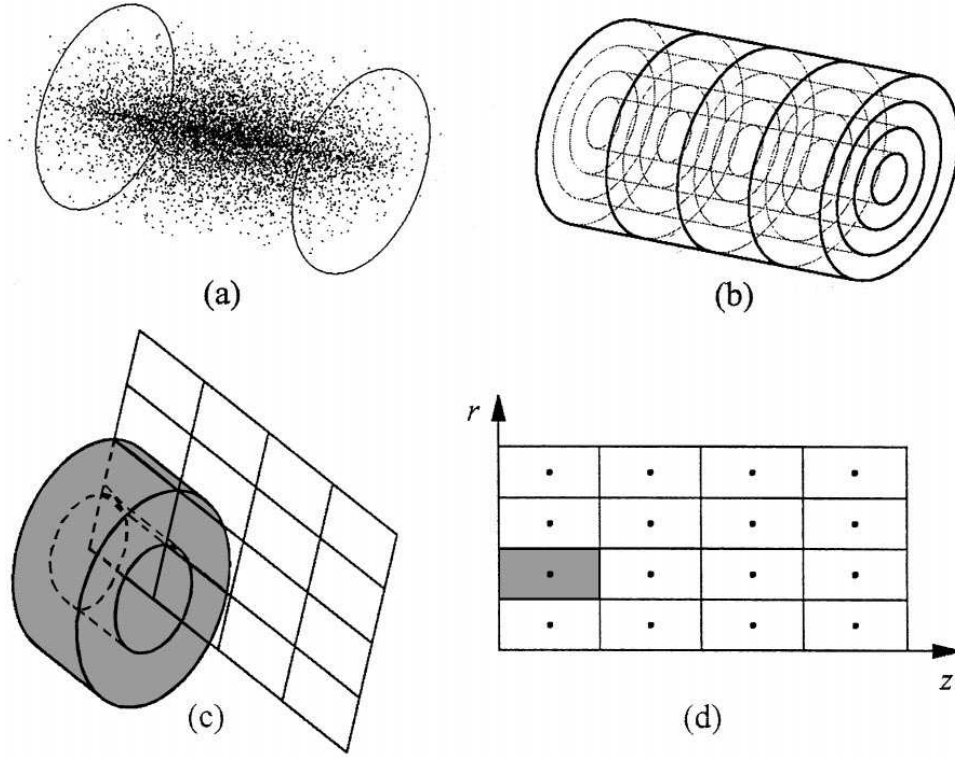


Figure 2.1: The SCHEFF method models the electron bunch (a) as a collection of macro-particles, and (b) breaks into concentric annular rings. Each ring is assumed to contain a uniform charge distribution. (d) The ring can be described on a 2-d grid where each cell is the intersection of a ring with a radial plane (constant θ) [31]

rest frame can be expressed as [32],

$$E_r(r, z) = \frac{1}{4\pi\epsilon_0} \frac{Q}{2\pi r_b} \frac{2r_b}{r [z^2 + (r + r_b)^2]^{1/2}} \left[K(k) - \frac{z^2 - (r^2 - r_b^2)}{z^2 + (r + r_b)^2} E(k) \right] \quad (2.1a)$$

and

$$E_z(r, z) = \frac{1}{4\pi\epsilon_0} \frac{Q}{2\pi r_b} \frac{4r_b z E(k)}{[z^2 + (r + r_b)^2]^{1/2} [z^2 + (r - r_b)^2]}, \quad (2.1b)$$

where r_b is the beam radius, Q is the bunch charge, $k = [4r_b r / (z^2 + (r + r_b)^2)]^{1/2}$ and K and E are the complete elliptical integrals of the first and second kind, respectively. The size of the ring is scaled with the variation of the beam size to match the amount of the charge in the each ring.

However, one can observe limitations in PARMELA as the SCHEFF subroutine is used. First, since it assumes that the current density is zero in the beam rest frame, it can only calculate the space-charge fields electrostatically, i.e., not including time retardation effects. In PARMELA, particles are pushed by the external rf and solenoids fields, which are computed from SUPERFISH and POISSON [33], respectively, in the region where the beam travels. It takes into account the beam space-charge fields induced by the real charge, as well as the image charge in the cathode. A second limitation is that even though it can also include interactions between the beam and the cavity walls, i.e., the wakefields, these fields cannot be computed internally, but must be imported externally. A third limitation is that the radial force generated from the azimuthal self-induced magnetic field B_θ is neglected. Moreover, the accuracy in PARMELA are in question for low energies near the cathode for the high brightness regime [31].

2.1.2 Lienard-Wiechert Potentials (TREDI)

TREDI is a multi-purpose macro-particle 3D Monte Carlo code, which can handle the electron beam in the various accelerator systems, such as rf photoinjectors, linacs, and bending magnets [17]. The beam dynamics in TREDI is obtained by integrating the Lorentz force law by means of a 4th order Runge-Kutta algorithm. The external fields from rf cavities, solenoids, or bending magnets can be computed analytically, loaded from external files, or evaluated from the on-axis fields using the series expansion.

The space-charge fields induced by the beam is calculated using Lienard-Wiechert potentials [34], and are given by

$$\mathbf{E} = \frac{1}{4\pi\epsilon_0} \frac{\hat{n} \times [(\hat{n} - \vec{\beta}) \times \dot{\vec{\beta}}]}{(1 - \vec{\beta} \cdot \hat{n})^3 |\mathbf{R}|} + \frac{1}{4\pi\epsilon_0} \frac{(\hat{n} - \vec{\beta}) [1 - |\vec{\beta}|^2]}{(1 - \vec{\beta} \cdot \hat{n})^3 |\mathbf{R}|^2} \quad (2.2a)$$

and

$$\mathbf{B} = \frac{1}{c} \hat{n} \times \mathbf{E}, \quad (2.2b)$$

where $\mathbf{R} = |\mathbf{x} - \mathbf{x}'|$, $\hat{n} = \mathbf{R}/|\mathbf{R}|$, and these fields are calculated at the retarded time,

$$t' = t - \frac{|\mathbf{R}(t')|}{c}. \quad (2.3)$$

Similar to PARMELA and ASTRA, TREDI assumes that the velocity of the source particle does not change on a time scale comparable to the retarded time, and the contribution of acceleration fields is negligible. Moreover, the fields are calculated in the rest frame, and then are transformed to the laboratory frame using the Lorentz transformation:

$$\mathbf{E}_{\text{lab}} = \gamma \mathbf{E}_{\text{rest}}, \quad (2.4a)$$

and

$$\mathbf{B}_{\text{lab}} = \vec{\beta} \times \mathbf{E}_{\text{lab}}. \quad (2.4b)$$

However, these fields are computed in the presence of a flat cathode and in free-space, i.e., there is no other conductor boundaries, such as cavity walls.

2.1.3 Yee/PIC Method (MAFIA)

MAFIA utilizes the Yee/PIC method to model the electromagnetic space-charge fields in the accelerator system [19]. The Yee algorithm is a FDTD (Finite-Difference Time-Domain) method to solve Maxwell's curl equations, and it has been widely used to calculate the electromagnetic fields for numerous problems, such as antennas, microwave circuits, and accelerator systems [28, 35].

In order to solve the time-dependent Maxwell's curl equations,

$$\nabla \times \mathbf{E} = -\frac{\partial \mathbf{B}}{\partial t}, \quad (2.5a)$$

and

$$\nabla \times \mathbf{H} = \mathbf{J} + \frac{\partial \mathbf{D}}{\partial t}, \quad (2.5b)$$

for an isotropic medium, first, Eqn.(2.5) are written in the differential forms in Cartesian coordinates as:

$$\frac{\partial B_x}{\partial t} = \frac{\partial E_y}{\partial z} - \frac{\partial E_z}{\partial y}, \quad (2.6a)$$

$$\frac{\partial B_y}{\partial t} = \frac{\partial E_z}{\partial x} - \frac{\partial E_x}{\partial z}, \quad (2.6b)$$

$$\frac{\partial B_z}{\partial t} = \frac{\partial E_x}{\partial y} - \frac{\partial E_y}{\partial x}, \quad (2.6c)$$

$$\frac{\partial D_x}{\partial t} = -J_x + \frac{\partial H_z}{\partial y} - \frac{\partial H_y}{\partial z}, \quad (2.6d)$$

$$\frac{\partial D_y}{\partial t} = -J_y + \frac{\partial H_x}{\partial z} - \frac{\partial H_z}{\partial x}, \quad (2.6e)$$

and

$$\frac{\partial D_z}{\partial t} = -J_z + \frac{\partial H_y}{\partial x} - \frac{\partial H_x}{\partial y}. \quad (2.6f)$$

In the Yee algorithm, the spatial coordinates (i, j, k) are defined as $(i\Delta x, j\Delta y, k\Delta z)$, where Δx , Δy , and Δz are grid separations in Cartesian coordinates. And then, each component of the electromagnetic fields in Eqn. (2.6) can be written as

$$F^n(i, j, k) = F(i\Delta x, j\Delta y, k\Delta z, n\Delta t), \quad (2.7)$$

where F can be any of E_x , E_y , E_z , B_x , B_y , and B_z , Δt is the time step, and n is the time index. The differential equations, Eqn. (2.6), will be computed using central differential approximations, for example,

$$\frac{\partial F^n(i, j, k)}{\partial x} = \frac{F^n(i + 1/2, j, k) - F^n(i - 1/2, j, k)}{\Delta x}, \quad (2.8a)$$

and

$$\frac{\partial F^n(i, j, k)}{\partial t} = \frac{F^{n+1/2}(i, j, k) - F^{n-1/2}(i, j, k)}{\Delta t}. \quad (2.8b)$$

Since we are using the central difference approximations, Eqn. (2.8) has a second-order accuracy in space and time.

The field components of \mathbf{E} and \mathbf{B} , in Eqn. (2.6) are spatially offset from one another, as seen in Figure 2.2. In Figure 2.2, The secondary lattice edges (red) connect centers of primary lattices (blue). The electric field components are constant along the edges of the primary lattice and are parallel to the primary lattice, while the magnetic field components are constant through the faces of the primary lattice. The magnetic field components are constant along the edges of the secondary lattice and are parallel to the secondary lattice, while the electric field components are constant through the faces of the secondary lattice.

In addition, \mathbf{E} and \mathbf{B} are also offset in time by $\Delta t/2$ using the leap-frog algorithm [36]. These offsets leads that the change of \mathbf{E} in time depends on the change of \mathbf{B} in space, and vice versa. Therefore, the new \mathbf{E} in time can be calculated from the old \mathbf{E} in time and the spatial derivatives of \mathbf{B} in the surrounding lattice. In a similar fashion, the new \mathbf{B} can be obtained.

In addition to the order of approximation of the discretization of the differential equations, there are several other factors that impact the accuracy of the finite element modeling. Since dimensions of the source are small, grid sizes of the cell must be sufficiently small enough to resolve the wave propagation through the cell. This requires large number of cells and consequently demands intensive computational

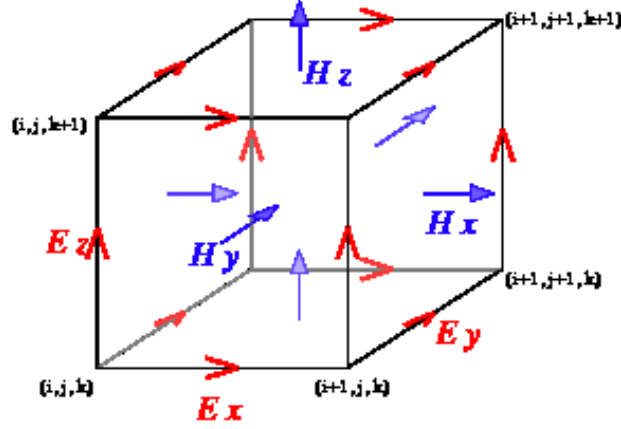


Figure 2.2: Discretization of the system into cubes and the position of field components on the grid.

resources. The FDTD method also suffers from numerical dispersion. The numerical phase velocity of the electromagnetic wave induced by the beam can be slower than the physical one. This implies that the particles can be traveling faster than the electromagnetic radiation induced by themselves. Consequently, this violates the causality condition and gives rise to numerical Cherenkov radiation [20].

2.2 Green's Function Approaches

2.2.1 Mode Analysis and Series Expansions

There have been analytical approaches to solve the electromagnetic fields in a rf photoinjector [25, 26], which are based on the Green's function method. These approaches solve the Maxwell's equation in the presence of the boundary conditions, such as a cathode and the cavity walls, using two different gauge conditions. And the cylindrical symmetry is used to simplify the problem. However, the reflection waves

from the wall are excluded since the system assumes the cavity radius is much greater than the beam radius.

First, the scalar and vector potentials are assumed to satisfy the “Lorenz gauge” condition [25],

$$\nabla \cdot \mathbf{A} + \frac{1}{c^2} \frac{\partial \phi}{\partial t} = 0. \quad (2.9)$$

Then, this implies the wave equations for potentials as:

$$\left(\nabla^2 - \frac{\partial^2}{\partial t^2} \right) \mathbf{A} = -\mu_0 \mathbf{J}, \quad (2.10a)$$

and

$$\left(\nabla^2 - \frac{\partial^2}{\partial t^2} \right) \phi = -\frac{1}{\epsilon_0} \rho \quad (2.10b)$$

The particular solutions of Eqn. (2.10a) can be found by using the series expansion of \mathbf{A} , then the coefficients of the expansion are calculated from the Fourier transformation in normal modes and the Green's function method. And the general solution is easily obtained from the homogeneous equation in Eqn. 2.10a. One can get the scalar potential, ϕ , using the Lorenz gauge condition, in Eqn. (2.9).

Another approach utilizes the “Coulomb gauge” condition [26], $\nabla \cdot \mathbf{A} = 0$. This yields the wave equations,

$$\nabla^2 \phi = -\frac{1}{\epsilon_0} \rho, \quad (2.11a)$$

and

$$\left(\nabla^2 - \frac{\partial^2}{\partial t^2} \right) \mathbf{A} = -\mu_0 \mathbf{J} + \frac{1}{c^2} \frac{\partial}{\partial t} (\nabla \phi) \quad (2.11b)$$

Eqn. (2.11) is solved by using the integral transform and Green's function method.

These two techniques have advantages that it can be used to calculate the space-charge fields to arbitrary accuracy for given beam charge and current densities when there is a sufficient amount of eigenmode numbers and Fourier modes.

2.2.2 Analytical Method with Green's Function

Similar to the methods developed by Salah *et al* [25, 26], we have developed analytical solutions to Maxwell's equations for the rf photoinjector in the presence of boundary conditions, such as the flat cathode and conducting cavity walls. The arbitrary longitudinal current densities of the beam are assumed to be in axially boundary conditions with an arbitrary cross-section. We find the electromagnetic space-charge potentials and fields using the time-dependent Green's function methods in Chapter 3.

The Green's function methods explicitly include the causality condition, which is important in the beam dynamics of the bunch head when the beam is emitted from the cathode. And the time-retardation effect, which can be a delayed interaction between the head and tail of the bunched beam, is also included. Since Green's functions are solutions to the wave equations with the delta function source, it is possible to accurately compute the electromagnetic fields of the bunch with arbitrary bunch length in the longitudinal direction. In addition, since the space-charge fields using the Green's function methods can be found everywhere in space and time, as opposed to a grid based space-charge algorithm, this method has an advantage of being dispersion free.

In Chapter 5, we will show the more general solution for the electromagnetic fields in the pipe structure with a cylindrically symmetric beam when transverse currents are present. Numerical implementations of our Green's function approaches for specific examples will be shown. Finally, in order to check the importance of the electromagnetic effects in both cases, we also derive the electrostatic Green's function solutions. These will be discussed briefly in the following chapters.

Chapter 3

Space-Charge Modeling of the RF Photoinjector

3.1 Electromagnetic Space-Charge Potentials and Fields

In order to model space-charge physics in the rf photoinjector, we simplify the geometry of the system with a flat cathode which is located at $z = 0$ and a surrounding conducting pipe of an arbitrary uniform cross section which is extended to infinity. An electron source beam which is generated by a laser pulse consists of a charge density $\rho(\mathbf{r}, t)$ and a current density $\mathbf{J}(\mathbf{r}, t)$. Figure 3.1 shows the schematic view of this system with the electron beam.

In this section, we will show the solutions of the electromagnetic space-charge potentials and fields of the rf photoinjector system with an electron beam for two specific cases. First, the solutions for the system with an arbitrary pipe cross section, but with only longitudinal beam currents, i.e., $\mathbf{J}(\mathbf{r}, t) = J_z(\mathbf{r}, t)\hat{e}_z$, will be shown. As an application to the rf photoinjector, we will show the potentials and fields of the

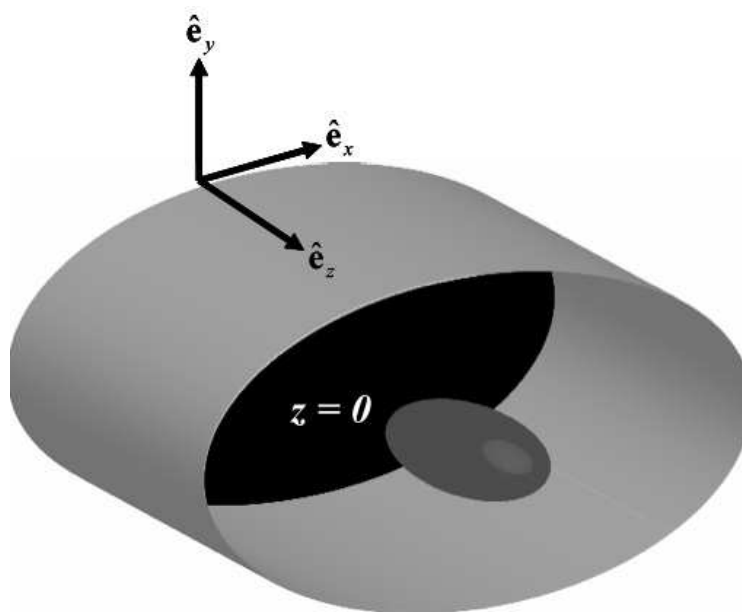


Figure 3.1: Schematic of an electron source showing a planar cathode at $z = 0$, a surrounding pipe which has an arbitrary cross section but is axially uniform for $z > 0$, and an accelerating electron beam

pipe with a circularly symmetric cross section. Second, we will present the solutions for the pipe with a rectangular cross section by assuming arbitrary beam currents. Although the system with a rectangular pipe cross section is only occasionally used in electron sources, it has a theoretical interest since it is a fully solvable system with arbitrary beam currents. The electromagnetic space-charge fields have not been solved for the system with an arbitrary, uniform pipe cross section with arbitrary beam currents. The calculations shown in this chapter have been outlined in our paper [21]

In general, the beam in an accelerating structure has transverse current components, as well as a longitudinal current component. But we note that the assumption of the beam current being solely in the longitudinal direction is very good since transverse currents will be typically small compared to the longitudinal current in the rf photoinjector system. This approximation can be verified by comparing the ratio of the transverse beam velocity to the longitudinal beam velocity. When the beam is emitted from the cathode, the ratio of the beam velocity can be approximated by the order of $|v_{\perp}/v_z| \sim |E_{\perp}/E_z|$. Each electric component consists of both the external rf field and space-charge field induced by the beam itself.

For the ANL 1.3 *GHz* photoinjector [27], the longitudinal accelerating rf field is the order of $25 \sim 100$ *MV/m*. The transverse rf field at the beam edge is about 3 % of the longitudinal electric field. Using the beam parameters, such as the bunch charge $Q_b = 1$ *nC*, the beam radius $r_b = 1$ *mm*, and the bunch length $l_b = 3$ *psec*, the transverse space-charge electric field is less than 10 % of the rf field. As the beam is accelerating by the rf field, the longitudinal velocity, v_z , is reduced by a factor of $1/\gamma$ due to the relativistic effect, where γ is the relativistic Lorentz factor. Since the velocity ratio is less than 10% for typical photoinjector systems, it is sufficient to approximate the beam currents for electromagnetic field calculations as $\mathbf{J}(\mathbf{r}, t) = J_z(\mathbf{r}, t)\hat{e}_z$.

3.1.1 Arbitrary Pipe Cross-Section with Longitudinal Currents

We assume that the system has the cross section of an arbitrary pipe cross section with the longitudinal beam currents, i.e., the current density is given by $\mathbf{J}(\mathbf{r}, t) = J_z(\mathbf{r}, t)\hat{e}_z$. For a given charge density $\rho(\mathbf{r}, t)$ and longitudinal current density $J_z(\mathbf{r}, t)$, the electromagnetic potentials, $\phi(\mathbf{r}, t)$ and $\mathbf{A}(\mathbf{r}, t) = A_z(\mathbf{r}, t)\hat{e}_z$, yield the electromagnetic space-charge fields, $\mathbf{E}(\mathbf{r}, t) = -\nabla\phi - \partial\mathbf{A}/\partial t$ and $\mathbf{B}(\mathbf{r}, t) = \nabla \times \mathbf{A}$, and these can be solved, i.e.,

$$\left(\nabla^2 - \frac{1}{c^2} \frac{\partial^2}{\partial t^2}\right) \phi(\mathbf{r}, t) = -\frac{\rho(\mathbf{r}, t)}{\epsilon_0}, \quad (3.1)$$

and

$$\left(\nabla^2 - \frac{1}{c^2} \frac{\partial^2}{\partial t^2}\right) A_z(\mathbf{r}, t) = -\mu_0 J_z(\mathbf{r}, t). \quad (3.2)$$

with the Lorenz gauge condition,

$$\frac{1}{c^2} \frac{\partial \phi}{\partial t} + \nabla \cdot \mathbf{A} = 0. \quad (3.3)$$

The beam charge and current densities satisfy the continuity equation,

$$\frac{\partial \rho}{\partial t} + \nabla \cdot \mathbf{J} = 0. \quad (3.4)$$

In this system, the flat cathode and the pipe are perfect conducting boundaries, and therefore the fields must satisfy the boundary conditions:

$$\mathbf{E}(\mathbf{r}, t) \times \hat{\mathbf{n}}|_{\text{surface}} = \mathbf{B}(\mathbf{r}, t) \cdot \hat{\mathbf{n}}|_{\text{surface}} = 0, \quad (3.5)$$

where \hat{n} denotes the normal vector on the conductor surface. Eqn. (3.3) can be satisfied by specifying the boundary conditions for the potentials to be:

$$\phi|_{\text{surface}} = 0, \quad (3.6)$$

$$\mathbf{A} \times \hat{n}|_{\text{surface}} = A_z|_{\text{surface}}^{z>0} = 0, \quad (3.7)$$

and

$$(\hat{\mathbf{n}} \cdot \nabla) (\mathbf{A} \cdot \hat{\mathbf{n}})|_{\text{surface}} = \frac{\partial \mathbf{A}}{\partial z} \Big|_{\text{surface}}^{z=0} = 0. \quad (3.8)$$

We note that Eqns. (3.6), and (3.7) yield the correct boundary conditions for the fields, and Eqn. (3.8) is obtained from Eqns. (3.6), and (3.7) along with the gauge condition in Eqn. (3.3).

The electromagnetic potentials may be written in terms of two electromagnetic Greens functions $G_\phi(\mathbf{r}, t; \mathbf{r}', t')$ and $G_z(\mathbf{r}, t; \mathbf{r}', t')$ as

$$\phi(\mathbf{r}, t) = \frac{1}{\epsilon_0} \int_{-\infty}^t \int G_\phi(\mathbf{r}, t; \mathbf{r}', t') \rho(\mathbf{r}', t') d^3\mathbf{r}' dt', \quad (3.9a)$$

and

$$A_z(\mathbf{r}, t) = \mu_0 \int_{-\infty}^t \int G_z(\mathbf{r}, t; \mathbf{r}', t') J_z(\mathbf{r}', t') d^3\mathbf{r}' dt', \quad (3.9b)$$

where both Green's functions satisfy the inhomogeneous wave equation with a delta function source:

$$\left(\nabla^2 - \frac{1}{c^2} \frac{\partial^2}{\partial t^2} \right) G_{\phi, z} = -\delta(\mathbf{r} - \mathbf{r}') \delta(t - t'), \quad (3.10)$$

but satisfy different boundary conditions:

$$G_\phi|_{\text{surface}} = 0, \quad (3.11a)$$

$$G_z|_{\text{surface}}^{z>0} = 0, \quad (3.11b)$$

and

$$\frac{\partial G_z}{\partial z} \Big|_{\text{surface}}^{z=0} = 0. \quad (3.11c)$$

from the boundary conditions of ϕ and A_z in Eqns. (3.6), (3.7), and (3.8). Here, the unprimed coordinates in space and time indicate the field point, while the primed coordinates are the source point.

Since the Green's functions which are defined by Eqn. (3.10) are generated by delta functions in both space and time, it is possible to calculate the electromagnetic

potentials, and hence, the electromagnetic fields for given beam charge and current densities as shown in Eqns. (3.9a) and (3.9b).

One can find the solutions to $G_{\phi,z}$ from the homogeneous solutions of Eqn. (3.10) [37], i.e.,

$$G_{\phi} = \frac{c\Theta(t-t')}{2} \sum_{mn} \psi_{mn}(\mathbf{r}_{\perp}) \psi_{mn}^*(\mathbf{r}'_{\perp}) \times [\Gamma_{-} - \Gamma_{+}] \quad (3.12a)$$

and

$$G_z = \frac{c\Theta(t-t')}{2} \sum_{mn} \psi_{mn}(\mathbf{r}_{\perp}) \psi_{mn}^*(\mathbf{r}'_{\perp}) \times [\Gamma_{-} + \Gamma_{+}], \quad (3.12b)$$

where $\mathbf{r}_{\perp} = \mathbf{r} - z\hat{e}_z$ and $\mathbf{r}'_{\perp} = \mathbf{r}' - z'\hat{e}_z$ are transverse vectors, the normalized eigenfunctions $\psi_{mn}(\mathbf{r}_{\perp})$ are the Dirichlet solutions of the transverse 2D Helmholtz equation with eigenvalues $k_{\perp mn}$, i.e.,

$$(\nabla^2 + k_{\perp mn}^2) \psi_{mn}(\mathbf{r}_{\perp}) = 0, \quad (3.13a)$$

$$\psi_{mn}(\mathbf{r}_{\perp})|_{\text{surf}} = 0, \quad (3.13b)$$

$$\int |\psi_{mn}(\mathbf{r}_{\perp})|^2 d^2\mathbf{r}_{\perp} = 1, \quad (3.13c)$$

and

$$\Gamma_{\pm} = \frac{1}{\pi} \int_{-\infty}^{\infty} dk \frac{e^{ik(z \pm z')} \sin \left[c\sqrt{k_{\perp mn}^2 + k^2} (t - t') \right]}{\sqrt{k_{\perp mn}^2 + k^2}}. \quad (3.14)$$

The Green's functions defined by the eigenfunction expansions in Eqns. (3.12a) and (3.12b), as well as the associated Γ_{-} and Γ_{+} defined by Eqn. (3.14), can be readily obtained in the following manner. First, by using the fact that

$$\Theta(t-t') \psi_{mn}(\mathbf{r}_{\perp}) e^{ikz} \{C_{mn} \cos[\omega(t-t')] + S_{mn} \sin[\omega(t-t')]\} \quad (3.15)$$

forms a complete set of eigenfunctions which are solutions to the homogeneous 3D Helmholtz equation, where C_{mn} and S_{mn} are constants and $\omega = c\sqrt{k_{\perp mn}^2 + k^2}$, we can express $G_{\phi,z}$ as a sum over these eigenfunctions. The factor $\Theta(t-t')$ is included to ensure causality. By inserting the expansion for $G_{\phi,z}$ into Eqn. (3.10) and then

integrating both sides by $\int_{t'-\epsilon}^{t'+\epsilon} dt$ in the limit $\epsilon \rightarrow 0$, it can be easily shown that $C_{mn} = 0$ and $G_{\phi,z}$ and Γ_{\perp} are given by Eqns. (3.12a), (3.12b) and (3.14). To be specific, the terms in $G_{\phi,z}$ corresponding to Γ_{+} yield an extra term proportional to $\delta(z + z')$ on the right-hand side of Eqn. (3.10). However, since $z, z' > 0$, this term is zero. The factor Γ_{+} in Eqns. (3.12a), and (3.12b) is necessary to satisfy the cathode boundary conditions at $z = 0$ given by Eqns. (3.11a) and (3.11b). From a physical point of view, Γ_{-} and Γ_{+} , represent the contributions of the real charge and image charge (due to the cathode at $z = 0$), respectively, on the electromagnetic fields. We note that the method of constructing Green's functions from eigenfunctions is a well-known method that is used extensively for solving non-homogeneous scalar wave equations [37].

The integral in Eqn. (3.14) may be simplified [38] to

$$\Gamma_{\perp} = J_0(k_{\perp mn} \lambda_{\pm}) \Theta(\lambda_{\pm}^2), \quad (3.16)$$

where $J_0(x)$ is the zeroth order Bessel function of the first kind, $\Theta(x)$ is the Heaviside-step function, and

$$\lambda_{\pm}^2 = c^2(t - t')^2 - (z \pm z')^2. \quad (3.17)$$

Using Eqn. (3.4) and integration by parts, one can readily check that the solutions given by Eqns (3.9), and (3.12) satisfy the Lorenz gauge condition. We note that the factors $\Theta(\lambda_{-}^2)$ and $\Theta(\lambda_{+}^2)$ enforce a causality condition on the electromagnetic waves emanating from the beam charge and induced image charges, respectively. When analyzing the potentials near the front of the bunch, these factors allow for rapid numerical convergence since only sources “sufficiently close” to the point of observation need to be considered.

The electromagnetic fields $\mathbf{E}(\mathbf{r}, t)$ and $\mathbf{B}(\mathbf{r}, t)$ can be computed from the potentials in Eqns. (3.9). In general, the electric field will have components in both the longitudinal and transverse directions, but under the assumption of only longitudinal

beam currents, the magnetic field will only have components in the transverse directions. The transverse electric and magnetic fields follow immediately from Eqns. (3.9), and are given by

$$\mathbf{E}_\perp = -\frac{c}{2\epsilon_0} \sum_{mn} \nabla_\perp \psi_{mn}(\mathbf{r}_\perp) \int_{-\infty}^t \int \psi'_{mn}(\mathbf{r}'_\perp) \times [\Gamma_- - \Gamma_+] \rho(\mathbf{r}'t') d^3\mathbf{r}' dt', \quad (3.18)$$

and

$$\mathbf{B}_\perp = -\frac{\mu_0}{2} \sum_{mn} \hat{e}_z \times \nabla_\perp \psi_{mn}(\mathbf{r}_\perp) \int_{-\infty}^t \int \psi'_{mn}(\mathbf{r}'_\perp) \times [\Gamma_- + \Gamma_+] J_z(\mathbf{r}'t') d^3\mathbf{r}' dt'. \quad (3.19)$$

The final solution to the electric field in the longitudinal direction requires a few mathematical steps. To start,

$$\begin{aligned} E_z &= -\frac{1}{\epsilon_0} \int_{-\infty}^t \int d^3\mathbf{r}' dt' \left[\frac{\partial G_\phi}{\partial z} \rho + \frac{1}{c^2} \frac{\partial G_z}{\partial t} J_z \right] \\ &= -\frac{c}{2\epsilon_0} \int d^2\mathbf{r}'_\perp \sum_{mn} \psi_{mn}(\mathbf{r}_\perp) \psi'_{mn}(\mathbf{r}'_\perp) \int_{-\infty}^t dt' \\ &\quad \times \int dz' \left[\left(\frac{\partial \lambda_-}{\partial t} \frac{\partial \Gamma_-}{\partial \lambda_-} - \frac{\partial \lambda_+}{\partial t} \frac{\partial \Gamma_+}{\partial \lambda_+} \right) \rho + \left(\frac{\partial \lambda_-}{\partial t} \frac{\partial \Gamma_-}{\partial \lambda_-} + \frac{\partial \lambda_+}{\partial t} \frac{\partial \Gamma_+}{\partial \lambda_+} \right) \frac{J_z}{c^2} \right]. \end{aligned} \quad (3.20)$$

Then using the fact that $dJ_0(x)/dx = -J_1(x)$,

$$\frac{d\Theta(\lambda_\pm^2)}{d\lambda_\pm} = 2\lambda_\pm \delta(\lambda_\pm^2) = \lambda_\pm \frac{\delta[z' \pm (z + c(t - t'))] + \delta[z' \pm (z - c(t - t'))]}{|z \pm z'|}, \quad (3.21)$$

and the completeness relation

$$\sum_{mn} \psi_{mn}(\mathbf{r}_\perp) \psi_{mn}^*(\mathbf{r}'_\perp) = \delta(\mathbf{r}_\perp - \mathbf{r}'_\perp), \quad (3.22)$$

we can express the longitudinal electric field as

$$\begin{aligned}
E_z = & \frac{c}{2\epsilon_0} \int d^2\mathbf{r}'_{\perp} \sum_{mn} k_{\perp mn} \psi_{mn}(\mathbf{r}_{\perp}) \psi'_{mn}(\mathbf{r}'_{\perp}) \int_{-\infty}^t dt' \\
& \times \int dz' \left\{ \frac{\Theta(\lambda_-^2)}{\lambda_-} J_1(k_{\perp mn} \lambda_-) \left[-(z - z') \rho + \frac{J_z(t - t')}{c} \right] \right. \\
& \quad \left. + \frac{\Theta(\lambda_+^2)}{\lambda_+} J_1(k_{\perp mn} \lambda_+) \left[-(z + z') \rho + \frac{J_z(t - t')}{c} \right] \right\} \\
& + \frac{c}{2\epsilon_0} \int_{-\infty}^t dt' \\
& \times \left\{ \Theta[z - c(t - t')] [\rho(\mathbf{r}_{\perp}, z - c(t - t'), t') - J_z(\mathbf{r}_{\perp}, z - c(t - t'), t')/c] \right. \\
& \quad - \Theta[z + c(t - t')] [\rho(\mathbf{r}_{\perp}, z + c(t - t'), t') + J_z(\mathbf{r}_{\perp}, z + c(t - t'), t')/c] \\
& \quad \left. - \Theta[-z + c(t - t')] [\rho(\mathbf{r}_{\perp}, -z + c(t - t'), t') + J_z(\mathbf{r}_{\perp}, -z + c(t - t'), t')/c] \right\}.
\end{aligned} \tag{3.23}$$

We note that the step functions in the last integral term arise from the fact that the delta functions in Eqn. (3.21) will only yield finite contributions after integration in z' when the zeros of the delta functions occur for $z' > 0$. Since it is always true that $-z - c(t - t') < 0$, the term which is proportional to $\Theta[-z - c(t - t')]$ does not contribute to the last term in Eqn. (3.23).

3.1.2 Circular Pipe Cross-Section with Longitudinal Currents

For the special case of a circular pipe with radius a , the transverse eigenfunctions and corresponding eigenvalues, which solve Eqns. (3.13), are given in cylindrical coordinates by

$$\psi_{mn}(\mathbf{r}_{\perp}) = \frac{1}{a\sqrt{\pi}} \frac{J_m(j_{mn}r/a) e^{im\theta}}{|J_{m+1}(j_{mn})|}, \tag{3.24a}$$

and

$$k_{\perp mn} = j_{mn}/a, \quad (3.24b)$$

where $J_m(x)$ is the m th order Bessel function and j_{mn} is the n th positive root of $J_m(x)$. Hence, Eqns. (3.24), along with Eqns. (3.18), (3.19), and (3.23) yield a complete description for computing the space-charge fields in a circular pipe with a cathode at $z = 0$.

We should emphasize that cylindrical symmetry is only placed on the pipe, but not on the charge and current distributions. Therefore, it is possible to use this formulation to simulate the electromagnetic fields for arbitrary longitudinal beam currents, such as those with dipole and quadrupole moments, within a cylindrical pipe.

As a numerical example, we choose the parabolic beam in the transverse direction with the zero-thickness in the longitudinal direction. The exact electromagnetic fields are given by

$$E_r(r, z, t) = \frac{4Q}{\pi \epsilon_0 \hat{r}_b^2 a^2} \sum_{n=0}^{\infty} \frac{J_1(j_{0n} \hat{r})}{j_{0n} |J_1(j_{0n})|^2} \left[\frac{2}{j_{0n} \hat{r}_b} J_1(j_{0n} \hat{r}_b) - J_0(j_{0n} \hat{r}_b) \right] \times \int_{-\infty}^{\tau} d\tau' \left[J_0(j_{0n} \hat{\lambda}_-) \Theta(\hat{\lambda}_-^2) - J_0(j_{0n} \hat{\lambda}_+) \Theta(\hat{\lambda}_+^2) \right] \quad (3.25a)$$

$$B_\theta(r, z, t) = \frac{4cQ\mu_0}{\pi \hat{r}_b^2 a^2} \sum_{n=0}^{\infty} \frac{J_1(j_{0n} \hat{r})}{j_{0n} |J_1(j_{0n})|^2} \left[\frac{2}{j_{0n} \hat{r}_b} J_1(j_{0n} \hat{r}_b) - J_0(j_{0n} \hat{r}_b) \right] \times \int_{-\infty}^{\tau} d\tau' \left[J_0(j_{0n} \hat{\lambda}_-) \Theta(\hat{\lambda}_-^2) + J_0(j_{0n} \hat{\lambda}_+) \Theta(\hat{\lambda}_+^2) \right] \left[\frac{d\hat{z}''(\tau)}{d\tau} \right]_{\tau=\tau'} \quad (3.25b)$$

and

$$\begin{aligned}
E_z = & \frac{4Q}{\pi\epsilon_0\hat{r}_b^2a^2} \sum_{n=0}^{\infty} \frac{J_0(j_{0n}\hat{r})}{j_{0n}^2|J_1(j_{0n})|^2} \left[\frac{2}{j_{0n}\hat{r}_b} J_1(j_{0n}\hat{r}_b) - J_0(j_{0n}\hat{r}_b) \right] \\
& \times \int_{-\infty}^{\tau} d\tau' \left\{ \left\{ [\hat{z} - \hat{z}''(\tau')] - (\tau - \tau') \left[\frac{d\hat{z}''(\tau)}{d\tau} \right]_{\tau=\tau'} \right\} \right. \\
& \times \left[-\frac{j_{0n}}{\hat{\lambda}_-} J_1(j_{0n}\hat{\lambda}_-) \Theta(\hat{\lambda}_-^2) + 2a^2 J_0(j_{0n}\hat{\lambda}_-) \delta(\hat{\lambda}_-^2) \right] \\
& - \left\{ [\hat{z} + \hat{z}''(\tau')] + (\tau - \tau') \left[\frac{d\hat{z}''(\tau)}{d\tau} \right]_{\tau=\tau'} \right\} \\
& \times \left[-\frac{j_{0n}}{\hat{\lambda}_+} J_1(j_{0n}\hat{\lambda}_+) \Theta(\hat{\lambda}_+^2) + 2a^2 J_0(j_{0n}\hat{\lambda}_+) \delta(\hat{\lambda}_+^2) \right] \Bigg\}. \tag{3.25c}
\end{aligned}$$

In Eqn. (3.25), the spatial and temporal coordinates are normalized to express the data of the gun in general make parameters dimensionless. The coordinates are normalized by the radius of the rf cavity, a , such that $\hat{r} = r/a$, $\hat{z} = z/a$, and $\tau = ct/a$, where c is the speed of the light. And $\hat{r}_b = r_b/a$ is the beam radius, Q is the bunch charge, and $\hat{z}''(\tau)$ is the bunch location. The detailed derivation of these fields are in the Appendix A.

Figures 3.2 and 3.3 show examples of field plots. The space-charge fields are numerically computed with the parameters of BNL 2.856 *GHz* gun. Figure 3.2 shows a 3D plot of E_r vs. r and z . There are two distinguishing features in Figure 3.2: a large pulse near $z/a = 0.225$, which is the bunch's axial location and a second smaller pulse with an outer edge at $z/a = 0.25$. The pulse at $z/a = 0.225$ represents the local electric field generated by the beam, while the second pulse represents the initial electromagnetic waves which were generated at $t = 0$ when the beam is emitted. Since the time in Figure 3.2 is $t = 0.25a/c$, the point $z/a = 0.25$ corresponds to the location of the causality condition, $z = ct$. From Figure 3.2, it is also seen that the fields are zero when $z > ct$, which illustrates the effect of the causality condition.

Figure 3.3 shows a plot of E_z vs. r and z . Figure 3.3 shows similar features as

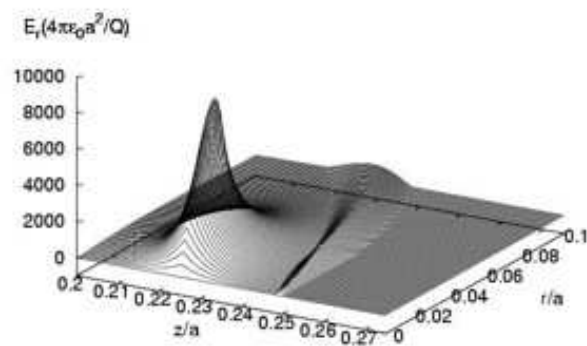


Figure 3.2: Plots of E_r vs. r and z , for $t = 0.25a/c$.

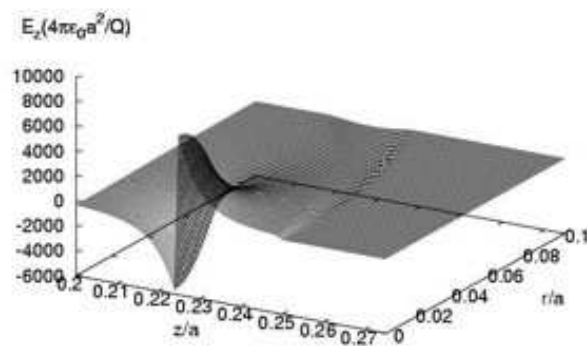


Figure 3.3: Plots of E_z vs. r and z , for $t = 0.25a/c$.

Figure 3.2, namely, two pulses - one near the beam and one generated by the initial waves due to bunch emission, i.e., the transient electromagnetic pulse due to the transient radiations. The sharp discontinuity in the pulse near the beam is located precisely at the bunch's location, and denotes the point at which the sign of the electric field changes.

3.1.3 Rectangular Pipe Cross-Section with Arbitrary Currents

In contrast to the previous example, the explicit solutions of the electromagnetic space-charge potentials and fields to the rectangular pipe cross section with the arbitrary beam currents can be easily found. In this system, the electron beam has transverse currents as well as the longitudinal currents, i.e., $\mathbf{J}(\mathbf{r}, t) = J_x(\mathbf{r}, t)\hat{e}_x + J_y(\mathbf{r}, t)\hat{e}_y + J_z(\mathbf{r}, t)\hat{e}_z$.

As in the previous case, the electromagnetic potentials $\phi(\mathbf{r}, t)$ and $\mathbf{A}(\mathbf{r}, t)$, may be solved in the Lorenz gauge. The difference in this case, however, is that $\mathbf{A}(\mathbf{r}, t)$ will also have transverse components instead of only the longitudinal component. For $\rho(\mathbf{r}, t)$ and $\mathbf{J}(\mathbf{r}, t)$ which satisfy the continuity equation, Eqn. (3.4), the potentials are given by

$$\left(\nabla^2 - \frac{1}{c^2} \frac{\partial^2}{\partial t^2}\right) \phi(\mathbf{r}, t) = -\frac{\rho(\mathbf{r}, t)}{\epsilon_0}, \quad (3.26a)$$

and

$$\left(\nabla^2 - \frac{1}{c^2} \frac{\partial^2}{\partial t^2}\right) \mathbf{A}(\mathbf{r}, t) = -\mu_0 \mathbf{J}(\mathbf{r}, t), \quad (3.26b)$$

and satisfy the boundary conditions listed in Eqns. (3.6), (3.7), and (3.8).

Similar to the previous case, the solutions to the electromagnetic potentials can be expressed in terms of four time-dependent Green's functions, which we denote by

$G_i(\mathbf{r}, t; \mathbf{r}', t')$, where $i = \phi, x, y$, and z . The potentials are given by

$$\phi(\mathbf{r}, t) = \frac{1}{\epsilon_0} \int_{-\infty}^t \int G_\phi(\mathbf{r}, t; \mathbf{r}', t') \rho(\mathbf{r}', t') d^3\mathbf{r}' dt', \quad (3.27a)$$

and

$$A_\alpha(\mathbf{r}, t) = \mu_0 \int_{-\infty}^t \int G_\alpha(\mathbf{r}, t; \mathbf{r}', t') J_\alpha(\mathbf{r}', t') d^3\mathbf{r}' dt', \quad (3.27b)$$

where $\alpha = x, y$, and z . All four Green's functions satisfy the differential equation

$$\left(\nabla^2 - \frac{1}{c^2} \frac{\partial^2}{\partial t^2} \right) G_i = -\delta(\mathbf{r} - \mathbf{r}') \delta(t - t'), \quad (3.28)$$

From the boundary conditions as in Eqns. (3.6), (3.7), and (3.8), the Green's functions are subject to the following conditions, namely

$$G_\phi|_{\text{surf}} = 0, \quad (3.29a)$$

$$G_x|_{y=0, y=W} = \frac{\partial G_x}{\partial x} \Big|_{x=0, x=L} = 0, \quad (3.29b)$$

$$G_y|_{x=0, x=L} = \frac{\partial G_y}{\partial y} \Big|_{y=0, y=W} = 0, \quad (3.29c)$$

$$G_z|_{y=0, y=W}^{x=0, x=L} = \frac{\partial G_z}{\partial z} \Big|_{z=0} = 0, \quad (3.29d)$$

as we specify the sides of the pipe by $x = 0$, $x = L$, $y = 0$, and $y = W$.

The solutions to G_i can be readily constructed in a fashion similar to the previous case, i.e.,

$$G_\phi = \frac{2c}{LW} \sum_{m=1}^{\infty} \sum_{n=1}^{\infty} \sin\left(\frac{m\pi x}{L}\right) \sin\left(\frac{m\pi x'}{L}\right) \sin\left(\frac{n\pi y}{W}\right) \sin\left(\frac{n\pi y'}{W}\right) [\Gamma_- - \Gamma_+], \quad (3.30a)$$

$$G_x = \frac{2c}{LW} \sum_{m=1}^{\infty} \sum_{n=1}^{\infty} \cos\left(\frac{m\pi x}{L}\right) \cos\left(\frac{m\pi x'}{L}\right) \sin\left(\frac{n\pi y}{W}\right) \sin\left(\frac{n\pi y'}{W}\right) [\Gamma_- - \Gamma_+], \quad (3.30b)$$

$$G_y = \frac{2c}{LW} \sum_{m=1}^{\infty} \sum_{n=1}^{\infty} \sin\left(\frac{m\pi x}{L}\right) \sin\left(\frac{m\pi x'}{L}\right) \cos\left(\frac{n\pi y}{W}\right) \cos\left(\frac{n\pi y'}{W}\right) [\Gamma_- - \Gamma_+], \quad (3.30c)$$

$$G_z = \frac{2c}{LW} \sum_{m=1}^{\infty} \sum_{n=1}^{\infty} \sin\left(\frac{m\pi x}{L}\right) \sin\left(\frac{m\pi x'}{L}\right) \sin\left(\frac{n\pi y}{W}\right) \sin\left(\frac{n\pi y'}{W}\right) [\Gamma_- + \Gamma_+]. \quad (3.30d)$$

where

$$k_{\perp mn} = \sqrt{\left(\frac{m\pi}{L}\right)^2 + \left(\frac{n\pi}{W}\right)^2}. \quad (3.31)$$

The reason why it is relatively straightforward to construct the potential solutions in this geometry for arbitrary beam currents as opposed to a general curvilinear pipe, such as a circular pipe, is due to two reasons. First, in the rectangular case for which it is appropriate to utilize Cartesian coordinates, Eqn. (3.26b) can be separated into three component equations. In these equations, there is no coupling between the two transverse directions, i.e., J_x generates A_x but not A_y , and vice versa. This is not the case, however, in general curvilinear coordinates, in which both A_r and A_θ are generated when either J_r or J_θ are present.

Second, in order to satisfy the Lorenz gauge condition with the potentials, it is necessary to change the order of differentiation in the eigenfunctions from unprimed(field) coordinates to primed(source) coordinates using integration by parts, and then to exploit the continuity equation. This was readily accomplished for longitudinal currents when the eigenfunctions in the longitudinal direction and in time are sinusoidal as in Eqn. (3.14). Since the transverse eigenfunctions for the rectangular case are also given by sinusoidal functions, the gauge condition can be readily satisfied for the transverse potentials as well.

3.2 Numerical Implementation

3.2.1 Development of IRPSS Code

We develop the computational code, IRPSS (Indiana University Rf Photoinjector Source Simulator), for computing the electromagnetic space-charge fields. IRPSS is capable of solving the space-charge fields with Green's function methods numerically.

We assume that the system is cylindrically symmetric, so that we can use the results of the previous section. We also assume that the beam is moving through the prescribed trajectory, which is calculated with the presence of the external rf field,

$$E_z^{\text{rf}} = E_0^{\text{rf}} \cos(kz) \sin(\omega t + \varphi), \quad (3.32)$$

where E_0 is the peak rf electric field, ω is the rf frequency, and φ is the injection rf phase [39]. This implies that there is only the longitudinal beam currents. Henceforth, the electromagnetic space-charge fields are computed for the bunch with the prescribed trajectory.

The numerical examples in this work are using the parameters of the two rf photoinjectors, which are the BNL 2.856 GHz and the ANL AWA 1.3 GHz guns. The main gun parameters are given in the Table 3.1.

The distribution of the bunched beam can be generalized to several types of distribution functions, such as parabolic, Gaussian, and waterbag in 3-dimensional directions. In particular, the charged particle beam distribution in the rf photoinjector has a short bunch length, which is much smaller than the transverse coordinates of the beam. First, we assume that the beam has the finite transverse size with the zero thickness in the longitudinal direction, and then the bunched beam consists of many sliced (zero thickness) beams. The multi-sliced bunched beam will be discussed in the following Section.

	BNL	ANL
rf frequency (GHz)	2.856	1.3
peak rf field (MV/m)	100	25 ~ 77
rf injection phase (deg)	68	65
radius of the cavity (m)	0.04111	0.0908
radius of the beam (mm)	1	1
charge of the beam (nC)	1	1

Table 3.1: The rf photoinjector beam parameters of the BNL 2.856 GHz and the ANL AWA 1.3 GHz guns

The space-charge fields are determined by the beam profile, which must be updated at each time step of simulations. In this work, we restrict that the beam density function is not changed with time and uncoupled between the longitudinal and transverse coordinates, then it can be separated into longitudinal- and time-dependent parts and a transverse-dependent one. To simplify the problem, we assume that there is no transverse motion. Using the completeness of the transverse eigenfunctions, the beam density function can be expanded in terms of the transverse eigenfunctions, $\psi_{mn}(\mathbf{r}_\perp)$, i.e.,

$$\rho(\mathbf{r}, t) = \sum_{m,n} \rho_{mn}(z, t) \psi_{mn}(\mathbf{r}_\perp) \quad (3.33)$$

where $\rho_{mn}(z, t)$ are the expansion coefficients, which depend on the longitudinal coordinates and time, m and n are mode numbers of transverse eigenfunctions, and \mathbf{r}_\perp is the transverse coordinates. From Eqn. (3.33), there needs to be enough transverse eigenmodes in order to resolve the transverse profile of the fields. The eigenfunction, $\psi_{mn}(\mathbf{r}_\perp)$, is determined by the given transverse beam distribution.

For the cylindrically symmetric beam, the azimuthal mode number, m , is zero, hence, only the radial eigenmode number is important for the expansion. For this cylindrical beam configuration, the eigenfunctions can be simply expressed as

$$\psi_{0n}(\mathbf{r}_\perp) = \frac{1}{a\sqrt{\pi}} \frac{J_0(j_{0n}r/a)}{|J_1(j_{0n})|} \quad (3.34)$$

where j_{0n} is the n^{th} root of the zeroth order Bessel function. In the following sections, we will use the radially parabolic shape of the beam distribution:

$$\rho(\mathbf{r}, t) = \frac{2Q}{\pi r_b^2} \Theta(r_b - r) \left(1 - \frac{r^2}{r_b^2}\right) \delta[z - z''(t)] \quad (3.35)$$

This function has no azimuthal dependence, i.e., it is cylindrically symmetric. The delta function indicates the beam has zero thickness in the longitudinal direction. $z''(t)$ contains the trajectory information of the charge, the beam has total charge of Q . Therefore, the beam distribution function can be expanded as

$$\rho(\mathbf{r}, t) = \frac{8Q}{\pi r_b^2} \sum_n \frac{J_0(j_{0n}r/a)}{j_{0n}^2 |J_1(j_{0n})|^2} \left[\frac{2}{j_{0n}r_b/a} J_1(j_{0n}r_b/a) - J_0(j_{0n}r_b/a) \right] \delta[z - z''(t)] \quad (3.36)$$

The Eqn. (3.36) is very similar to the our Green's function solution of the transverse electromagnetic fields with the given density function, Eqn. (3.33).

Figures 3.4 shows plots of the radial beam density distribution for different eigenmode summations with two different sizes of the beam radius, $r_b/a = 0.02433$ and 0.5 . By comparing two Figures 3.4(a) and 3.4(b), we note that the convergence rates of the series of the density function (Eqn. (3.36)) strongly depends on the transverse size of the beam. The convergence rate is much more slow for the small radial beam size. For the beam radius of $r_b/a = 0.5$, even 100 eigenmode is enough to resolve the density function. For the beam radius of $r_b/a = 0.02433$, the density function is oscillating around the exact solution (solid:red), therefore, and at least 2,000 eigenmodes are needed to get less than 1% numerical error.

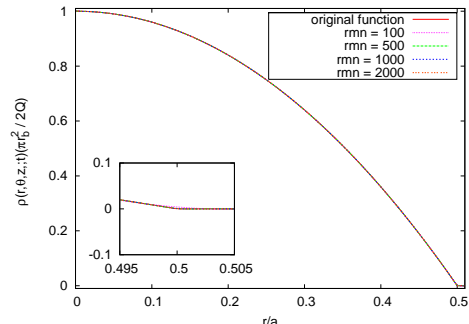
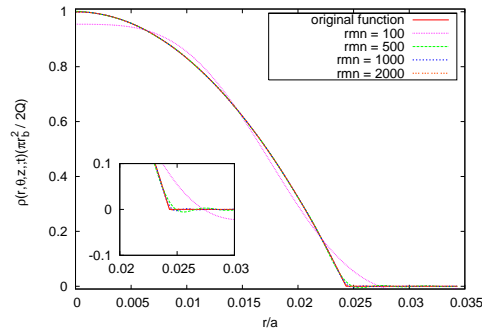
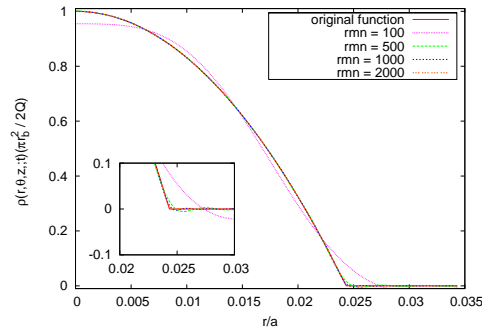
(a) $r_b/a = 0.5$ (b) $r_b/a = 0.02433$ (c) $r_b/a = 0.0111$

Figure 3.4: The plots of the beam distribution function with different beam sizes. The original function is plotted without the expansion, and **rmn** is the radial eigenmode number.

For numerical calculations of the fields, we are required to perform the transverse eigenmode summations, a time integration, spatial integrations over three dimensional coordinates, and the temporal and spatial derivatives for calculating the fields. In order to accurately simulate the space-charge fields within less than 1% error, however, we need to consider the computational requirements for these numerical implementations. Since the zero-thickness parabolic beam is assumed with the cylindrically symmetric cavity geometry in this work, the spatial integrations are handled analytically. Due to azimuthal symmetry, there is only radial eigenmode summations and no azimuthal mode summations. We now show the computational requirements for high-accuracy space-charge field calculations.

3.2.2 Eigenmode Summation

With the cylindrically symmetric beam distribution function, described in the Equation (3.35), the radial space-charge field is given by

$$E_r(\mathbf{r}, t) = \frac{4Q}{\pi\epsilon_0 r_b^2} \sum_n \frac{J_0(j_{0n}r/a)}{j_{0n}|J_1(j_{0n})|^2} \left[\frac{2}{j_{0n}r_b/a} J_1(j_{0n}r_b/a) - J_0(j_{0n}r_b/a) \right] \times \int_{-\infty}^t dt' [J_0(j_{0n}\lambda_-/a) \Theta(\lambda_-^2) - J_0(j_{0n}\lambda_+/a) \Theta(\lambda_+^2)] \quad (3.37)$$

where λ_{\pm}^2 are given by

$$\lambda_{\pm}^2 = c^2 (t - t')^2 - [z \pm z''(t')]^2 \quad (3.38)$$

We can estimate the required number of radial modes to model for a charge density with a form given by Eq (3.35). In general, a large number of radial modes are necessary to reconstruct the type of charge density for a given beam radius, r_b . For large mode numbers, i.e., $j_{0n}r/a \gg 1$,

$$J_0(j_{0n}r/a) \approx \sqrt{\frac{2a}{\pi j_{0n}r}} \cos\left(j_{0n}\frac{r}{a} - \frac{\pi}{4}\right) \quad (3.39)$$

is the asymptotic form for the radial mode expansion.

Since a cosine function has a period 2π , it is necessary that in order to have a sufficient number of modes to model the beam charge density,

$$j_{0M} \frac{r_b}{a} \gg 2\pi \quad (3.40)$$

where M is the largest required radial mode number. The number of transverse eigenmodes necessary for accurately determining the fields is inversely proportional to the transverse size of the beam. The necessary mode number is inversely proportional to the ratio between the beam size, r_b and the radius of the cavity, a , i.e.,

$$j_{0M} \gg \frac{2\pi}{r_b/a} \approx 12.57 > j_{0,4}, \quad (3.41)$$

for $r_b/a = 0.5$. Choosing $M \sim 40$ satisfies this condition. From the inequality relation, The appropriate transverse eigenmode numbers can be estimated. For example, with $r_b/a = 0.02433$, it is necessary that,

$$j_{0M} \gg \frac{2\pi}{r_b/a} \approx 258.25 > j_{0,82}. \quad (3.42)$$

Choosing $M > 1000$ satisfies this condition.

In Figure 3.5, the radial electric fields are plotted as a function of r for 100, 500, 1000, and 2000 eigenmodes for the charge density shown in Figure 3.4(b). For $ct/a = 0.25$ and $z/a = 0.225$, the radial electric fields are oscillating with r for small values of eigenmodes. In order to model the fields within 1% accuracy, it is necessary to sum over at least 2000 modes.

3.2.3 Numerical Time Integration

In order to resolve the fields related with the beam motion, the integration time step, $\Delta t'$ must be smaller than the characteristic time scale of the system. Since the

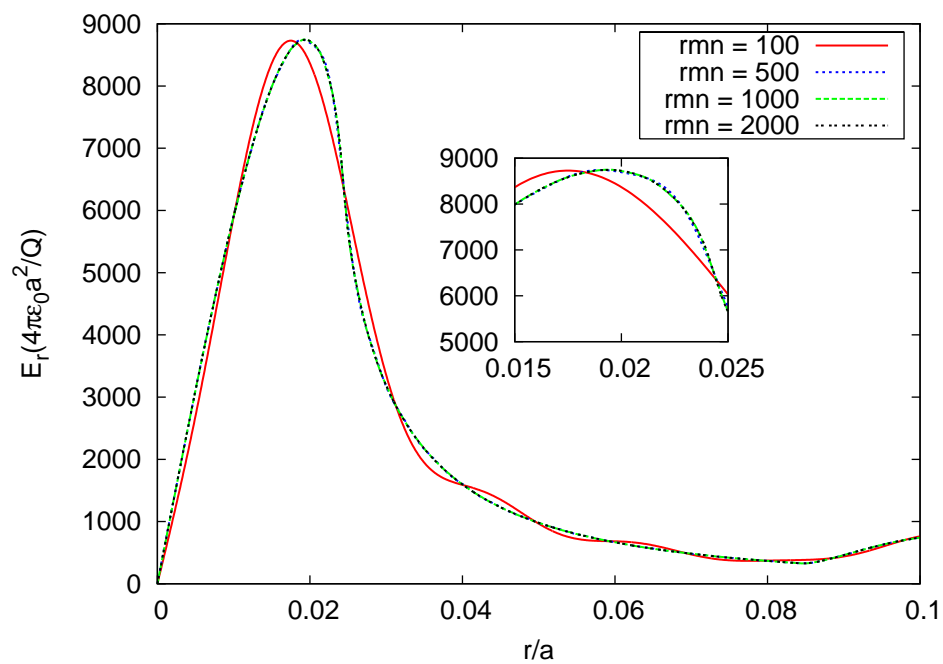


Figure 3.5: E_r vs. r for different eigenmode number, rmn

electron beam is accelerated relativistically by the external rf field, the characteristic time of the photoinjector system, τ_{dyn} is given by

$$\tau_{dyn} \sim \gamma_b m_e c e / E. \quad (3.43)$$

where γ_b is the relativistic Lorentz factor of the beam. This yields $\Delta t' \ll \tau_{dyn}$. In addition to this limit, however, we need more restrictions for the time integration step to reduce the numerical errors. There is another restriction on the time-integration.

The formula for the space-charge fields using the Green's function method contains time integral factors, which store the trajectory history of the bunch. Due to the complexities of the integrands, however, it is necessary to integrate these numerically, and to consider the relation between the integration time step and the eigenmode number. Each field equation includes similar Bessel function type arguments: $J_0(j_{0n}\lambda_-/a)\Theta(\lambda_-^2)$ and $J_0(j_{0n}\lambda_+/a)\Theta(\lambda_+^2)$. The former represents the real charge, while the latter reads the induced image charge by the cathode geometry. The function $\lambda_{\pm}(z, t; t')$ are given by

$$\lambda_{\pm}^2 = c^2(t - t')^2 - [z - z''(t')]^2 \quad (3.44)$$

where t' is the time integral variable and varies from $-\infty$ to t . The step functions represent the causality conditions of the field, which occur due to the finite speed of light. For modeling the transient effects near the front of the bunch, these factors become very important [21].

Figure 3.6 shows $J_0(j_{0n}\lambda_-/a)\Theta(\lambda_-^2)$ as functions of t' for different transverse mode number, n , when t is fixed. As n increases, $J_0(j_{0n}\lambda_-/a)\Theta(\lambda_-^2)$ oscillates with time, and these oscillations are smooth. But there are discontinuities at certain values of t and z , which are generated by the step function. These discontinuities generate numerical time integration errors, so that the time step, $\Delta t'$, must be small enough to reduce errors around these points. This imposes a maximum limit on the time step.

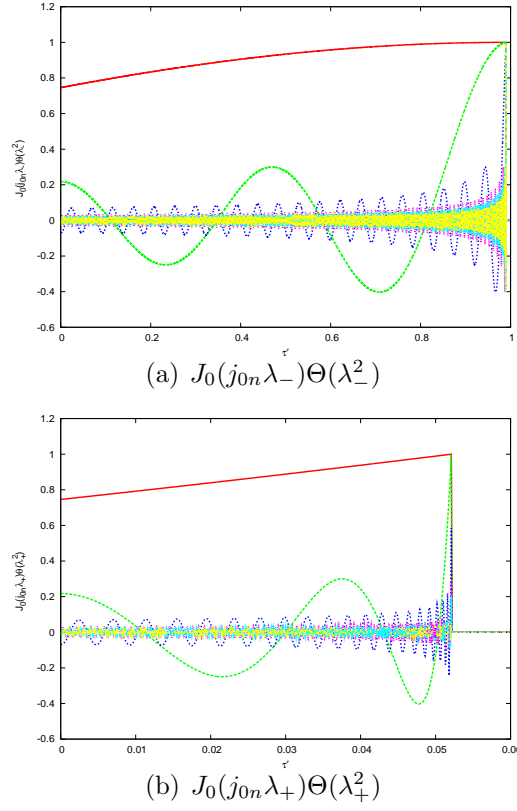


Figure 3.6: Plots of the arguments of the time integration for 1 (red), 10 (green), 100 (blue), 500 (pink), 1000 (light blue), and 2000 (yellow) eigenmode numbers.

The time step must be chosen sufficiently small such that

$$j_{0n} \frac{c\Delta t'}{a} \ll 2\pi, \quad (3.45)$$

so that time integration over the Bessel functions are accurate. Using $j_{0M} \frac{r_b}{a} \gg 2\pi$, we find

$$\Delta t' \ll \frac{0.01 r_b}{c}. \quad (3.46)$$

From Figure 3.6, however, the oscillation time is very short for the large eigenmode number, thus we need much smaller time step.

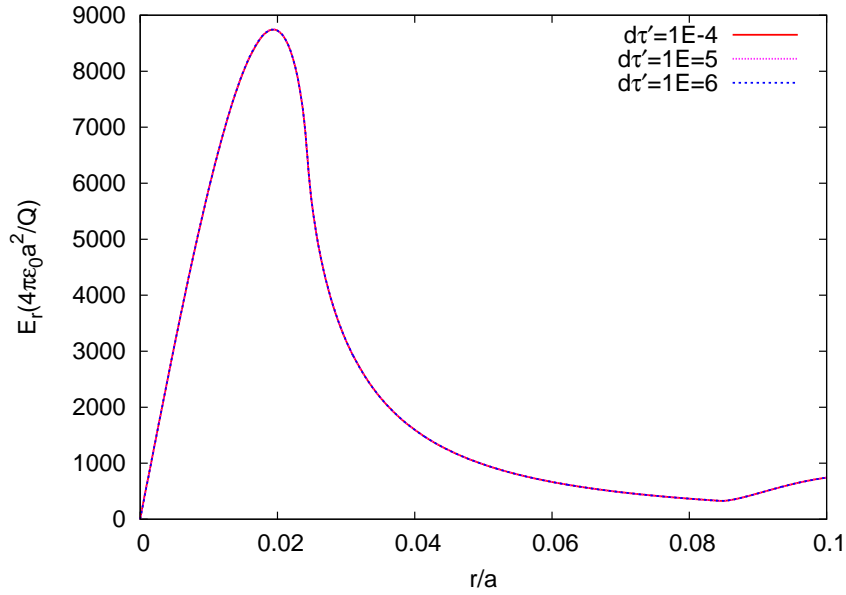


Figure 3.7: E_r vs. r for different numerical integration time steps:

$$d\tau' = cdt'/a = 10^{-4}, \quad 10^{-5}, \quad \text{and} \quad 10^{-6}$$

Figures 3.7 and 3.8 show E_r and E_z as functions of z for different time steps, $\Delta t'$, with $t/a = 0.25$. Here, τ' is the normalized time, ct'/a . The maximum mode number is chosen to be 2000 to see only errors by the numerical integration time step. For

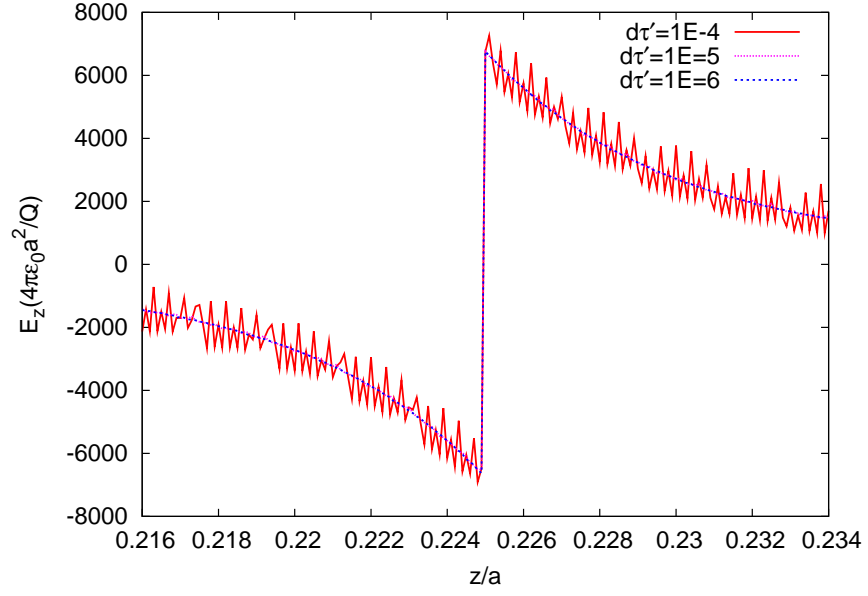


Figure 3.8: E_z vs. z for different numerical integration time steps:
 $d\tau' = cdt'/a = 10^{-4}$, 10^{-5} , and 10^{-6}

the time step, $cdt'/a = 10^{-4}$, 10^{-5} and 10^{-6} , there is no significant difference in E_r vs. r . Since there is no radial dependence in the time integration factor, the effect of the time step size is very small with fixed z and t for E_r .

For the E_z calculations, however, the longitudinal field strongly depends on the beam trajectory, which is the function of the time integral variable, t' . Figure 3.8 shows the dependence of the time step size along the axis of the symmetry. The oscillation periods are determined by the characteristic spatial step size, Δz , the transverse eigenmode number, n , and the integration step size, $\Delta t'$. The smaller Δz reduces the period of the oscillation, however it also requires much smaller $\Delta t'$. The smaller $\Delta t'$ reduces the amplitude of the oscillation. This is generalized by,

$$c\Delta t' < \Delta z \ll r_b/\gamma_b \quad (3.47)$$

The relativistic Lorentz factor of the beam, γ_b , is assigned to correct the relativistic effect of the beam. We can see that $c\Delta t'/a = 10^{-4}$ is not small enough to resolve the fields, even though it is about factor of 200 times smaller than r_b/a .

3.2.4 Multi Slice Bunch Simulation Method

Since the bunched beam has finite size in the longitudinal direction, the zero-thickness beam is not adequate for designing the real beam. Thus the multi-sliced bunch model is introduced to make it realistic. We assume that (1) there are a finite number of zero-thickness sliced beams. (2) Each slice has an equal number of particles. And (3) these slices are uniformly distributed over the bunch length. We try to find out how many bunches are needed to express the finite thickness beam.

Suppose that the total bunch length is $t_l = 9$ ps. The bunch length varies with the frequency, injection phase, and wave number of the rf electric field. Since each slice is emitted at a different time, its injection phase is slightly different. However, a 9 psec bunch length is relatively short compared to the time scale of the rf field. Thus, we

can assume that all slices have the same trajectory configurations, i.e., all slices are launched at the same phase, and they are distributed uniformly in time. Therefore, if the central slice of the bunch is at time $t = t_0$, then the i^{th} ($1 \leq i \leq N/2$) slice at the head of the bunch is at time $t_i = t_0 + it_l/N$, since the time interval between two adjacent slice for the $N + 1$ slices is t_l/N .

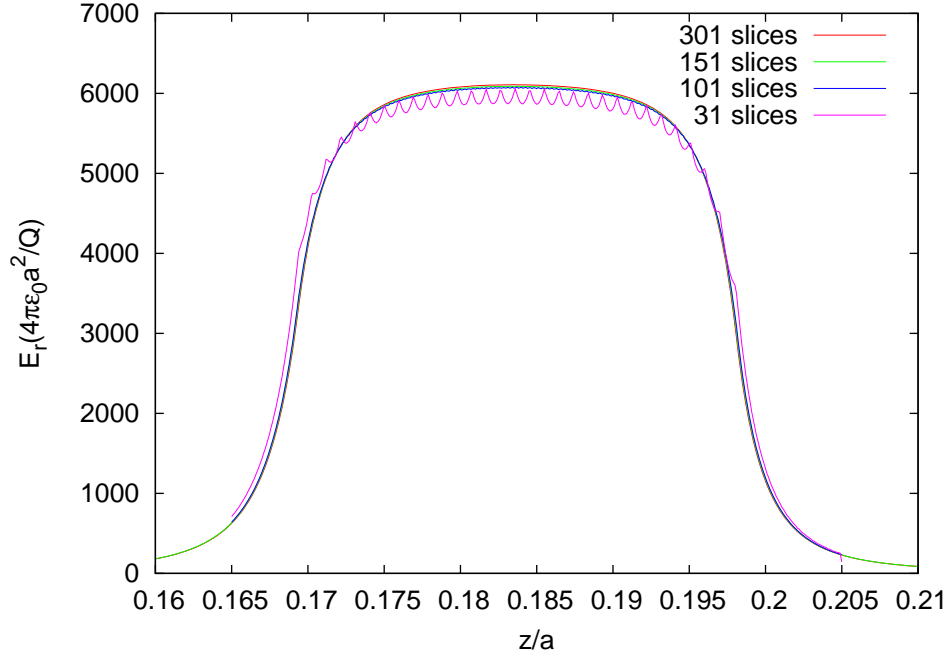


Figure 3.9: E_r vs. z at $r = r_b$ for different numbers of slices

Now, we set up the uniformly spaced (in time), equally charged $N + 1$ slices, which form the complete bunch. In this section, we use the AWA rf photoinjector gun of the ANL. In order to reduce other considerable errors, the following numerical parameters are used: the eigenmode number, $n = 1000$, the spatial step size, $\Delta z/a = 10^{-4}$, and the numerical time integration step, $\Delta t' = 5 \times 10^{-5}$.

Figures 3.9 to 3.11 show plots of the space-charge electric fields as a function of

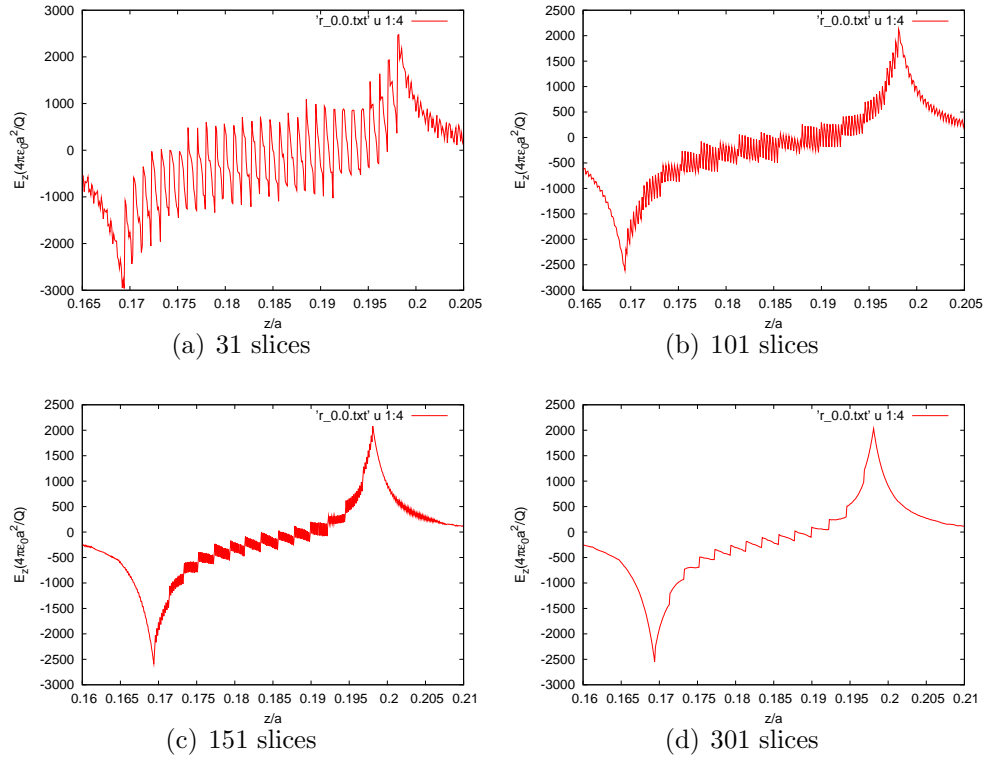


Figure 3.10: E_z vs. z at $r = 0$ for different numbers of slices

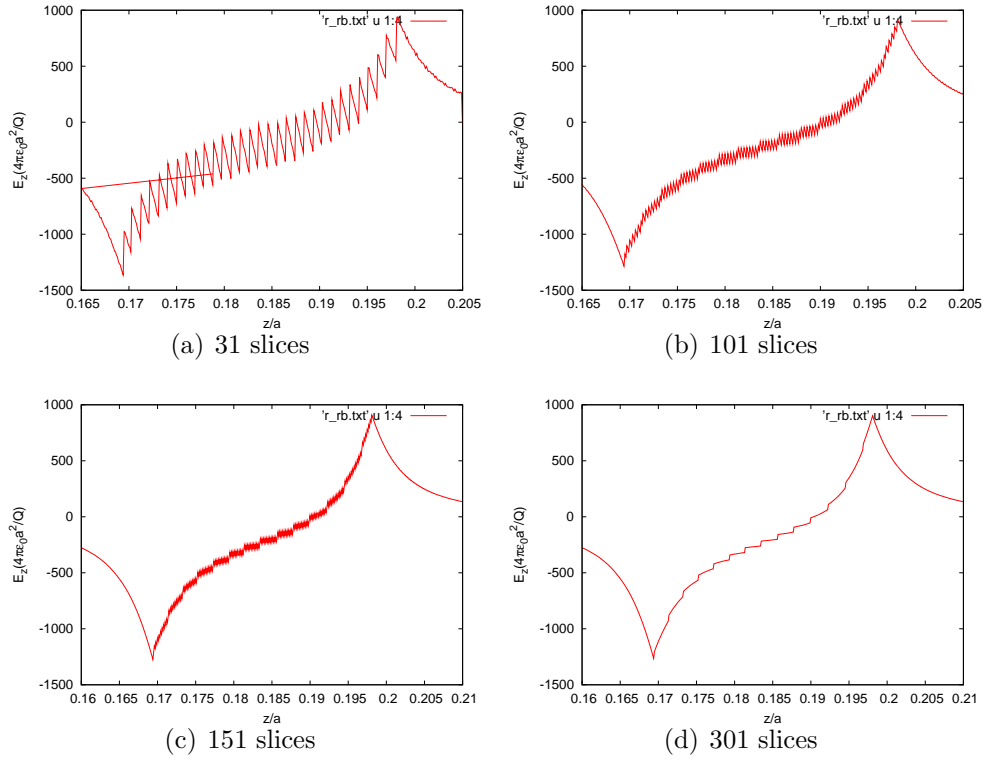


Figure 3.11: E_z vs. z at $r = r_b$ for the different number of slices

the normalized longitudinal coordinate, z/a , for the different number of slices. The fields are at $ct/a = 0.185$, and those are plotted around the bunch.

In the Figure 3.9, the radial field of 31-slice model is rapidly oscillating along the axis, although the errors are still small. These oscillations are due to the peak of each slice. Thus 31 slices are not enough to resolve the radial electric field. But, for more than 101 slices, the fields become smoothed out with small discrepancies, which are ignorable errors.

In Figures 3.10 and 3.11, beyond the 101 slices, the peak fields do not vary much with the number of slices. However, the axial fields are oscillating even with 151 slices. The amplitudes of the oscillation are reduced with the position of r . From these plots, we can estimate that more than 300 slices can represent the finite size of the beam for the bunch length of 9 ps. If the bunch length is shortened or lengthened, the required number of slices are decreased or increased, respectively.

3.2.5 Benchmark Modeling and Comparison

It is essential when developing a numerical algorithm to find benchmarks by which the algorithm may be compared. The benchmark that we now present is based on an analytical result. In particular, we test the case of a source with cylindrical pipe of radius a whereby a bunch of total charge Q is emitted from the cathode at time $t = 0$ with a constant uniform velocity $\mathbf{V} = V\hat{\mathbf{e}}_z$. The bunch is assumed to be cylindrically symmetric, have zero longitudinal length, and have finite size in the transverse directions. We assume that the radial density of the bunch is parabolic with radius r_b and fixed in time. The charge and current densities are given by

$$\rho(\mathbf{r}, t) = \rho_{\perp}(\mathbf{r}_{\perp}) \delta(z - Vt), \quad (3.48a)$$

and

$$J_z(\mathbf{r}, t) = \rho_{\perp}(\mathbf{r}_{\perp}) V \delta(z - Vt), \quad (3.48b)$$

where $\rho_{\perp}(\mathbf{r}_{\perp}) = (2Q/\pi r_b^2 \Theta(r_b - r)(1 - r^2/r_b^2))$.

Now we compare the fields of this system to the fields of another system where there are two bunches $Q_1 = Q$ and $Q_2 = -Q$, with velocities $\mathbf{V}_1 = V\hat{\mathbf{e}}_z$ and $\mathbf{V}_2 = -V\hat{\mathbf{e}}_z$, respectively. The trajectories of the two bunches are configured, such that at time $t = 0$, the two bunches will overlap. The charge and current densities of this second system are given by

$$\rho_1(\mathbf{r}, t) = \rho_{\perp}(\mathbf{r}_{\perp}) \delta(z - Vt), \quad (3.49a)$$

$$J_{z1}(\mathbf{r}, t) = \rho_{\perp}(\mathbf{r}_{\perp}) V \delta(z - Vt), \quad (3.49b)$$

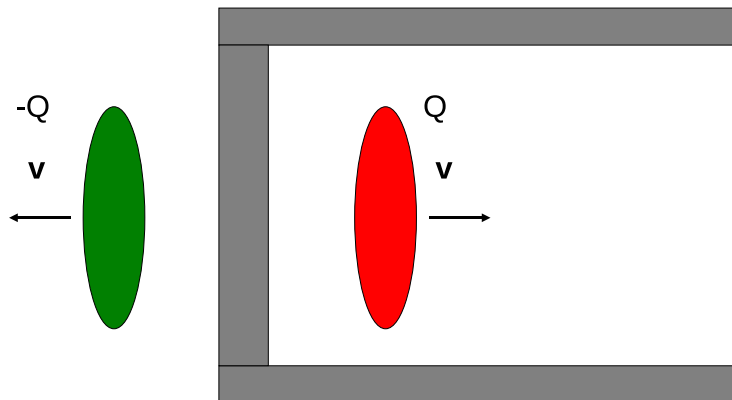
$$\rho_2(\mathbf{r}, t) = -\rho_{\perp}(\mathbf{r}_{\perp}) \delta(z + Vt), \quad (3.49c)$$

and

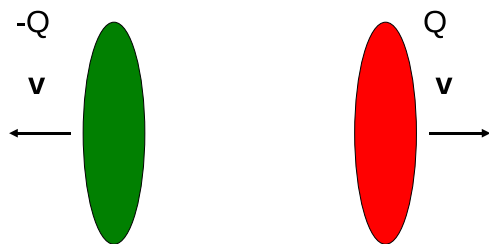
$$J_{z2}(\mathbf{r}, t) = \rho_{\perp}(\mathbf{r}_{\perp}) V \delta(z + Vt). \quad (3.49d)$$

Figure 3.12 shows the schematic comparison diagrams between the benchmark model and our model. In the benchmark model, there is no cathode boundary. However, there are two beams, which having opposite polarities and moving in opposite direction, to represent the image charge effect by the cathode. Assuming that the beam is moving with the constant speed, e.g., $v = 0.9c$.

The fields for each bunch in the second system can be easily computed by finding the electric field in the rest frame of the bunch, and then Lorentz transforming back to the laboratory frame. In the second system, the bunch Q_2 represents the image bunch which is found in the first system due to the presence of the cathode at $z = 0$. For specific regions of space and time, e.g., before wave reflection from the pipe has occurred ($t < 2a/c$ for $r = 0$) and after the initial electromagnetic shock front due to bunch emission has passed ($z < ct$ for $r = 0$), the electromagnetic fields produced by the first system will be exactly the same as those of the second system. We note that,



(a) IRPSS Model



(b) Benchmark Model

Figure 3.12: (a) IRPSS simulation of a disk bunch of charge emitted at time $t = 0$ from the cathode surface moving uniformly with speed v (b) Analytical model of two disks of charge moving uniformly in opposite directions for all time and intersecting at $t = 0$

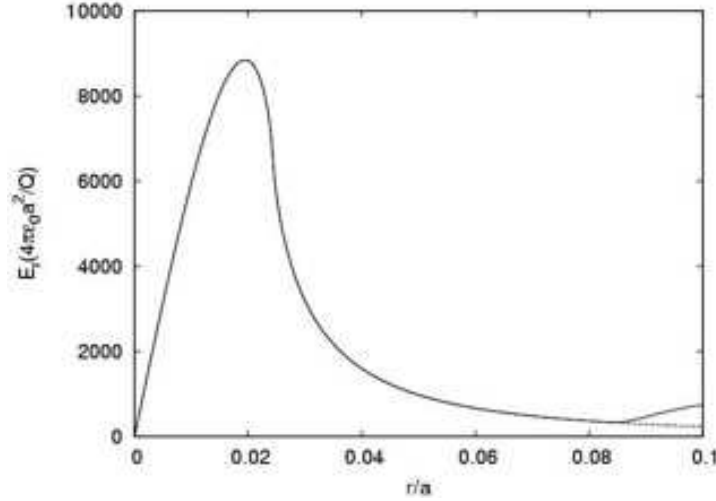


Figure 3.13: Plots of E_r vs. r at the bunch location $z/a = 0.225$, showing the numerical scheme (solid line) and the benchmark example (dashed line).

in the first system, the fields should be exactly zero when $z > ct$, since the causality condition prevents any waves from propagating beyond $z = ct$.

Figures 3.13 and 3.14 show plots of the normalized radial and longitudinal electric fields using the beam densities given in Eqn. (3.48) and the field equations given by Eqns. (3.18) and (3.23). In the simulation, the following parameters were chosen: the beam velocity is $V = 0.9c$, the beam radius corresponds to the experimental beam radius in the BNL 2.856 GHz photocathode experiment [40], i.e., $r_b/a = 0.0243$, and the time is $t = 0.25a/c$. In order to accurately compute the fields, we set $M = 2000$ and $\Delta t' = 10^{-6}a/c$.

Figure 3.13 shows a plot (solid line) of E_r vs. r at the bunch's location $z/a = 0.225$. In addition, a plot of the normalized radial electric field from the second (benchmark) system is shown (dashed line), which uses the densities in Eqns. (3.49) to compute

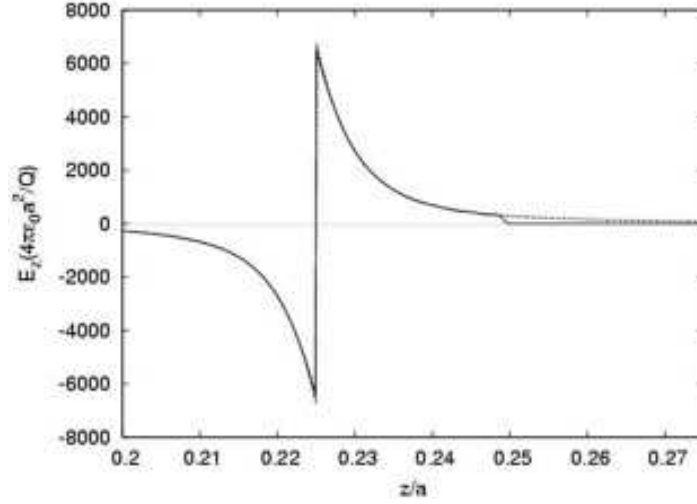


Figure 3.14: Plots of E_z vs. z , showing the numerical scheme (solid line) and the benchmark example (dashed line).

the fields. From Figure 3.13, it is seen that there is excellent agreement, i.e., less than 1% error, between the numerical scheme and the benchmark example for $r/a \leq 0.085$. The difference between the fields in Figure 3.13 for $r/a \geq 0.085$ is attributed to the initial electromagnetic pulse generated at bunch emission. Essentially, one can view this transient electromagnetic pulse as being due to transition radiation, which occurs when the electron bunch is spontaneously generated at the cathode surface at time $t = 0$. Obviously, this electromagnetic pulse would not be present in the benchmark example since the two bunches defined by Eqns. (3.49) are uniformly moving for all time. It is therefore necessary to wait a sufficient amount of time for the initial transient pulse to pass in order for the fields in the benchmark case and the numerical case to match.

Figure 3.14 shows a plot of E_z vs. z at $r = 0$ for both the numerical scheme (solid line) as well as the benchmark example (dashed line). We see excellent agreement,

i.e., less than 1% error between the fields for locations which are not close to the second pulse at $z = ct$. For $z > ct$, the numerical scheme correctly shows that the fields are zero according to the causality condition.

3.3 Discussion

In the future, we are planning to expand the analysis in this section by including the effect of one or more metallic irises on space-charge fields. Irises are typically found in photoinjector systems, and the first iris along with the cathode and cavity walls usually define the boundary of the first half-cell in a photoinjector. The irises will affect the space-charge fields with the presence of additional image charges and image currents. There are a variety of methods which can be utilized for including the effects of irises. For example, in Ref. [25, 26], the authors expanded the space-charge fields in each region of injector space, i.e., before and after the iris, using eigenfunctions which locally satisfy the correct boundary conditions. The coefficients of the field expansions were found numerically by applying boundary conditions, such as field continuity, at the location of the iris. Usually, this technique results in determining the elements of a large $N \times M$ matrix where N and M are the number of eigenmodes used in expanding the fields before and after the iris. Another technique with which the present authors are actively pursuing is a method developed by H. Bethe that expands the fields due to the iris(es) using a perturbative multipole field expansion [41]. This technique starts by solving the space-charge fields assuming that no iris is present, i.e., that the geometry of the conductor is a pillbox. These lowest order electromagnetic fields can then be used to compute the induced electric and magnetic multipole moments of the iris to all orders in b/a , where the iris radius is b and the cavity radius is a . The total space-charge field can then be represented as the zeroth order fields plus the fields due to the electric and magnetic multipoles for each iris.

Chapter 4

Application to the RF Photoinjector Experiments

In order to simulate the beam dynamics and electromagnetic space-charge fields in the rf photocathode gun, including those near the cathode, a new code called, IRPSS (Indiana Rf Photocathode Source Simulator), has been developed. IRPSS can calculate the electromagnetic space-charge fields based on a time-dependent Green's function method [42, 21, 43, 44], and it can track the beam evolution throughout the first half cell. In order for a one-to-one comparison, we have written an electrostatic code, which is also based on a Green's function method. To be specific, the electrostatic code incorporates both \mathbf{E} and \mathbf{B} space-charge fields, but does not include time-retardation effects. While each code has a different space-charge solver, both codes utilize identical tracking algorithms.

4.1 Simulation Set-Up for the RF Photoinjector

4.1.1 Prescribed Trajectory

In the IRPSS code, we first calculate the electromagnetic space-charge potentials and fields for a given charge and current densities, which satisfy the continuity equation. The space-charge fields are computed using the time-dependent Green's function method. With these self-fields, we track the motions of the bunched beam in the rf photoinjector under the influence of external fields, such as rf and solenoid fields.

IRPSS constructs the charge and current densities of the beam using slices, i.e., zero thickness disks. In particular, the choice of $\rho(\mathbf{r})$ and $J_z(\mathbf{r})$ is of the form

$$\rho(\mathbf{r}) = \sum_{i=1}^N \sigma_i(r) \delta[z - z_i''(t)], \quad (4.1a)$$

and

$$J_z(\mathbf{r}) = \sum_{i=1}^N \sigma_i(r) \delta[z - z_i''(t)] \frac{dz_i''(t)}{dt}, \quad (4.1b)$$

where $\sigma_i(r)$ is the charge per unit area of the i th slice, $z_i''(t)$ is the longitudinal location of the i th slice, and N is the number of slices on the simulation. The required number of slices to form the bunch was described in the previous Chapter 3.

In order to illustrate this numerically, we use the ANL AWA 1.3 *GHz* gun parameters as listed in Table. 3.1. We make the simplifying assumption that the trajectories, $z_i''(t)$, are specified by the external rf field. Physically, one could view this simulation as the space-charge fields being small compared to the rf fields. The trajectory of each of the slices can be computed from the relativistic equation of motion for the slice in the rf field [11].

$$\frac{dz''}{dt} = \frac{1}{m_e} P_z \quad (4.2a)$$

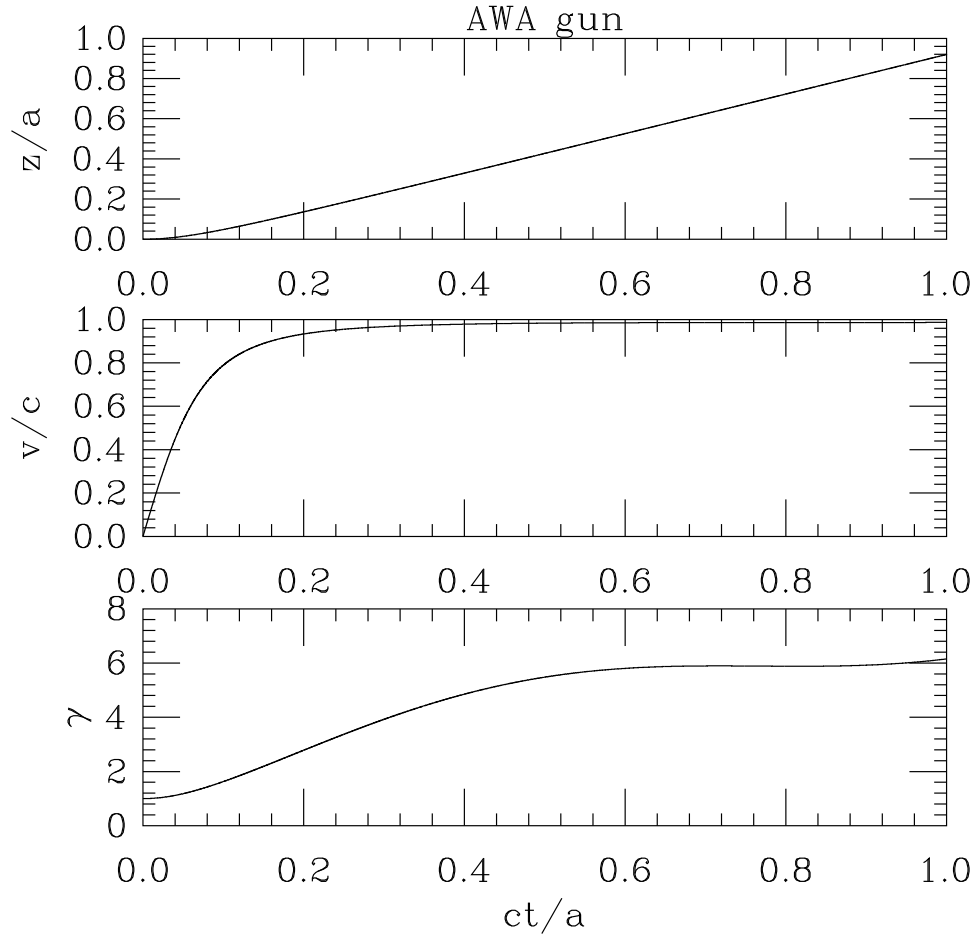


Figure 4.1: The trajectory, velocity, and acceleration of a particle in ANL AWA 1.3 GHz rf photoinjector are plotted as functions of $\tau = ct/a$ with the rf peak field of 77 MV/m .

and

$$\frac{dP_z}{dt} = -eE_z^{\text{rf}}(r, z, t), \quad (4.2b)$$

where m_e is the mass of an electron and $E_z^{\text{rf}}(r, z, t)$ is the external rf field. Figure 4.1 shows the trajectory, velocity, and Lorentz factor, γ , of a particle in the ANL AWA 1.3 *GHz* rf photoinjector. To calculate the trajectories, the TM_{01} mode rf field is used.

4.1.2 External Fields

In the rf photoinjector, the electron beam emitted from the cathode is accelerating by the external rf field. The rf field accelerates the beam from rest to a relativistic velocity. There are numerous codes for modeling the rf cavities and for computing the fields in those systems, such as SUPERFISH [33], or MWS (Micro Wave Studio) [47]. In our simulation, we calculate the rf fields using SUPERFISH, and the field data is easily imported into our simulation code, IRPSS. Figure 4.2 shows the external rf and solenoid fields which have been used in our beam dynamics simulation. Those fields are computed using parameters of the ANL AWA 1.3 *GHz* rf photoinjector, listed in Table 3.1. In the following numerical examples for the beam dynamics, we will use the rf field maps calculated using SUPERFISH.

In SUPERFISH, the rf system is assumed to be cylindrically symmetric. Fully 3-dimensional rf field maps with complicated geometries can be calculated with other simulation codes, e.g., MWS. In IRPSS, the external field maps are imported in 3-dimensional coordinates, hence we can use not only rf field maps of SUPERFISH, but also those of MWS. Since our goal is to see the zeroth order symmetric space-charge effect, the geometry of the rf gun is assumed to be the axially symmetric, and this is a good approximation.

Alternatively, one can use TM_{010} mode rf fields, which is mostly dominant through

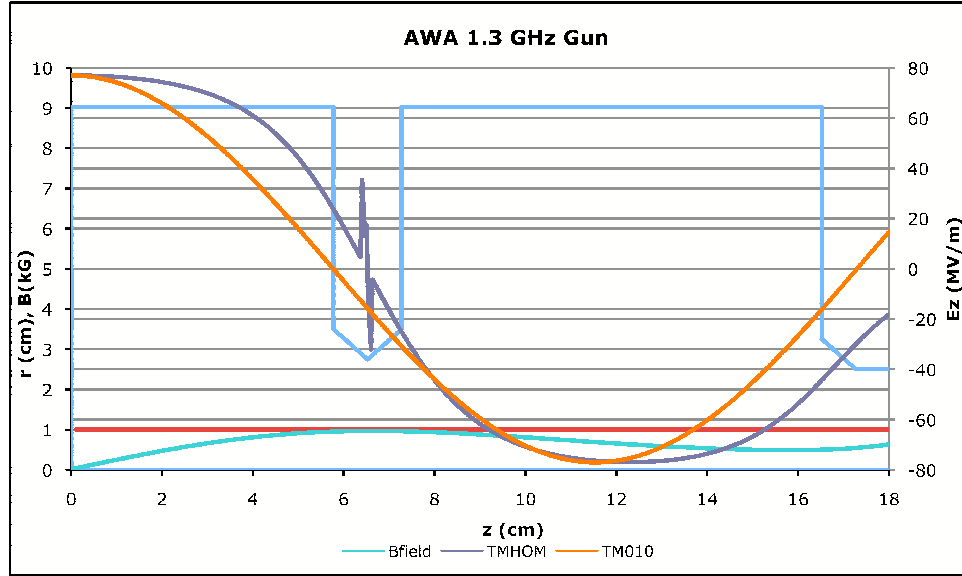


Figure 4.2: The external rf (dark blue) and solenoid (green) fields are plotted in the schematic diagram (light blue) of the ANL AWA 1.3 *GHz* rf photoinjector. For comparison, the rf fields (orange) calculated from SUPERFISH and those of TM_{010} mode are presented.

the entire rf gun. The advantage of TM_{010} mode rf fields is that the analytical forms are well known and ready to use. The TM_{010} mode electromagnetic rf fields in the pillbox cavity with sin convention are given by [6, 39]

$$\begin{aligned} E_z &= E_0 \cos(k_z z) \sin(\omega t + \varphi_0), \\ E_r &= \frac{E_0 r k_z}{2} \sin(k_z z) \sin(\omega t + \varphi_0), \\ B_\theta &= \frac{E_0 r k_z}{2c} \cos(k_z z) \cos(\omega t + \varphi_0), \end{aligned} \quad (4.3)$$

where E_0 is the peak rf field, k_z is the longitudinal wave number, ω is the angular rf frequency, and φ_0 is the injection rf phase. The vector and scalar potential can be found from the following three relations:

- (1) $\vec{E} = -\vec{\nabla}\Phi - \frac{\partial \vec{A}}{\partial t}$,
- (2) $\vec{B} = \vec{\nabla} \times \vec{A}$,
- (3) $\vec{\nabla} \cdot \vec{A} + \frac{1}{c^2} \frac{\partial \Phi}{\partial t} = 0$ (Lorentz gauge condition).

Then, the potentials are given by

$$\Phi = -\frac{E_0}{2k_z} \sin(k_z z) \sin(\omega t + \varphi_0), \quad (4.4a)$$

$$A_r = \frac{E_0 r}{2c} \sin(k_z z) \cos(\omega t + \varphi_0), \quad (4.4b)$$

$$A_z = \frac{E_0}{2k_z c} \cos(k_z z) \cos(\omega t + \varphi_0). \quad (4.4c)$$

The solenoid magnetic fields in IRPSS simulation are also imported from the external field maps. The magnetic fields can be computed using POISSON [33] or MAFIA [19]. Since our simulation is concentrated on the first half cell in the rf gun, and the solenoid magnetic field is relatively small as $< 1 \text{ kG}$, we do not show its details.

4.1.3 Equations of Motion

After the full calculations of electromagnetic space-charge fields in the first part of IRPSS, the second part in IRPSS code tracks the motion of the electron beam with space-charge and external fields. One may simulate the beam dynamics using either the Hamiltonian of the system or the Lorentz force law. The Hamiltonian of an electron in the cylindrical coordinates is given by

$$H = e\phi + c \left[m_e^2 c^2 + (P_r - eA_r)^2 + \left(\frac{P_\theta}{r} - eA_\theta \right)^2 + (P_z - eA_z)^2 \right]^{1/2}. \quad (4.5)$$

In IRPSS, we prefer to use the Lorentz force law,

$$\mathbf{F} = q [\mathbf{E} + (\beta \times c\mathbf{B})], \quad (4.6)$$

since this method does not require additional derivatives of potential maps. In the cylindrically symmetric system, we have only the following field components.

- (1) Space-Charge fields: E_r^{SC} , E_z^{SC} , and B_θ^{SC} ,
- (2) Rf fields: E_r^{RF} , E_z^{RF} , and B_θ^{RF} ,
- (3) Solenoid fields: B_r^{SC} and B_z^{SC} .

The 2nd order differential equations in the Lorentz force law with these fields are numerically simulated using the 4th order Runge-Kutta method [36], Runge-Kutta methods have the high-order local truncation error of the Taylor methods while eliminating the need to compute and evaluate the derivatives of $f(\mathbf{r}, t)$. To achieve highly accurate results, CERNlib is implemented using the Runge-Kutta method [48].

4.2 Space-Charge Fields and Beam Dynamics

4.2.1 Calculations of Space-Charge Fields

In most of rf simulation codes, such as, PARMELA, the space-charge fields are calculated electrostatically. However, IRPSS uses a fully electromagnetic method for the space-charge field calculations. The differences in field calculations can cause differences in the beam dynamics. In this section, we first show the physics of space-charge fields near the cathode, and compare the electromagnetic and electrostatic space-charge fields.

In order to compare the space-charge fields of IRPSS with electrostatic codes, we simplify the photoinjector system by assuming that it has no iris and the cavity is cylindrically symmetric. Since the iris does not have much of an effect on the beam dynamics for early times, this assumption is an excellent approximation, while we investigate the physics near the cathode.

The rf field for the beam accelerating in the gun is calculated using SUPERFISH [33], and the peak rf E_z field is 50 MV/m with the injection phase of 65 degrees. The azimuthal rf magnetic field B_θ is also included in the simulation. Here, only rf fields are used for the external field in order to focus on the effect of the space-charge fields. The external solenoidal fields, which are normally used for emittance compensation [12], are very small near the cathode and are excluded.

We use a radial parabolic shape for the transverse beam distribution and a uniform longitudinal distribution for these simulations:

$$\rho(r, z, t) = \sum_i^N \frac{2Q}{\pi r_b^2} \Theta(r_b - r) \left(1 - \frac{r^2}{r_b^2}\right) \delta[z - z_i''(t)] \quad (4.7)$$

where Q is the bunch charge, r_b is the beam radius (1 mm). For the uniform longitudinal beam distribution, a multi-slice method is used. In particular, a bunched beam

is broken up into a number of zero-thickness slices. In Eq. (4.7), the $z_i''(t)$ indicates the location of the i th slice with respect to time. We assume that each beam slice has an equal amount of charge. To reduce the computational time and errors and to achieve accurate calculations of space-charge fields, an adequate number of zero thickness slices are uniformly distributed within the desired bunch length. In the space-charge field calculation, we choose a bunch length of 1.2 ps . For this bunch length, 41 longitudinal slices are enough to smoothly model the space-charge fields. In Chapter 3, we showed the computational requirements for IRPSS, such as the minimum eigenmode numbers and the minimum numerical integration time step for achieving highly accurate space-charge field calculations.

In IRPSS, the electromagnetic space-charge fields are solved from Maxwell's equations for conductor boundary conditions. These solutions can be obtained using a time-dependent Green's function method. For cylindrically symmetric pipe boundary conditions with a flat cathode, all fields can be computed analytically and are given by,

$$E_r(r, z, t) = \frac{4Q}{\pi\epsilon_0\hat{r}_b^2a^2} \sum_{n=0}^{\infty} \frac{J_1(j_{0n}\hat{r})}{j_{0n}|J_1(j_{0n})|^2} \left[\frac{2}{j_{0n}\hat{r}_b} J_1(j_{0n}\hat{r}_b) - J_0(j_{0n}\hat{r}_b) \right] \times \int_{-\infty}^{\tau} d\tau' \left[J_0(j_{0n}\hat{\lambda}_-) \Theta(\hat{\lambda}_-^2) - J_0(j_{0n}\hat{\lambda}_+) \Theta(\hat{\lambda}_+^2) \right] \quad (4.8a)$$

$$B_{\theta}(r, z, t) = \frac{4cQ\mu_0}{\pi\hat{r}_b^2a^2} \sum_{n=0}^{\infty} \frac{J_1(j_{0n}\hat{r})}{j_{0n}|J_1(j_{0n})|^2} \left[\frac{2}{j_{0n}\hat{r}_b} J_1(j_{0n}\hat{r}_b) - J_0(j_{0n}\hat{r}_b) \right] \times \int_{-\infty}^{\tau} d\tau' \left[J_0(j_{0n}\hat{\lambda}_-) \Theta(\hat{\lambda}_-^2) + J_0(j_{0n}\hat{\lambda}_+) \Theta(\hat{\lambda}_+^2) \right] \left[\frac{dz''(\tau)}{d\tau} \right]_{\tau=\tau'} \quad (4.8b)$$

and

$$\begin{aligned}
E_z = & \frac{4Q}{\pi\epsilon_0\hat{r}_b^2a^2} \sum_{n=0}^{\infty} \frac{J_0(j_{0n}\hat{r})}{j_{0n}^2|J_1(j_{0n})|^2} \left[\frac{2}{j_{0n}\hat{r}_b} J_1(j_{0n}\hat{r}_b) - J_0(j_{0n}\hat{r}_b) \right] \\
& \times \int_{-\infty}^{\tau} d\tau' \left\{ \left\{ [\hat{z} - \hat{z}''(\tau')] - (\tau - \tau') \left[\frac{d\hat{z}''(\tau)}{d\tau} \right]_{\tau=\tau'} \right\} \right. \\
& \times \left[-\frac{j_{0n}}{\hat{\lambda}_-} J_1(j_{0n}\hat{\lambda}_-) \Theta(\hat{\lambda}_-^2) + 2a^2 J_0(j_{0n}\hat{\lambda}_-) \delta(\hat{\lambda}_-^2) \right] \\
& - \left\{ [\hat{z} + \hat{z}''(\tau')] + (\tau - \tau') \left[\frac{d\hat{z}''(\tau)}{d\tau} \right]_{\tau=\tau'} \right\} \\
& \times \left[-\frac{j_{0n}}{\hat{\lambda}_+} J_1(j_{0n}\hat{\lambda}_+) \Theta(\hat{\lambda}_+^2) + 2a^2 J_0(j_{0n}\hat{\lambda}_+) \delta(\hat{\lambda}_+^2) \right] \Bigg\}, \tag{4.8c}
\end{aligned}$$

where $\hat{r}_b = r_b/a$, $\hat{r} = r/a$, $\hat{z} = z/a$, $\tau = ct/a$, $\tau' = ct'/a$, and $\hat{\lambda}_{\pm}^2 = (\tau - \tau')^2 - (\hat{z} \pm \hat{z}')^2$

For the cylindrical cavity, ψ_{mn} are the transverse eigenfunctions. In general, spatial and time integrations can be performed numerically. However, in this simulation, we specify ρ in Eqn. (4.7) for the transverse direction, and use zero thickness slices longitudinally to model the beam.

In addition to IRPSS, we have also written an electrostatic code using a time-independent Green's function approach. The electrostatic space-charge potential of the real disk beam in the rest frame for a cylindrically symmetric waveguide with a flat cathode can be calculated as [34]:

$$\phi(\mathbf{r}) = \frac{1}{\epsilon_0} \int G_{\phi}(\mathbf{r}; \mathbf{r}') \rho(\mathbf{r}') d\mathbf{r}', \tag{4.9}$$

where

$$G_{\phi}(\mathbf{r}; \mathbf{r}') = \frac{1}{2} \sum_{mn} \frac{\psi_{mn}(\mathbf{r}_{\perp}) \psi_{mn}^*(\mathbf{r}'_{\perp})}{k_{\perp mn}} e^{-\frac{j_{0n}}{a}|z-z_0|}, \tag{4.10}$$

and a is the cavity radius (9.08 cm). In order to include the image charge effect, the scalar potential can be described as the superposition of potentials of real and image disks. Since the beam is at rest in this frame, the vector potential, A_z is zero.

The scalar and vector potentials in the laboratory frame can be obtained by Lorentz transformations, and these yield the electrostatic space-charge fields:

$$E_r^{\text{ES}} = \frac{4Q\gamma}{\pi\epsilon_0 r_b^2} \sum_n \frac{J_1(j_{0n}r/a)}{j_{0n}^2 |J_1(j_{0n})|^2} \left[\frac{2}{j_{0n} \frac{r_b}{a}} J_1\left(j_{0n} \frac{r_b}{a}\right) - J_0\left(j_{0n} \frac{r_b}{a}\right) \right] \times \left\{ e^{-\frac{j_{0n}}{a}\gamma|z-z_0|} - e^{-\frac{j_{0n}}{a}\gamma|z+z_0|} \right\}, \quad (4.11a)$$

$$B_\theta^{\text{ES}} = \frac{4cQ\mu_0\beta\gamma}{\pi r_b^2} \sum_n \frac{J_1(j_{0n}r/a)}{j_{0n}^2 |J_1(j_{0n})|^2} \left[\frac{2}{j_{0n} \frac{r_b}{a}} J_1\left(j_{0n} \frac{r_b}{a}\right) - J_0\left(j_{0n} \frac{r_b}{a}\right) \right] \times \left\{ e^{-\frac{j_{0n}}{a}\gamma|z-z_0|} + e^{-\frac{j_{0n}}{a}\gamma|z+z_0|} \right\}, \quad (4.11b)$$

$$E_z^{\text{ES}} = \frac{4Q}{\pi\epsilon_0 r_b^2} \sum_n \frac{J_0(j_{0n}r/a)}{j_{0n}^2 |J_1(j_{0n})|^2} \left[\frac{2}{j_{0n} \frac{r_b}{a}} J_1\left(j_{0n} \frac{r_b}{a}\right) - J_0\left(j_{0n} \frac{r_b}{a}\right) \right] \times \begin{cases} \left[e^{-\frac{j_{0n}}{a}\gamma|z-z_0|} - e^{-\frac{j_{0n}}{a}\gamma|z+z_0|} \right] & \text{for } z \geq 0, \\ \left[-e^{-\frac{j_{0n}}{a}\gamma|z_0-z|} - e^{-\frac{j_{0n}}{a}\gamma|z+z_0|} \right] & \text{for } z < 0, \end{cases} \quad (4.11c)$$

where z_0 is the location of a disk beam. The detailed derivation of Eqn (4.11) is in Appendix B.

In order to check the validity of the electrostatic code, we also formulated an exact bunch charge and current density fluid model assuming zero current density compressibility, which represents the physics at beam emission. We have found that both the electrostatic fluid model and the electrostatic code agree precisely. One of the advantages of developing the analytical fluid model is that we can produce an exact formula for the longitudinal space-charge field at the critical location $r = 0.0$ m and $z = 0.0$ m. This formula is given by,

$$E_z^{\text{ES}}(0,0) = \frac{4Q}{\pi\epsilon_0 r_b^2} \sum_m \sqrt{\frac{\pi}{j_{0m} z_b/a}} \frac{\text{Erf}\left(\sqrt{j_{0m} z_b/a}\right)}{j_{0m}^2 J_1^2(j_{0m})} \times \left[\frac{2}{j_{0m} r_b/a} J_1\left(j_{0m} \frac{r_b}{a}\right) - J_0\left(j_{0m} \frac{r_b}{a}\right) \right], \quad (4.12)$$

where Erf is the error function, and r_b and z_b are the bunch radius and bunch length, respectively. The detailed derivation of Eqn (4.12) is in Appendix B.2. When we

compare the two longitudinal electrostatic fields at $r = 0$ and $z = 0$, which is the center of the cathode, as the full bunch is emitted, they agree extremely well.

Figure 4.3 shows the critical E_z space-charge fields at $r = 0.0$ and $z = 0.0$ for different laser pulse lengths at 0.1 nC (for $r_b = 1 \text{ mm}$) and 10 nC (for $r_b = 1 \text{ cm}$). The primary result is that as the laser pulse length is increased, the discrepancy between electrostatic and electromagnetic space-charge fields is gradually increased. The size of the discrepancy also depends on the beam radius. Qualitatively, as the beam radius is increased, i.e., the beam becomes more pancake like, and the discrepancy becomes smaller. Moreover, the maximum electric field for both the electrostatic, as well as the electromagnetic cases, occurs when they have a zero bunch length beam, which acts as a sheet of charge near the cathode. In this case, the electric field is exactly found to be σ/ϵ_0 where σ is the local charge density (charge/area) on the beam axis. For a parabolic (radial) and uniform (longitudinal) beam with $Q = 100 \text{ pC}$, σ is given by $2Q/\pi\epsilon_0 r_b^2$, hence $\sigma/\epsilon_0 = -7.19 \text{ MV/m}$. Both electromagnetic and electrostatic results show that they agree extremely well for shorter bunch lengths, i.e., pancake-like beam, as seen in Figure 4.3(b).

Figure 4.4 shows the percentage difference between electromagnetic and electrostatic critical E_z fields. And this effect can become larger by increasing the bunch length with fixed beam radius. However, the percentage discrepancy between electromagnetic and electrostatic fields has a maximum around 2.4% for $r_b = 1 \text{ mm}$ with a laser pulse length of 10 psec and around 1.6% discrepancy for $r_b = 1 \text{ cm}$.

In Figures 4.5 and 4.6, we compare electromagnetic and electrostatic space-charge fields for a 1 nC bunched beam. The space-charge fields, \mathbf{F}/Q , are computed from the Lorentz force law, $\mathbf{F} = Q [\mathbf{E} + \beta \times (c\mathbf{B})]$, where \mathbf{E} and \mathbf{B} are proportional to the bunch charge Q . Figure 4.5 shows F_r/Q vs. r , for various times. At $t = 0.005a/c$, a bunch is just launched, and there are significant discrepancies between the two space-charge fields. For a large amount of beam charge, such as 1 nC , the beam feels

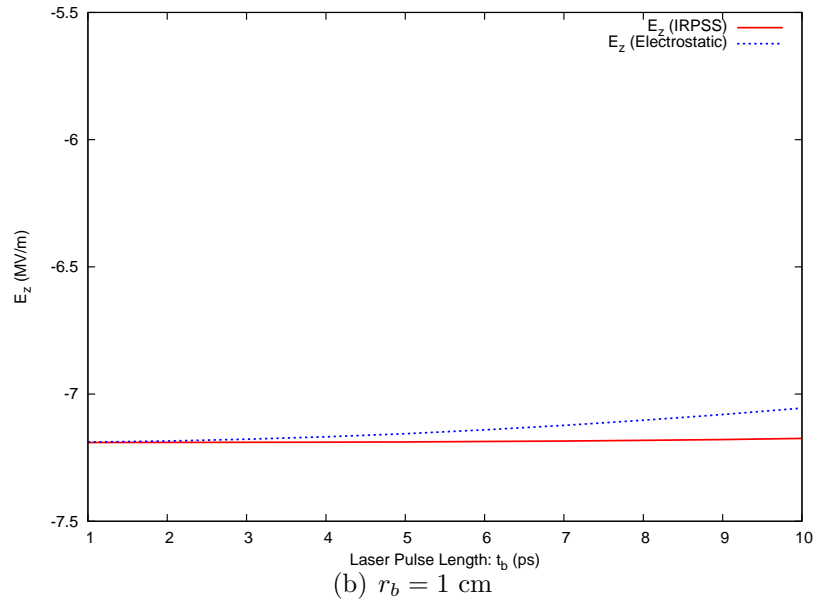
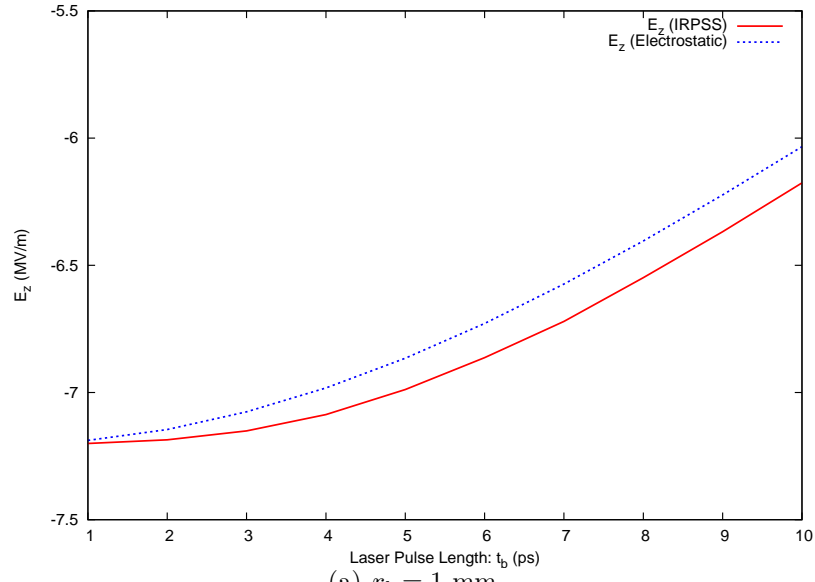


Figure 4.3: The longitudinal space-charge fields at $r = 0.0$ and $z = 0.0$ computed by IRPSS (red) and electrostatic methods (blue)

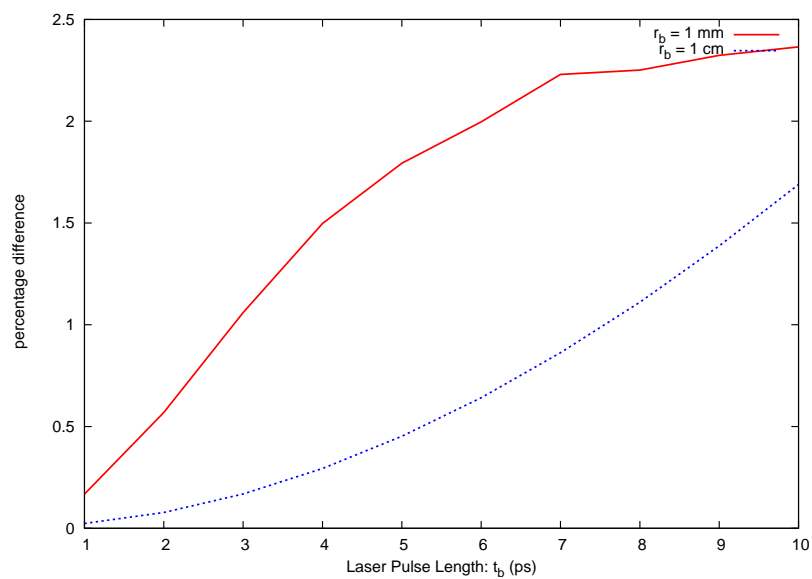


Figure 4.4: Percentage difference between critical electromagnetic and electrostatic E_z space-charge fields for different beam radii

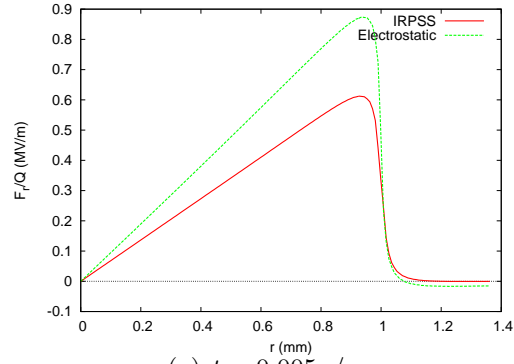
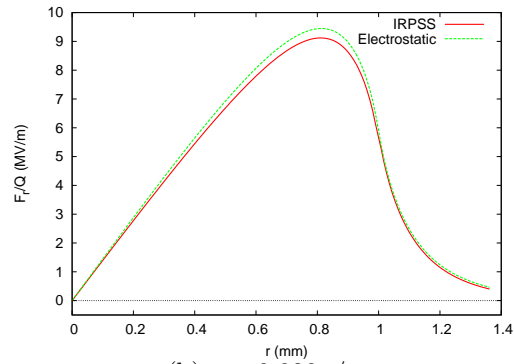
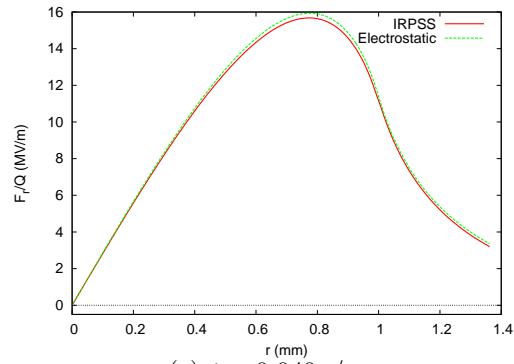
(a) $t = 0.005a/c$ (b) $t = 0.020a/c$ (c) $t = 0.040a/c$

Figure 4.5: Electromagnetic (IRPSS) and electrostatic space-charge fields for different times: F_r/Q vs. r at the center of the beam

more of a defocusing force with the electrostatic space-charge fields in the transverse direction. Hence, this effect causes a growth in beam phase space. These discrepancies in space-charge fields between the two algorithms become smaller with time. For a small amount of beam charge, it becomes more difficult to find the difference between two fields, since the transverse space-charge fields are much smaller compared to the transverse rf fields.

Comparisons of the longitudinal space-charge fields are shown in Figure 4.6. As can be seen, the electromagnetic E_z space-charge field has a more negative value than the electrostatic E_z space-charge field near the cathode right after beam emission. However, the discrepancy, between electrostatic and electromagnetic space-charge fields in the longitudinal direction, for our example, is less pronounced than in the radial direction, because of the choice of short bunch length, i.e., 1.2 *psec*. The longitudinal discrepancy becomes more apparent for longer bunch lengths such as in the study by A. Candel *et al* which looked at a 10 and 15 *psec* bunch length cases [23]. Like the transverse space-charge fields, however, the longitudinal space-charge fields agree for higher time.

We could roughly estimate these discrepancies by assuming the beam as a thin disk. Since the initial bunch length of 1.2 *psec* is relatively smaller than the beam radius of $r_b = 1$ *mm*, the thin disk assumption is valid. For sufficiently small times, i.e., $t \ll r_b/c$, the edge effects of the beam for the electromagnetic space-charge fields at $r = 0$ and $z = 0$ is zero due to the finite speed of light. Hence, the longitudinal space-charge fields near the cathode at $r = 0$ resemble those of an infinite sheet of charge at $z''(t)$ with charge density σ_0 and an infinite sheet of image charge at $-z''(t)$ with charge density $-\sigma_0$. In this case, $\sigma_0 = 2Q/\pi r_b^2$ which is the charge density at $r = 0$ for a parabolic radial beam distribution. Therefore, for short times, the electromagnetic longitudinal field is σ_0/ϵ_0 . In the electrostatic case, however, the effects of the beam edges are non-negligible and give a reduction to E_z as shown in

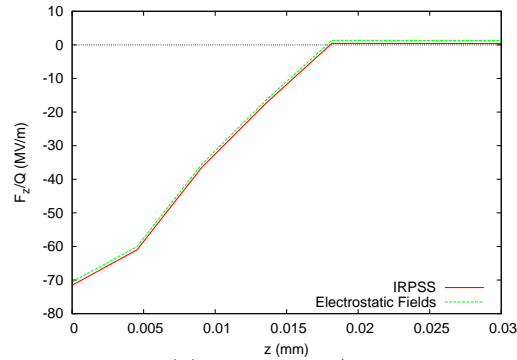
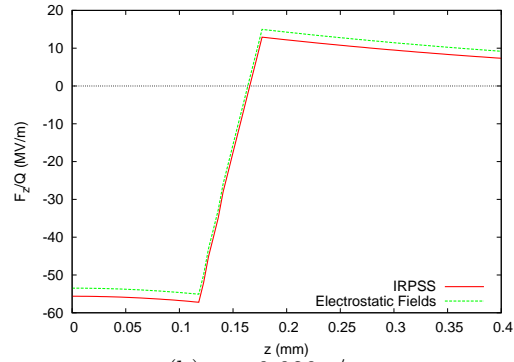
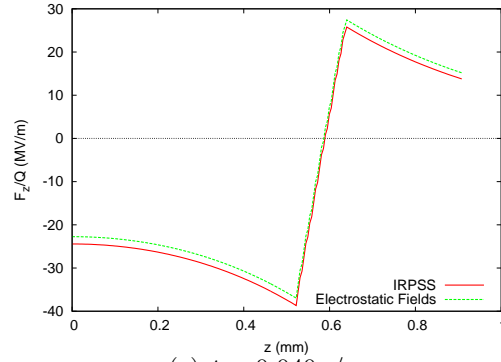
(a) $t = 0.005a/c$ (b) $t = 0.020a/c$ (c) $t = 0.040a/c$

Figure 4.6: The longitudinal electromagnetic (IRPSS) and electrostatic space-charge fields for different times: F_z/Q vs. z at $r = 0.0$

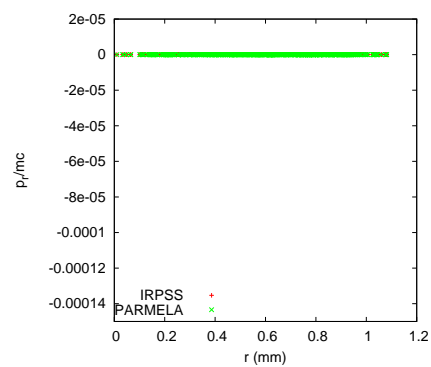
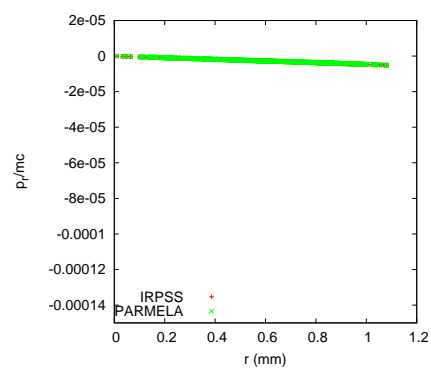
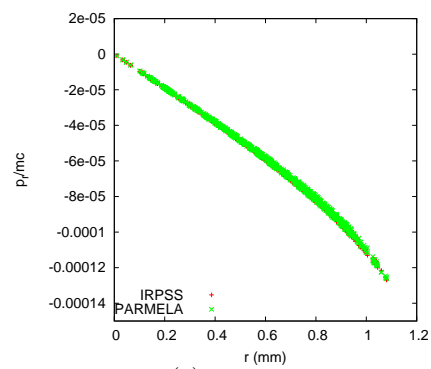
Figure 4.6, near the head and tail of the bunch.

4.2.2 Beam Dynamics with Space-Charge Effects

In the previous section, we showed the calculations of the time-dependent and time-independent space-charge fields (forces), and explained the differences between IRPSS and the electrostatic calculations. Now, we examine the beam dynamics near the cathode, where the space-charge effects are extremely important. As we have seen in the previous section, the electromagnetic and electrostatic space-charge fields have disagreements near the cathode, and these are getting smaller with time. In Figures 4.7-4.9, different locations ($z = 0.0$ cm (cathode), $z = 0.003$ cm, and $z = 0.03$ cm), all within the first cell and near the cathode, are chosen to see differences of the transverse phasespaces (p_r/mc vs. r/a) between two space-charge field calculations.

In order to check the validity of our tracking algorithm, we first run the simulations only with rf fields (zero space-charge fields). We compare these beam dynamics results with those of PARMELA, which are also run without the space-charge fields. At the cathode, the beam starts with zero momentum, i.e., zero thermal emittance. Hence, particles are on the r axis on the transverse phasespace plots. With only rf fields, particles are radially focused near the cathode. Figure 4.7 shows that the two codes agree very well.

For sufficiently large amounts of charge, the evolutions of the phasespace are very different. In Figures 4.8 and 4.9, we include the effects of space-charge. Since the initial beam distribution in the radial direction is parabolic, the radial space-charge forces are maximum at slightly less than $r = r_b$, as seen in Fig 4.5. Therefore, the radial beam edge feels less defocusing force than the particles with the maximum space-charge force. In phasespace plots, we could see these effects in both IRPSS and the Green's function based electrostatic code.

(a) $z = 0.0$ cm(b) $z = 0.003$ cm(c) $z = 0.03$ cm**Figure 4.7:** Phasespace plots with zero space-charge field

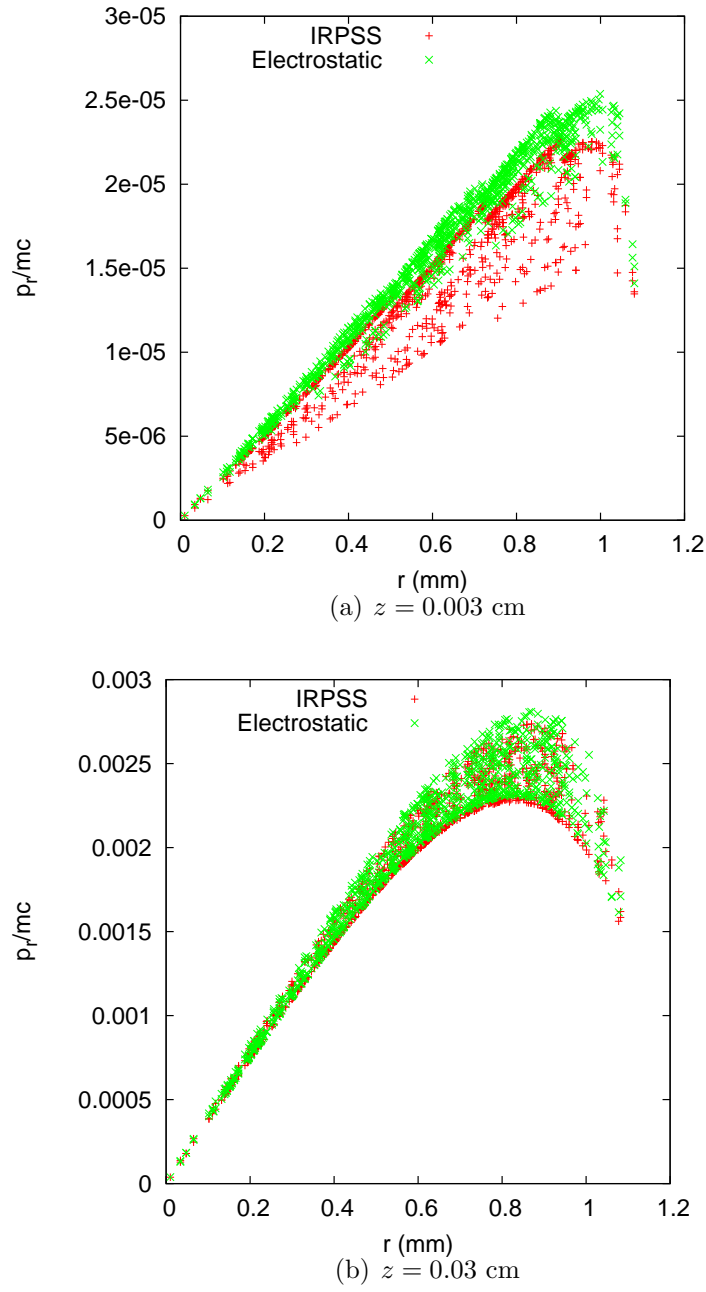


Figure 4.8: Phasespace plots for $Q = 100$ pC

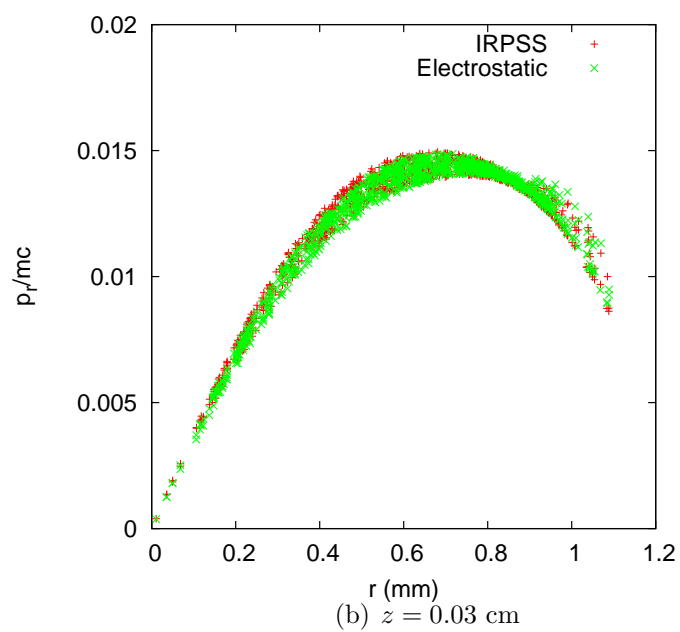
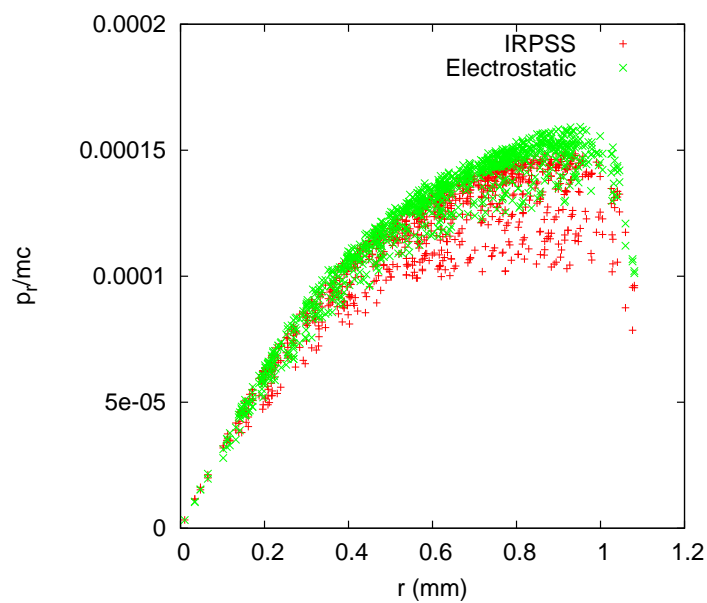


Figure 4.9: Phasespace plots for $Q = 500$ pC

As we increase the bunch charge, the differences between transverse phasespace plots become apparent at 1 pC , and then become more significant for larger bunch charges. Since the electrostatic space-charge fields near the cathode are larger than the electromagnetic space-charge fields, we see less defocusing in IRPSS phasespace plots. As seen in Figures 4.8(a), and 4.9(a), IRPSS and the electrostatic phasespace plots have large discrepancies, since particles with electrostatic fields feel much stronger defocusing forces. In general, we find a larger phasespace size in IRPSS simulations near the cathode compared to electrostatic simulations due to the larger variation of F_r in IRPSS with respect to time. Since the two transverse space-charge fields are getting closer with time as shown in Figure 4.5, phasespace plots for both electromagnetic (IRPSS) and electrostatic space-charge fields look similar at later times as shown in Figures 4.8(b), and 4.9(b).

For a highly charged beam, the longitudinal space-charge forces from the head of the bunch cause the tail of the bunch to hit back onto the cathode causing beam loss. There is no beam loss for lower beam charge, e.g. less than 100 pC , since the accelerating E_z^{rf} fields are dominant. Beam loss starts to occur at 640 pC , where the space-charge fields match the rf fields. From Figures 4.6, we can estimate that beam loss will occur at a slightly smaller beam charge value for the electromagnetic case since the electromagnetic E_z space-charge field at a bunch tail is slightly larger in magnitude than the electrostatic E_z space-charge field. For example, for 1 nC beam at $r_b = 1\text{ mm}$ and a bunch length of 1.2 psec , IRPSS expects about 32.6% beam loss, while the electrostatic code yields 32.4% beam loss. These small discrepancies are also found in longitudinal energy spread comparisons which show differences of less than 1%.

Figure 4.10 shows comparisons of transverse emittances between IRPSS and electrostatic calculations with different bunch charges. For lower beam charge, such as 1 pC , rf forces are dominant and space-charge forces are relatively small, so that

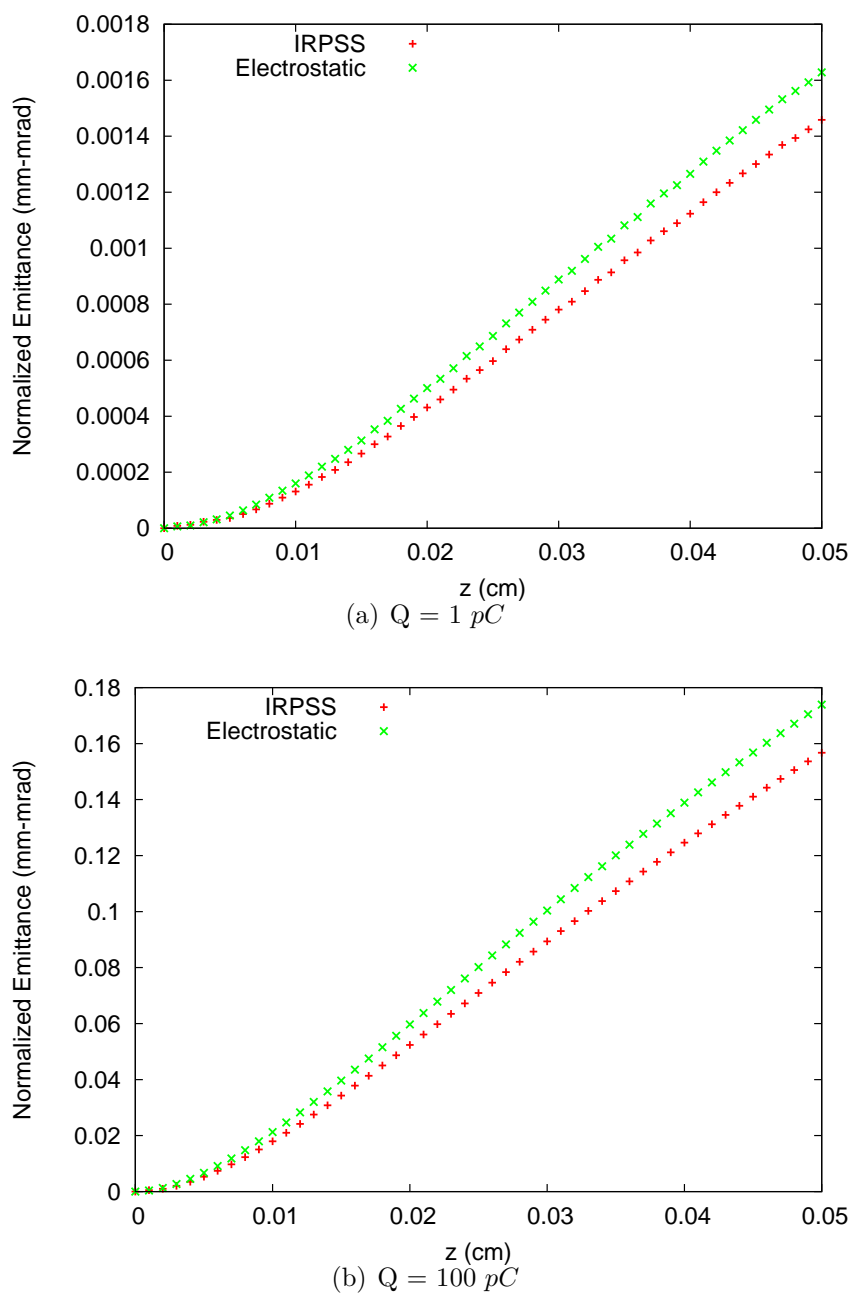


Figure 4.10: Normalized rms transverse emittances

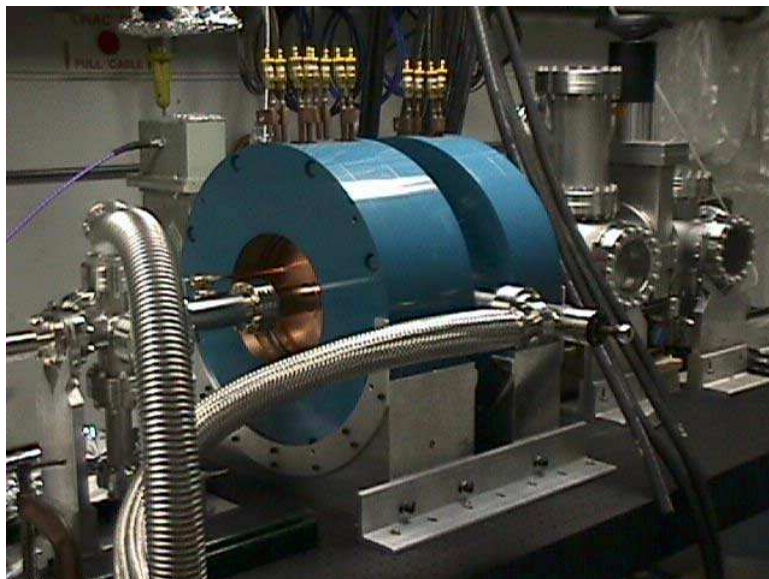
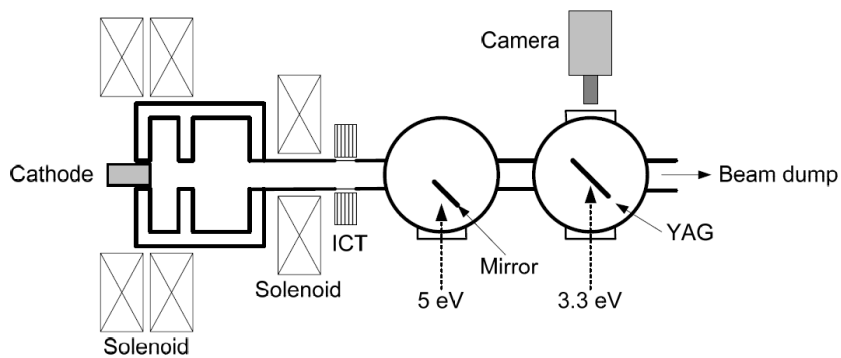
emittances are small as shown in Figure 4.10(a). For $Q = 100 \text{ pC}$, however, the beam feels much stronger space-charge forces, hence, this causes larger emittance than lower beam charge as shown in Figure 4.10(b). The discrepancies in space-charge forces leads to a difference in emittances, which is about $8 \sim 9\%$ at $z = 0.05 \text{ cm}$.

4.3 Experimental Measurements

We performed an experimental beam loss measurement on the 1.3 GHz rf gun at the ANL AWA experiment [45]. The main purpose of the Argonne Wakefield Accelerator is for high current beam generation and diagnostics, and high-gradient wakefield experiments [27, 49]. Figure 4.11(a) shows the AWA rf photoinjector and the schematic diagram of its beamline. It consists of a 1.5 cell rf cavity, CS_2Te semiconductor photocathode, YAG laser, solenoid magnets, and beam diagnostic systems. The gun is operated with 50 MV/m rf peak field, 65 degree injection phase.

Before guiding the laser light to the cathode, we measure the laser spot size and intensity using *UV* (Ultra-Violet) camera. Although the efficiency of the photocathode is not 100 % in generating the electron beam, we assume that the laser intensity is equivalent to the initial beam charge. Experimentally, it is difficult to measure the beam charge at the inside of the gun. Hence, we measure the emitted beam charge by taking the beam intensity and its profile through the 2nd diagnostic window after the gun. In order to see the effect of the bunch length in the beam loss measurement, we choose two laser pulse lengths, 3.4 and 10.4 *psec* in FWHM (Full-Width Half-Maximum). The laser pulse length is equivalent to the bunch length. The laser spot size is 2 *mm*, i.e., the beam radius is 1 *mm*.

Figure 4.12 shows plots of the measured bunch charge from the exit of the gun as a function of laser pulse intensity. If no beam loss were to occur, then the plot should be linear with a uniform slope. However, at a critical bunch charge, i.e.,

(a) ANL AWA 1.3 GHz rf photoinjector

(b) Schematic diagram of Argonne Wakefield Accelerator beamline [49]

Figure 4.11: Experimental set up for beam loss measurements

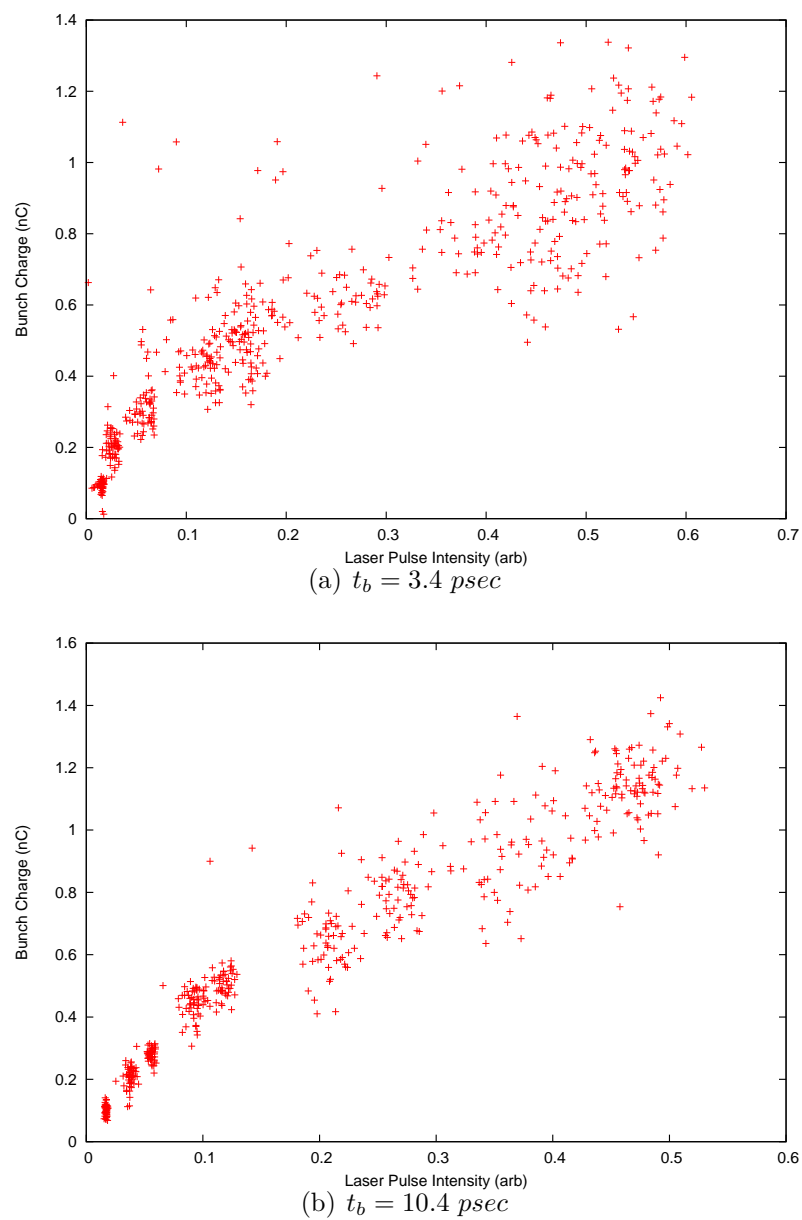


Figure 4.12: Experimental results of bunch charge vs. laser pulse intensity for different bunch lengths.

$E_z^{\text{rf}} = E_z^{\text{critical}}$, for fixed laser pulse length and radius, one would expect beam loss to occur and a reduction in the slope of the curve. The visual inspection of the preliminary data suggest changes in slopes, i.e., onsets of beam losses, at around $300 - 400 \text{ pC}$ for 3.4 psec and $500 - 600 \text{ pC}$ for 10.4 psec . However, these are lower than our theoretical predictions of 1.2 nC for a uniform radial bunch distribution. Possible explanations for these are non-uniformity of the laser spot size, effects due to the acceptance in the first-half cell, and uncertainties in measurements of laser intensities and bunch charges. Further analysis is needed to understand differences between prediction and experiment. We plan to continue these measurements, and look at possible ways to increase the E_z field discrepancy by changing the magnitude of the rf field and injection phase.

4.4 Discussion

IRPSS is a novel space-charge solver and simulation code for modeling photoinjectors. Since it uses a Green's function approach to calculate electromagnetic space-charge fields, it is capable of simulating beams with arbitrarily small bunch lengths. Because IRPSS self-consistently models the space-charge fields electromagnetically, effects such as a finite time-retardation can be included. In general, electrostatic codes, such as PARMELA may overestimate the transverse space-charge fields and underestimate the longitudinal space-charge fields compared to IRPSS leading to differences in beam phasespace near the cathode and beam loss.

We present the space-charge effects in the ANL AWA rf photocathode gun near the cathode by comparing the phasespace and emittance between IRPSS and an electrostatic Green's function code. In general, we have found that the phasespace plots and emittances predicted by IRPSS and the electrostatic code can be different due to the space-charge fields.

Chapter 5

Transverse Current Modeling

We generalize the exact formalism for the space-charge fields of a cylindrically symmetric beam in a conducting circular pipe. This formalism also includes the effect of the transverse currents, which was ignored for modeling the rf photoinjector in the previous chapters. With the series expansions of the charge and current densities in terms of the Bessel functions, the electromagnetic space-charge fields are constructed using the time-dependent Green's function method in the cylindrical conducting boundary system. This formalism can be used to model the high space-charge systems, such as high-power microwave sources. Numerical studies will be shown as an example of the space-charge field calculations for a radially oscillating beam.

5.1 Electromagnetic Field for Circularly Symmetric Sources

In this section, we derive the exact electromagnetic space-charge fields for circularly symmetric charged sources using a time-dependent Green's function method [50]. We assume that the system has a cylindrically symmetric conducting pipe with radius of

a. The charge and current densities are denoted by $\rho(r, z, t)$ and $\mathbf{J}(r, z, t)$ in cylindrical coordinates. These beam densities are only restricted by the self-consistent continuity equation, i.e., $\partial\rho/\partial t + \nabla \cdot \mathbf{J} = 0$.

5.1.1 Expansions of Charge and Current Densities

First, we start by making the judicious representations of the charge and current densities into series of Bessel functions. Since the beam source and the system are cylindrically symmetric, Bessel functions are helpful to find the solutions of wave equations, which define the electric and magnetic field components. By noting that for circularly symmetric beam distributions the radial and azimuthal current densities go to zero as $r \rightarrow 0$, the Bessel function expansions can be expressed as

$$\rho = \sum_{m=1}^{\infty} \rho_m(z, t) J_0 \left(\frac{j_{0m} r}{a} \right), \quad (5.1a)$$

$$J_r = \sum_{m=1}^{\infty} J_{rm}(z, t) J_1 \left(\frac{j_{0m} r}{a} \right), \quad (5.1b)$$

$$J_\theta = \sum_{m=1}^{\infty} J_{\theta m}(z, t) J_1 \left(\frac{j_{1m} r}{a} \right), \quad (5.1c)$$

and

$$J_z = \sum_{m=1}^{\infty} J_{zm}(z, t) J_0 \left(\frac{j_{0m} r}{a} \right), \quad (5.1d)$$

where $J_l(x)$ is the l^{th} order Bessel functions of the first kind and j_{lm} is the m^{th} zero of $J_l(x)$. We note that while three of the above source functions utilize j_{lm} in connection with $J_l(x)$ as Fourier-Bessel series expansions, the radial current density, J_r , does not. In particular, J_r utilizes j_{0m} zeroes in combination with $J_1(x)$, which is a special type of expansion known as a Dini series [51].

The coefficients in each expansion, which are functions of z and t , can be immediately found using orthogonality relations of the Bessel functions and are given

by

$$\rho_m = \frac{2}{a^2 J_1^2(j_{0m})} \int_0^a dr r \rho(r, z, t) J_0\left(\frac{j_{0m} r}{a}\right), \quad (5.2a)$$

$$J_{rm} = \frac{2}{a^2 J_1^2(j_{0m})} \int_0^a dr r J_r(r, z, t) J_1\left(\frac{j_{0m} r}{a}\right), \quad (5.2b)$$

$$J_{\theta m} = \frac{2}{a^2 J_0^2(j_{1m})} \int_0^a dr r J_\theta(r, z, t) J_1\left(\frac{j_{1m} r}{a}\right), \quad (5.2c)$$

and

$$J_{zm} = \frac{2}{a^2 J_1^2(j_{0m})} \int_0^a dr r J_z(r, z, t) J_0\left(\frac{j_{0m} r}{a}\right). \quad (5.2d)$$

Since $J_{\theta m}$ is independent of θ coordinates, the continuity equation can be represented in terms of ρ_m , J_{rm} , and J_{zm} , i.e

$$\frac{\partial \rho_m}{\partial t} = \frac{j_{0m}}{a} J_{rm} + \frac{\partial J_{zm}}{\partial z} = 0. \quad (5.3)$$

In addition, Maxwell's equations leads to inhomogeneous wave equations for the electromagnetic fields with charge and current densities acting as drive terms, i.e.,

$$\nabla^2 \mathbf{E} - \frac{1}{c^2} \frac{\partial^2 \mathbf{E}}{\partial t^2} = \frac{1}{\epsilon_0} \nabla \rho + \mu_0 \frac{\partial \mathbf{J}}{\partial t}, \quad (5.4a)$$

and

$$\nabla^2 \mathbf{B} - \frac{1}{c^2} \frac{\partial^2 \mathbf{B}}{\partial t^2} = -\mu_0 \nabla \times \mathbf{J}. \quad (5.4b)$$

From Eqn. (5.4), one can immediately find that under cylindrically symmetric conditions, J_θ will generate the fields E_θ , B_r , and B_z , while ρ , J_r , and J_z generate the other fields E_r , E_z , and B_θ .

5.1.2 TE Mode Space-Charge Fields

From Eqn. (5.4), the electric and magnetic fields generated by J_θ can be expressed in terms of Bessel functions with unknown coefficients. These coefficients, which

depend on z and t , can be found by solving wave equations with J_θ as a source. The expansions of TE-mode fields are given by

$$E_\theta = \sum_{m=1}^{\infty} E_{\theta m}(z, t) J_1 \left(\frac{j_{1m} r}{a} \right), \quad (5.5a)$$

$$B_r = \sum_{m=1}^{\infty} B_{rm}(z, t) J_1 \left(\frac{j_{1m} r}{a} \right), \quad (5.5b)$$

and

$$B_z = \sum_{m=1}^{\infty} B_{zm}(z, t) J_0 \left(\frac{j_{1m} r}{a} \right). \quad (5.5c)$$

At $r = a$, we note that E_θ and B_r equal to zero. Eqns. (5.5a) and (5.5b) imply that the series expansions of E_θ and B_r automatically satisfy the conducting boundary conditions, namely, $E_{||}|_{\text{surface}} = 0$ and $B_{\perp}|_{\text{surface}} = 0$. In addition, Eqn. (5.5c) gives another boundary condition, $\partial B_{||}/\partial r|_{\text{surface}} = 0$.

The coefficients in the field expansions are derived directly from Eqn. (5.4) and are given by,

$$\frac{\partial^2 E_{\theta m}}{\partial z^2} - \frac{1}{c^2} \frac{\partial^2 E_{\theta m}}{\partial t^2} - \left(\frac{j_{1m}}{a} \right)^2 E_{\theta m} = \mu_0 \frac{\partial J_{\theta m}}{\partial t}, \quad (5.6a)$$

$$\frac{\partial^2 B_{rm}}{\partial z^2} - \frac{1}{c^2} \frac{\partial^2 B_{rm}}{\partial t^2} - \left(\frac{j_{1m}}{a} \right)^2 B_{rm} = \mu_0 \frac{\partial J_{\theta m}}{\partial z}, \quad (5.6b)$$

and

$$\frac{\partial^2 B_{zm}}{\partial z^2} - \frac{1}{c^2} \frac{\partial^2 B_{zm}}{\partial t^2} - \left(\frac{j_{1m}}{a} \right)^2 B_{zm} = -\mu_0 \frac{j_{1m}}{a} J_{\theta m}. \quad (5.6c)$$

One can find the solutions of the Eqn. (5.6) using time-dependent Green's function method. This method was already discussed in detail for longitudinal currents in a conducting pipe in Chapter 3. In particular, the solutions to the field coefficients are given by,

$$E_{\theta m} = \int_{-\infty}^t dt' \int dz' \mu_0 \frac{\partial J_{\theta m}(z', t')}{\partial t'} G_{1m}(z, t; z', t') \quad (5.7a)$$

$$B_{rm} = \int_{-\infty}^t dt' \int dz' \mu_0 \frac{\partial J_{\theta m}(z', t')}{\partial t'} G_{1m}(z, t; z', t') \quad (5.7b)$$

and

$$B_{zm} = \int_{-\infty}^t dt' \int dz' \mu_0 \frac{j_{1m}}{a} J_{\theta m}(z', t') G_{1m}(z, t; z', t') \quad (5.7c)$$

where

$$G_{1m}(z, t; z', t') = \frac{c}{2} J_0 \left(\frac{j_{1m}}{a} \lambda \right) \Theta(\lambda^2) \quad (5.8a)$$

is a time-dependent Green's function that satisfies the differential equation

$$\frac{\partial^2 G_{1m}}{\partial z^2} - \frac{1}{c^2} \frac{\partial^2 G_{1m}}{\partial t^2} - \left(\frac{j_{1m}}{a} \right)^2 G_{1m} = -\delta(z - z') \delta(t - t'), \quad (5.8b)$$

and $\lambda = \sqrt{c^2(t - t')^2 - (z - z')^2}$.

Therefore, for a given $J_\theta(r, z, t)$, $J_{\theta m}(z, t)$ can be found by Eqn. (5.2c), and then coefficients $E_{\theta m}$, B_{rm} , and B_{zm} can be computed, finally the TE mode electromagnetic fields can be obtained.

5.1.3 TM Mode Space-Charge Fields

We now turn our attention to the TM mode fields, E_r , E_z , and B_θ . In a similar way, we can make series expansions for E_r , E_z , and B_θ , from Eqn. (5.1) and (5.4). i.e.,

$$E_r = \sum_{m=1}^{\infty} E_{rm}(z, t) J_1 \left(\frac{j_{0m} r}{a} \right), \quad (5.9a)$$

$$E_z = \sum_{m=1}^{\infty} E_{zm}(z, t) J_0 \left(\frac{j_{0m} r}{a} \right), \quad (5.9b)$$

and

$$B_\theta = \sum_{m=1}^{\infty} B_{\theta m}(z, t) J_1 \left(\frac{j_{0m} r}{a} \right). \quad (5.9c)$$

Again note that the field expansion for E_z correctly satisfies the conductor pipe boundary condition at $r = a$, namely, $E_{||}|_{\text{surface}} = 0$. These expansions when plugged

into the field wave equations, i.e., Eqns. (5.4a) and (5.4b), yield differential equations for the field coefficients given by:

$$\frac{\partial^2 E_{rm}}{\partial z^2} - \frac{1}{c^2} \frac{\partial^2 E_{rm}}{\partial t^2} - \left(\frac{j_{0m}}{a} \right)^2 E_{rm} = -\frac{j_{0m}}{a} \frac{\rho_m}{\epsilon_0} + \mu_0 \frac{\partial J_{rm}}{\partial t}, \quad (5.10a)$$

$$\frac{\partial^2 E_{zm}}{\partial z^2} - \frac{1}{c^2} \frac{\partial^2 E_{zm}}{\partial t^2} - \left(\frac{j_{0m}}{a} \right)^2 E_{zm} = \frac{1}{\epsilon_0} \frac{\partial \rho_m}{\partial z} + \mu_0 \frac{\partial J_{zm}}{\partial t}, \quad (5.10b)$$

and

$$\frac{\partial^2 B_{\theta m}}{\partial z^2} - \frac{1}{c^2} \frac{\partial^2 B_{\theta m}}{\partial t^2} - \left(\frac{j_{0m}}{a} \right)^2 B_{\theta m} = -\mu_0 \frac{j_{0m}}{a} J_{zm} - \mu_0 \frac{\partial J_{rm}}{\partial z}. \quad (5.10c)$$

In a similar fashion, we can construct E_r , E_z , and B_θ using a second time-dependent Green's function. In particular, the coefficients of the fields are given by,

$$E_{rm} = \int_{-\infty}^t dt' \int dz' \left(\frac{j_{0m}}{a} \frac{\rho_m}{\epsilon_0} - \mu_0 \frac{\partial J_{rm}}{\partial t'} \right) G_{0m}(z, t; z', t'), \quad (5.11a)$$

$$E_{zm} = - \int_{-\infty}^t dt' \int dz' \left(\frac{1}{\epsilon_0} \frac{\partial \rho_m}{\partial z'} + \mu_0 \frac{\partial J_{zm}}{\partial t'} \right) G_{0m}(z, t; z', t'), \quad (5.11b)$$

$$B_{\theta m} = \int_{-\infty}^t dt' \int dz' \left(\mu_0 \frac{j_{0m}}{a} J_{zm} + \mu_0 \frac{\partial J_{rm}}{\partial z'} \right) G_{0m}(z, t; z', t'). \quad (5.11c)$$

where

$$G_{0m}(z, t; z', t') = \frac{c}{2} J_0 \left(\frac{j_{0m}}{a} \lambda \right) \Theta(\lambda^2) \quad (5.12a)$$

is a time-dependent Green's function that satisfies the differential equation

$$\frac{\partial^2 G_{0m}}{\partial z^2} - \frac{1}{c^2} \frac{\partial^2 G_{0m}}{\partial t^2} - \left(\frac{j_{0m}}{a} \right)^2 G_{0m} = -\delta(z - z') \delta(t - t'). \quad (5.12b)$$

Finally, the solutions to the field coefficients in Eqns. (5.7) and (5.11) along with the expansion formulas in Eqns. (5.2), (5.5), and (5.9) offer a complete description

of electromagnetic space-charge fields for cylindrically symmetric beams in a circular conducting pipe.

We should note that for the expansions given in Eqns. (5.2), (5.5), and (5.9), there are other useful formulas connecting the field coefficients which can be immediately found from Maxwell's equations. In particular, one can easily verify the following relations,

$$B_{rm} = -\frac{a}{j_{1m}} \frac{\partial B_{zm}}{\partial z}, \quad (5.13a)$$

$$E_{\theta m} = -\frac{a}{j_{1m}} \frac{\partial B_{zm}}{\partial t}, \quad (5.13b)$$

$$\frac{j_{0m}}{a} E_{rm} + \frac{\partial E_{zm}}{\partial z} = \frac{1}{\epsilon_0} \rho_m, \quad (5.13c)$$

$$\frac{\partial E_{rm}}{\partial z} + \frac{j_{0m}}{a} E_{zm} = -\frac{\partial B_{\theta m}}{\partial t}, \quad (5.13d)$$

$$-\frac{\partial B_{\theta m}}{\partial z} = \mu_0 J_{rm} + \frac{1}{c^2} \frac{\partial E_{rm}}{\partial t}, \quad (5.13e)$$

and

$$\frac{j_{0m}}{a} B_{\theta m} = \mu_0 J_{zm} + \frac{1}{c^2} \frac{\partial E_{zm}}{\partial t}. \quad (5.13f)$$

One can immediately see that although all of the field coefficients will be determined from integrations of Green's functions over z' and t' for given charge and current densities in Eqns. (5.7) and (5.11), it is only necessary to compute these integrations for a few of the field coefficients. Hence, using relations in Eqns. (5.13), it is easy to determine the other coefficients. This will be demonstrated in the numerical example in the next Section.

5.2 Numerical Implementation

5.2.1 Description of the System

We now demonstrate how to numerically model the space-charge fields of a radially oscillating bunched beam in a circular pipe. We assume that the beam is parabolic in the transverse direction, and is oscillating in the radial direction. Specifically, the beam distribution is given by

$$\rho(r, z, t) = \frac{2Q}{\pi r_b^2(t)} \left[1 - \frac{r^2}{r_b^2(t)} \right] \Theta[r_b(t) - r] \left[\Theta\left(z + \frac{L}{2}\right) - \Theta\left(z - \frac{L}{2}\right) \right], \quad (5.14)$$

where Q is the total bunch charge, L is its longitudinal length. The beam radius, $r_b(t)$ is a constant, r_0 , for time $t < 0$, and then is sinusoidally oscillating with amplitude δr and angular frequency ω in the radial direction for $t > 0$, i.e.,

$$r_b(t) = \begin{cases} r_0, & \text{for } t \leq 0, \\ r_0 + \delta r - \delta r \cos(\omega t), & \text{for } t > 0. \end{cases} \quad (5.15)$$

5.2.2 Derivations of the Space-Charge Fields

For given charge and current densities, $\rho(r, z, t)$ and $\mathbf{J}(r, z, t)$, one can compute the exact space-charge fields E_r , E_z , and B_θ using the Green's function methods discussed in the previous section. These space-charge fields are fully self-consistent and include the time-dependency of the oscillations, the initial transient start-up physics at time $t = 0$, and the effect of the image charges and image currents on the circular pipe.

By specifying the charge density in Eqn. (5.14), we are able to compute the charge density coefficients, ρ_m , in Eqn. (5.2a), which are given by

$$\begin{aligned} \rho_m(z, t) = & \frac{8Q}{\pi a^2 L} \frac{a^2}{r_b^2 j_{0m}^2 J_1^2(j_{0m})} \left[\frac{2}{j_{0m} r_b / a} J_1\left(j_{0m} \frac{r_b}{a}\right) - J_0\left(j_{0m} \frac{r_b}{a}\right) \right] \\ & \times \left[\Theta\left(z + \frac{L}{2}\right) - \Theta\left(z - \frac{L}{2}\right) \right]. \end{aligned} \quad (5.16)$$

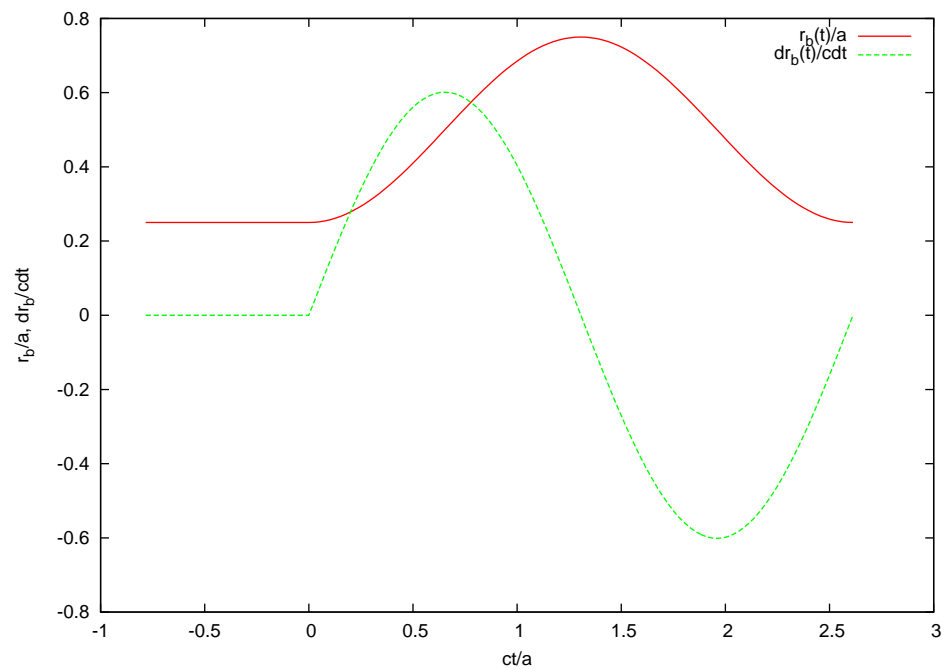


Figure 5.1: Plots of r_b and $\frac{dr_b}{dt}$ as functions of time.

Next, we calculated the coefficient of the longitudinal electric field E_{zm} from Eqn. (5.11b), using ρ_m in Eqn. (5.16). Note that we have made use of the fact that $J_{zm} = 0$ since no longitudinal currents exist when implementing Eqn. (5.11b). From Eqns. (5.11b) and (5.12a), E_{zm} can be derived as following:

$$\begin{aligned}
E_{zm} &= - \int_{-\infty}^t dt' \int dz' \left[\frac{1}{\epsilon_0} \frac{\partial \rho_m(z', t')}{\partial z'} \right] G_{0m}(z, t; z', t') \\
&= - \frac{4Q}{\pi \epsilon_0 a L} \int_{-\infty}^t \left(\frac{cdt'}{a} \right) \frac{1}{j_{0m}^2 J_1^2(j_{0m})} \frac{a^2}{r_b^2} \left[\frac{2}{j_{0m} r_b / a} J_1 \left(j_{0m} \frac{r_b}{a} \right) - J_0 \left(j_{0m} \frac{r_b}{a} \right) \right] \\
&\quad \times \left[J_0 \left(\frac{j_{0m}}{a} \lambda_+ \right) \Theta(\lambda_+^2) - J_0 \left(\frac{j_{0m}}{a} \lambda_- \right) \Theta(\lambda_-^2) \right],
\end{aligned} \tag{5.17}$$

where $\lambda_{\pm} = \sqrt{c^2(t - t')^2 - (z \pm L/2)^2}$. Therefore, the longitudinal electric field is given by

$$\begin{aligned}
E_z &= - \frac{4Q}{\pi \epsilon_0 a L} \sum_m \int_{-\infty}^t \left(\frac{cdt'}{a} \right) \frac{J_0(j_{0m} r/a)}{j_{0m}^2 J_1^2(j_{0m})} \frac{a^2}{r_b^2} \left[\frac{2}{j_{0m} r_b / a} J_1 \left(j_{0m} \frac{r_b}{a} \right) - J_0 \left(j_{0m} \frac{r_b}{a} \right) \right] \\
&\quad \times \left[J_0 \left(\frac{j_{0m}}{a} \lambda_+ \right) \Theta(\lambda_+^2) - J_0 \left(\frac{j_{0m}}{a} \lambda_- \right) \Theta(\lambda_-^2) \right],
\end{aligned} \tag{5.18}$$

Since r_b remains constant, r_0 , for $t \leq 0$, we can manipulate the time integration

in the following manner:

$$\begin{aligned}
E_z = & -\frac{4Q}{\pi\epsilon_0 a L} \sum_m \frac{J_0(j_{0m}r/a)}{j_{0m}^2 J_1^2(j_{0m})} \\
& \times \left\{ \int_{-\infty}^0 \frac{cdt'}{a} \frac{a^2}{r_b^2} \left[\frac{2}{j_{0m}r_b/a} J_1\left(j_{0m}\frac{r_b}{a}\right) - J_0\left(j_{0m}\frac{r_b}{a}\right) \right] \right. \\
& \quad + \int_0^t \frac{cdt'}{a} \frac{a^2}{r_b^2} \left[\frac{2}{j_{0m}r_b/a} J_1\left(j_{0m}\frac{r_b}{a}\right) - J_0\left(j_{0m}\frac{r_b}{a}\right) \right] \\
& \quad + \int_0^t \frac{cdt'}{a} \frac{a^2}{r_0^2} \left[\frac{2}{j_{0m}r_0/a} J_1\left(j_{0m}\frac{r_0}{a}\right) - J_0\left(j_{0m}\frac{r_0}{a}\right) \right] \\
& \quad \left. - \int_0^t \frac{cdt'}{a} \frac{a^2}{r_0^2} \left[\frac{2}{j_{0m}r_0/a} J_1\left(j_{0m}\frac{r_0}{a}\right) - J_0\left(j_{0m}\frac{r_0}{a}\right) \right] \right\} \\
& \times \left[J_0\left(\frac{j_{0m}}{a}\lambda_+\right) \Theta(\lambda_+^2) - J_0\left(\frac{j_{0m}}{a}\lambda_-\right) \Theta(\lambda_-^2) \right],
\end{aligned} \tag{5.19}$$

where we break up the integration into the two terms around $t = 0$, and add and subtract the same integration term with the radius of r_0 instead of $r_b(t)$. And then we join the second and fourth terms together, and do the same for the first and third terms. This yields

$$\begin{aligned}
E_z = & -\frac{4Q}{\pi\epsilon_0 a L} \sum_m \frac{J_0(j_{0m}r/a)}{j_{0m}^2 J_1^2(j_{0m})} \\
& \times \left[\int_0^t \frac{cdt'}{a} \left\{ \frac{a^2}{r_b^2} \left[\frac{2}{j_{0m}r_b/a} J_1\left(j_{0m}\frac{r_b}{a}\right) - J_0\left(j_{0m}\frac{r_b}{a}\right) \right] \right. \right. \\
& \quad \left. \left. + \frac{a^2}{r_0^2} \left[\frac{2}{j_{0m}r_0/a} J_1\left(j_{0m}\frac{r_0}{a}\right) - J_0\left(j_{0m}\frac{r_0}{a}\right) \right] \right\} \right. \\
& \quad \left. + \int_{-\infty}^0 \frac{cdt'}{a} \frac{a^2}{r_0^2} \left[\frac{2}{j_{0m}r_0/a} J_1\left(j_{0m}\frac{r_0}{a}\right) - J_0\left(j_{0m}\frac{r_0}{a}\right) \right] \right] \\
& \times \left[J_0\left(\frac{j_{0m}}{a}\lambda_+\right) \Theta(\lambda_+^2) - J_0\left(\frac{j_{0m}}{a}\lambda_-\right) \Theta(\lambda_-^2) \right],
\end{aligned} \tag{5.20}$$

This method is useful since the second integration term is exactly equivalent to the electrostatic part of E_z , hence there needs no integration up to a time $t = -\infty$. The

derivation of the electrostatic field will be in the Appendix B. With the electrostatic term, the final E_z field is given by

$$\begin{aligned}
E_z = & -\frac{4Q}{\pi\epsilon_0 a L} \sum_m \frac{J_0(j_{0m}r/a)}{j_{0m}^2 J_1^2(j_{0m})} \int_0^t \frac{cdt'}{a} \left[J_0\left(\frac{j_{0m}}{a}\lambda_+\right) \Theta(\lambda_+^2) - J_0\left(\frac{j_{0m}}{a}\lambda_-\right) \Theta(\lambda_-^2) \right] \\
& \times \left\{ \frac{a^2}{r_b^2} \left[\frac{2}{j_{0m}r_b/a} J_1\left(j_{0m}\frac{r_b}{a}\right) - J_0\left(j_{0m}\frac{r_b}{a}\right) \right] \right. \\
& \quad \left. + \frac{a^2}{r_0^2} \left[\frac{2}{j_{0m}r_0/a} J_1\left(j_{0m}\frac{r_0}{a}\right) - J_0\left(j_{0m}\frac{r_0}{a}\right) \right] \right\} \\
& - \frac{4Q}{\pi\epsilon_0 a L} \sum_m \frac{J_0(j_{0m}r/a)}{j_{0m}^3 J_1^2(j_{0m})} \frac{a^2}{r_0^2} \left[\frac{2}{j_{0m}r_0/a} J_1\left(j_{0m}\frac{r_0}{a}\right) - J_0\left(j_{0m}\frac{r_0}{a}\right) \right] \\
& \times \begin{cases} \left[e^{-\frac{j_{0m}}{a}(z+\frac{L}{2})} - e^{-\frac{j_{0m}}{a}(z-\frac{L}{2})} \right] & \text{for } z > \frac{L}{2} \\ \left[e^{-\frac{j_{0m}}{a}(z+\frac{L}{2})} - e^{\frac{j_{0m}}{a}(z-\frac{L}{2})} \right] & \text{for } |z| \leq \frac{L}{2} \\ \left[e^{\frac{j_{0m}}{a}(z+\frac{L}{2})} - e^{\frac{j_{0m}}{a}(z-\frac{L}{2})} \right] & \text{for } z < -\frac{L}{2} \end{cases} .
\end{aligned} \tag{5.21}$$

One can build up the transverse electromagnetic field components, E_r and B_θ , using Eqns. (5.11a) and (5.11c) with ρ_m and J_{rm} . However, calculations of the time integrations for different integrands requires large computational resources. As mentioned in the previous section, we can reduce these tasks by using the relations from the Maxwell's equations (Eqn. (5.13)). For given charge and current densities, it is easy to find at least one field coefficient, for example, E_{zm} , in this numerical example, as well as those of charge and current densities. Then, we can use these coefficients to derive other components.

Henceforth, the transverse space-charge electric field coefficients E_{rm} and $B_{\theta m}$ can be found from E_{zm} and ρ_m using Eqns. (5.13c) and (5.13f), respectively, i.e.,

$$E_r = \sum_m \frac{a}{j_{0m}} \left(\frac{1}{\epsilon_0} \rho_m - \frac{\partial E_{zm}}{\partial z} \right) J_1\left(j_{0m}\frac{r}{a}\right) \tag{5.22a}$$

and

$$\begin{aligned}
 B_\theta &= \sum_m \frac{a}{j_{0m}} \left(\mu J_{zm} + \frac{1}{c^2} \frac{\partial E_{zm}}{\partial t} \right) J_1 \left(j_{0m} \frac{r}{a} \right) \\
 &= \sum_m \frac{a}{j_{0m}} \frac{1}{c^2} \frac{\partial E_{zm}}{\partial t} J_1 \left(j_{0m} \frac{r}{a} \right).
 \end{aligned} \tag{5.22b}$$

Note that we have made use of the fact that $J_{zm} = 0$ since no longitudinal currents exist when implementing Eqn. (5.22b). Using the relation,

$$\begin{aligned}
 &\frac{\partial}{\partial z} J_0 \left(\frac{j_{0m}}{a} \lambda_\pm \right) \Theta(\lambda_\pm^2) \\
 &= \frac{\partial \lambda_\pm}{\partial z} \frac{\partial}{\partial \lambda_\pm} \left[J_0 \left(\frac{j_{0m}}{a} \lambda_\pm \right) \Theta(\lambda_\pm^2) \right] \\
 &= \frac{z \pm L/2}{\lambda_\pm} \left[\frac{j_{0m}}{a} J_1 \left(\frac{j_{0m}}{a} \lambda_\pm \right) \Theta(\lambda_\pm^2) - 2\lambda_\pm J_0 \left(\frac{j_{0m}}{a} \lambda_\pm \right) \delta(\lambda_\pm^2) \right],
 \end{aligned} \tag{5.23}$$

the radial electromagnetic space-charge field is derived as

$$\begin{aligned}
E_r = & \frac{8Q}{\pi\epsilon_0 a L} \sum_m \frac{J_1(j_{0m}r/a)}{j_{0m}^3 J_1^2(j_{0m})} \\
& \times \frac{a^2}{r_b^2} \left[\frac{2}{j_{0m}r_b/a} J_1\left(j_{0m}\frac{r_b}{a}\right) - J_0\left(j_{0m}\frac{r_b}{a}\right) \right] \left[\Theta\left(z + \frac{L}{2}\right) - \Theta\left(z - \frac{L}{2}\right) \right] \\
& + \frac{4Q}{\pi\epsilon_0 a L} \sum_m \int_0^t \frac{cdt'}{a} \frac{J_1(j_{0m}r/a)}{j_{0m}^2 J_1^2(j_{0m})} \\
& \times \left\{ \frac{a^2}{r_b^2} \left[\frac{2}{j_{0m}r_b/a} J_1\left(j_{0m}\frac{r_b}{a}\right) - J_0\left(j_{0m}\frac{r_b}{a}\right) \right] \right. \\
& \quad \left. + \frac{a^2}{r_0^2} \left[\frac{2}{j_{0m}r_0/a} J_1\left(j_{0m}\frac{r_0}{a}\right) - J_0\left(j_{0m}\frac{r_0}{a}\right) \right] \right\} \\
& \times \left\{ \frac{z + L/2}{\lambda_+} \left[J_1\left(\frac{j_{0m}}{a}\lambda_+\right) \Theta(\lambda_+^2) - \frac{2a}{j_{0m}}\lambda_+ J_0\left(\frac{j_{0m}}{a}\lambda_+\right) \delta(\lambda_+^2) \right] \right. \\
& \quad \left. - \frac{z - L/2}{\lambda_-} \left[J_1\left(\frac{j_{0m}}{a}\lambda_-\right) \Theta(\lambda_-^2) - \frac{2a}{j_{0m}}\lambda_- J_0\left(\frac{j_{0m}}{a}\lambda_-\right) \delta(\lambda_-^2) \right] \right\} \\
& - \frac{4Q}{\pi\epsilon_0 a L} \sum_m \frac{J_1(j_{0m}r/a)}{j_{0m}^3 J_1^2(j_{0m})} \frac{a^2}{r_0^2} \left[\frac{2}{j_{0m}r_0/a} J_1\left(j_{0m}\frac{r_0}{a}\right) - J_0\left(j_{0m}\frac{r_0}{a}\right) \right] \\
& \times \begin{cases} \left[e^{-\frac{j_{0m}}{a}(z+\frac{L}{2})} - e^{-\frac{j_{0m}}{a}(z-\frac{L}{2})} \right] & \text{for } z > \frac{L}{2} \\ \left[e^{-\frac{j_{0m}}{a}(z+\frac{L}{2})} + e^{\frac{j_{0m}}{a}(z-\frac{L}{2})} \right] & \text{for } |z| \leq \frac{L}{2} \\ \left[-e^{\frac{j_{0m}}{a}(z+\frac{L}{2})} + e^{\frac{j_{0m}}{a}(z-\frac{L}{2})} \right] & \text{for } z < -\frac{L}{2} \end{cases} .
\end{aligned} \tag{5.24}$$

In the derivation of B_θ , there needs more delicate consideration since both integrands and the integration range in the time integration of E_{zm} depend on the differential variable t . Let the integrands be $f(t, t')$, then the time integration can be simply derived as

$$\frac{\partial}{\partial t} \int_{-\infty}^t dt' f(t, t') = f(t, t) + \int_{-\infty}^t dt' \frac{\partial}{\partial t} f(t, t'). \tag{5.25}$$

In Eqn. (5.25), $f(t, t)$ is always zero since $\lambda_\pm^2 = c^2(t - t')^2 - (z \pm L/2)^2$ are less than or equal to zero at $t' = t$, i.e., $\Theta(\lambda_\pm^2)$ do not contribute to the calculation.

And the time derivatives of the Bessel functions in the integrands are similar to Eqn. (5.23) as

$$\begin{aligned}
& \frac{\partial}{\partial t} J_0 \left(\frac{j_{0m}}{a} \lambda_{\pm} \right) \Theta(\lambda_{\pm}^2) \\
&= \frac{\partial \lambda_{\pm}}{\partial t} \frac{\partial}{\partial \lambda_{\pm}} \left[J_0 \left(\frac{j_{0m}}{a} \lambda_{\pm} \right) \Theta(\lambda_{\pm}^2) \right] \\
&= - \frac{c^2(t-t')}{\lambda_{\pm}} \left[\frac{j_{0m}}{a} J_1 \left(\frac{j_{0m}}{a} \lambda_{\pm} \right) \Theta(\lambda_{\pm}^2) - 2\lambda_{\pm} J_0 \left(\frac{j_{0m}}{a} \lambda_{\pm} \right) \delta(\lambda_{\pm}^2) \right].
\end{aligned} \tag{5.26}$$

Therefore, using Eqns. (5.9b), (5.21), and (5.26)

$$\begin{aligned}
B_{\theta} &= \frac{4Q}{\pi \epsilon_0 a L} \sum_m \int_0^t \frac{cdt'}{a} \frac{J_1(j_{0m}r/a)}{j_{0m}^2 J_1^2(j_{0m})} \\
&\times \left\{ \frac{a^2}{r_b^2} \left[\frac{2}{j_{0m}r_b/a} J_1 \left(j_{0m} \frac{r_b}{a} \right) - J_0 \left(j_{0m} \frac{r_b}{a} \right) \right] \right. \\
&\quad \left. + \frac{a^2}{r_0^2} \left[\frac{2}{j_{0m}r_0/a} J_1 \left(j_{0m} \frac{r_0}{a} \right) - J_0 \left(j_{0m} \frac{r_0}{a} \right) \right] \right\} \\
&\times \left\{ \frac{c^2(t-t')}{\lambda_+} \left[J_1 \left(\frac{j_{0m}}{a} \lambda_+ \right) \Theta(\lambda_+^2) - \frac{2a}{j_{0m}} \lambda_+ J_0 \left(\frac{j_{0m}}{a} \lambda_+ \right) \delta(\lambda_+^2) \right] \right. \\
&\quad \left. - \frac{c^2(t-t')}{\lambda_-} \left[J_1 \left(\frac{j_{0m}}{a} \lambda_- \right) \Theta(\lambda_-^2) - \frac{2a}{j_{0m}} \lambda_- J_0 \left(\frac{j_{0m}}{a} \lambda_- \right) \delta(\lambda_-^2) \right] \right\}.
\end{aligned} \tag{5.27}$$

5.2.3 Numerical Requirements

As demonstrated in the previous chapter, the numerical requirements to analyze the electromagnetic fields are studied. The number of radial eigenmodes needed for good convergence scales inversely proportional to the radial size of the perturbation which is being analyzed. Figure 5.2 shows normalized E_r vs. r/a at time $t = 0.25T$, where $T(= 2\pi/\omega)$ is the characteristic beam oscillation period, i.e., the beam edge is at $r = r_0 + \delta r = 0.5a$ for $r_0 = 0.25a$ and $\delta r = 0.25a$. In Figure 5.2, the normalized radial electric field is plotted for $m = 5$ radial modes (red:solid), $m = 10$ modes

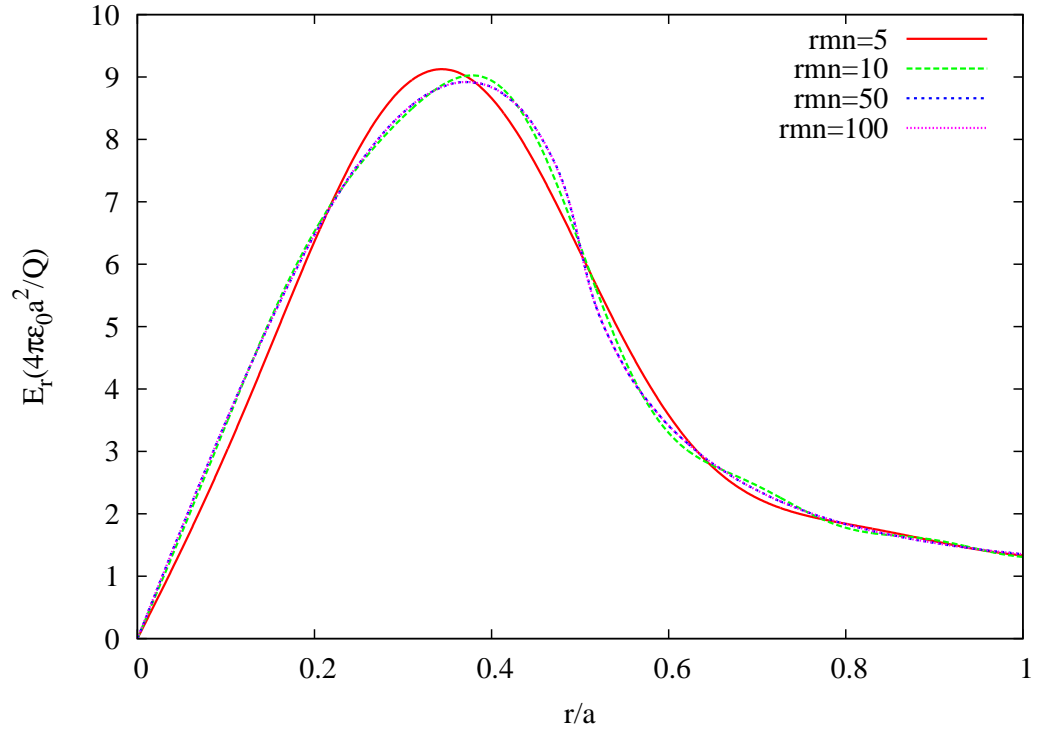


Figure 5.2: Plots of the normalized radial electric field at $z = 0$ and $t = 0.25T$ are plotted using 5 radial modes (red:solid), 10 modes (green:dashed), 50 modes (blue:dotted), and 100 modes (pink:dashed-dotted) (\mathbf{rmn} is the radial eigenmode number).

(green:dashed), $m = 50$ modes (blue:dotted), and $m = 100$ modes (pink:dashed-dotted).

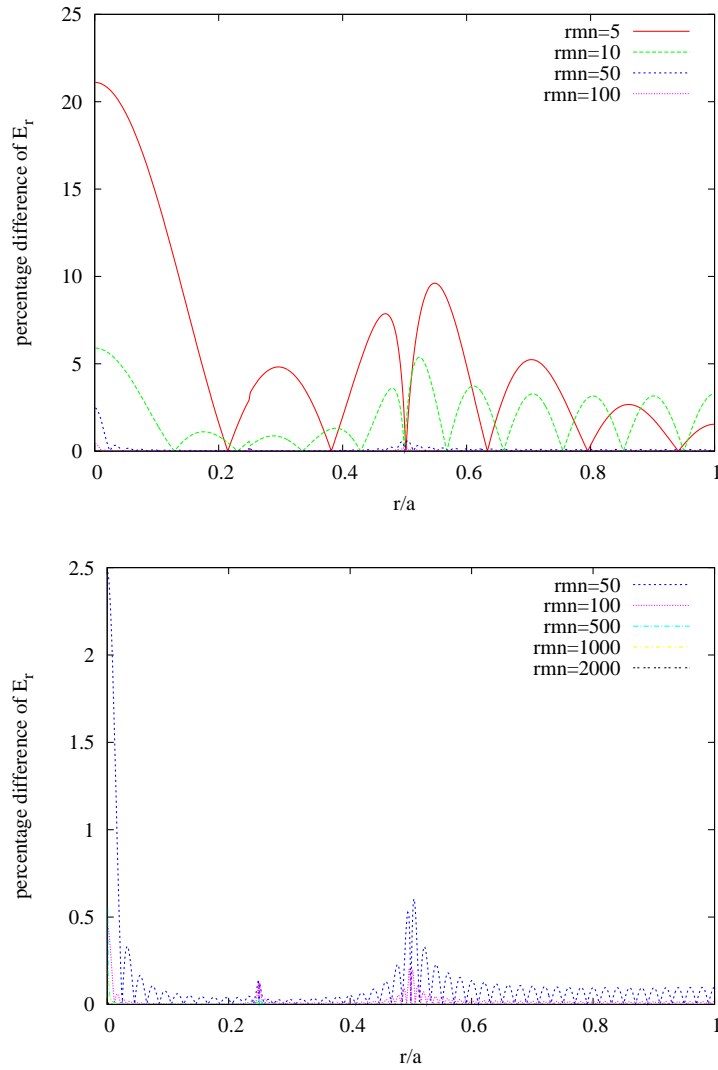


Figure 5.3: Plots of the percentage error of the normalized radial electric field at $z = 0$ and time $t = 0$.

Figure 5.3 shows the percentage difference of the normalized radial electric field

for different eigenmodes. The differences are calculated from $m = 2000$ modes. We note that as we increase the eigenmode number E_r is rapidly converged, such that the difference between $m = 100$ and $m = 500$ modes is already negligible. It is obvious that most discrepancies are occurred at $r = 0.0$, $r = 0.25a = r_0$ and $r = 0.5a = r_b$, since the eigenmode summations are conducted around these radii as seen in Eqn. (5.24). In order to achieve higher accuracy, we use $m = 1000$ modes for the following numerical examples.

In Eqns. (5.21), (5.24), and (5.27), numerical time integrations needs restrictions for integration time step size, as previously discussed in Chapter 3. The time step size must be small enough to resolve the radial oscillation of the beam, which is represented by the Green's function found in the Eqns. (5.21), (5.24), and (5.27). In Chapter 3 for computing the electromagnetic space-charge fields due to the longitudinal motion of the beam, we found that the time step size is restricted by the relation $\Delta t' \ll 0.01r_b/c$. In order to achieve highly accurate fields, the step size was 10^{-6} in normalized units.

When we compare Eqn. (3.38) and (5.24), for example, the temporal part in the time integration is very similar, although the beam radius in the present work also depends on the integration variable t' . Hence, one can expect that the required time step size has to be in the same criteria. However, the temporal part of the rf photoinjector study is more complicated, i.e., it has the dependence of the longitudinal beam trajectory, $z''(t)$, while there is no longitudinal motion in this model. Therefore, the requirements of the time-step size for the integration is less restricted than those in the previous work. Moreover, for the parameters in this example, the beam radius is varying from $0.25a$ to $0.75a$, so that a time step of $\Delta t' = 0.0001a/c$ is enough to get excellent numerical convergence.

5.2.4 Space-Charge Fields with Transverse Current

As an example of the transverse current model, we show the plots of the normalized radial electric field vs. r at the middle of the bunch, $z = 0$ and the normalized longitudinal electric field vs. z/a at the axis, $r = 0$ and vs. r/a at $z = 0.001$ for different times, which are related to the characteristic beam oscillation period, $T(= 2\pi/\omega)$. We choose times, $t = 0$, $t = 0.25T$, $t = 0.5T$, $t = 0.75T$, and $t = T$, in which the beam is oscillating for one full period. The plot of normalized azimuthal magnetic field is excluded, since it is zero at the bunch mid-plane, $z = 0$, as well as, at the axis, $r = 0$, due to the symmetry. But it is non-zero at different r and z values.

In order to find the electromagnetic effects, the electrostatic space-charge fields are also calculated and are plotted for the comparison. The electrostatic fields are also found using the electrostatic Green's function [34], and the detailed derivations are shown in the previous section. The beam oscillation starts with the initial beam radius, $r_b = 0.25a$, the radial variation, $\delta r = 0.25a$, and the oscillating frequency is $\omega = j_{01}c/a$, where a is the pipe radius of 0.0908 m . All field calculations are fulfilled with the numerical requirements, i.e., $m = 1000$ modes and $\Delta t' = 0.0001a/c$.

Figure 5.4 shows plots of normalized E_r vs. r for different times during one characteristic beam oscillation period. The red-solid curve is the electrostatic field, while the blue-dashed curve is the electromagnetic field. Figure 5.4 has plots of the normalized radial electric field at $z = 0.0$ for times $t = 0$ (Figure 5.4(a)), $t = 0.25T$ (Figure 5.4(b)), $t = 0.5T$ (Figure 5.4(c)), $t = 0.75T$ (Figure 5.4(d)), and $t = T$ (Figure 5.4(e)). Since the beam is not oscillating for $t \leq 0$, the two electric fields at $t = 0$ are exactly same, i.e., fully electrostatic, as shown in Figure 5.4(a). At time $t = 0.5T$, the beam has the maximum radius, $r_b = r_0 + 2\delta r = 0.75a$. We see that the solution of the electrostatic field is underestimated by about 10 % compared to the electromagnetic field in Figure 5.4(c). For $t = T$, however, one can see that the elec-

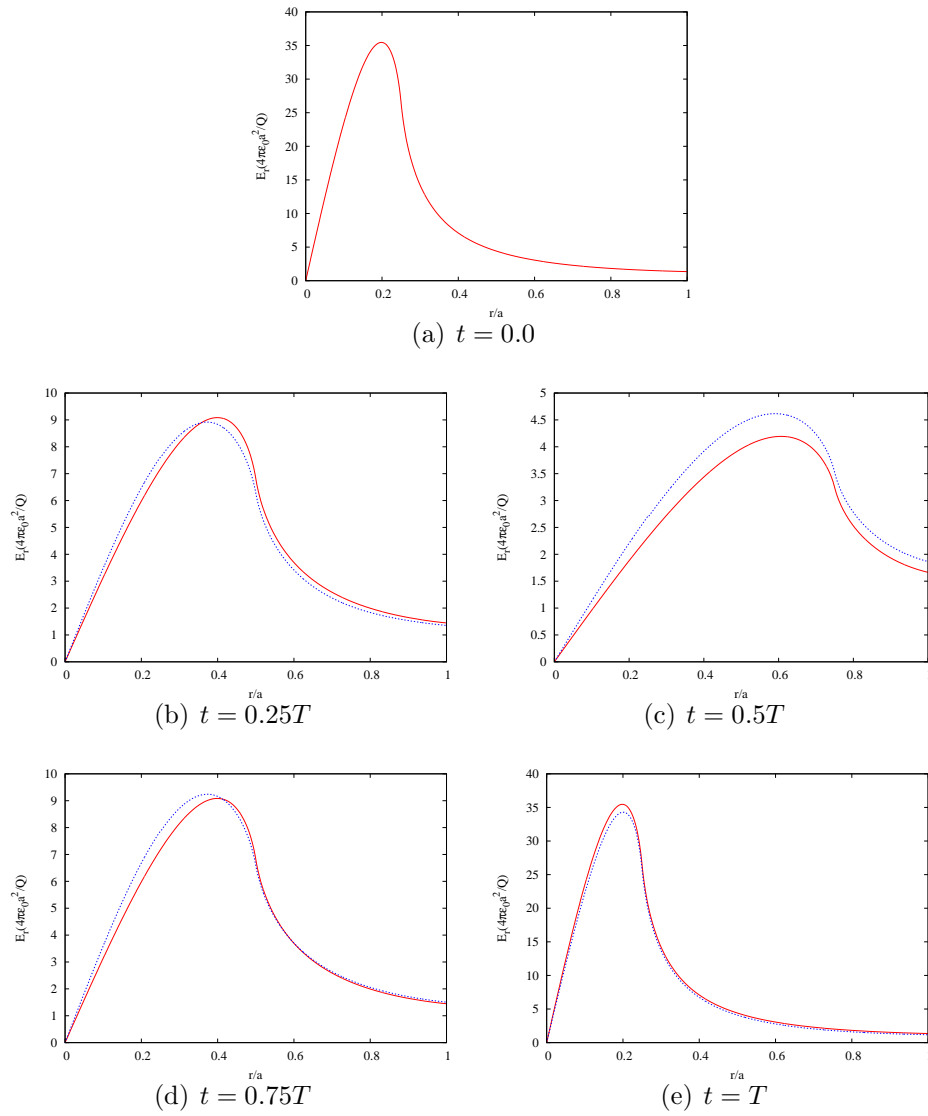


Figure 5.4: Plots of the normalized radial electric field at $z = 0$ and at time (a) $t = 0$, (b) $t = 0.25T$, (c) $t = 0.5T$, (d) $t = 0.75T$, and (e) $t = T$ computed electrostatically (red:solid) and electromagnetically (blue:dashed).

trostatic field is overestimated compared to the electromagnetic field. Since the beam distribution is parabolic in the transverse direction, the peak is located at slightly less than the beam edge. When we compare the two field solutions for times $t = 0.25T$ and $t = 0.75T$, where the beam radii for both cases are $r_b = r_0 + \delta r = 0.5a$, the electrostatic field is underestimated or overestimated around the peak. However, the peak electromagnetic field for $t = 0.25T$ is less than the peak of the electrostatic field, while the peak electromagnetic field for $t = 0.75T$ is larger than the peak electrostatic field. This is because the beam is radially oscillating in the outward direction for $t = 0.25T$, while it is moving inward for $t = 0.75T$. For $t = T$, one can see that the electrostatic field is overestimated compared to the electromagnetic field.

Figure 5.5 shows plots of a normalized E_z vs. z at $r = 0$ (Figure 5.5(a)) and $r = 0.25a$ (Figure 5.5(b)) for the times $t = 0$, $t = 0.25T$, $t = 0.5T$, $t = 0.75T$, and $t = T$. From Figure 5.5, it is immediately apparent that E_z is maximum at $t = 0$ and $t = T$. This is easily explained by the fact that as the bunch radius increases, the beam charge density at $r = 0$ decreases leading to a smaller E_z . We find that while the difference in E_z as found by electrostatic and electromagnetic methods at $r = 0$ and at times $t = 0$ and $t = T$ for these parameters is negligible, the difference in E_z is approximately 20% at times $t = 0.25T$ and $t = 0.75T$ near the longitudinal beam edges and increases to 40% at time $t = 0.5T$. When we compare Figures 5.5(a) and 5.5(b) near the longitudinal beam edge, the electrostatic solutions are underestimated on the beam center, $r = 0$, while those are overestimated as r is increased. Therefore, the effects of the longitudinal electromagnetic space-charge fields are important near the beam edge for the radially oscillating beam as described in this example.

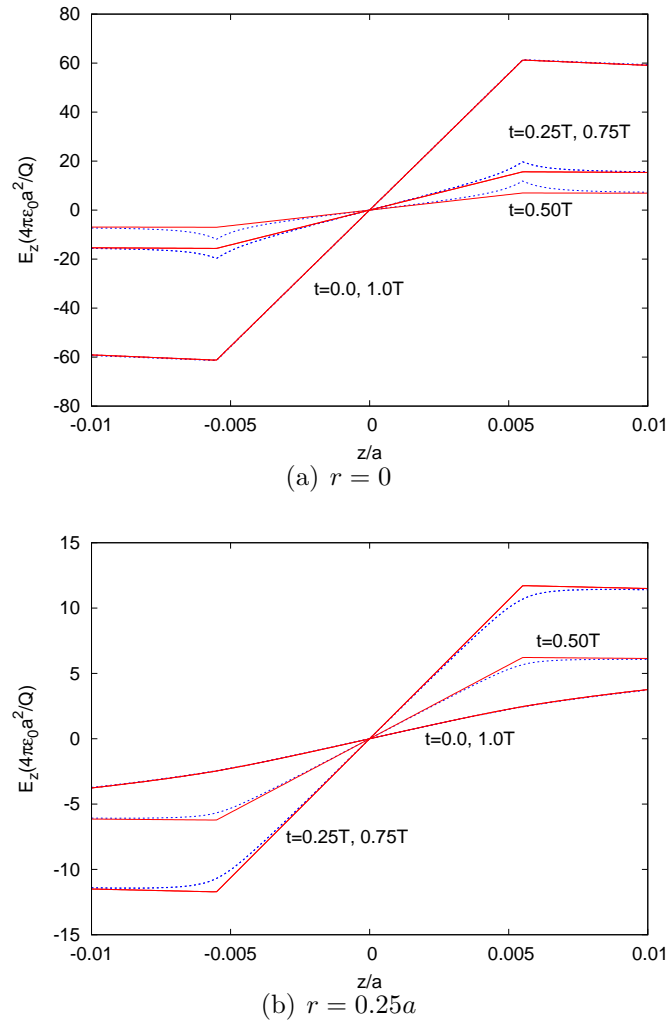


Figure 5.5: Plots of the normalized longitudinal electric field at (a) $r = 0$ and (b) $r = 0.25a$ for times $t = 0$, $t = 0.25T$, $t = 0.5T$, $t = 0.75T$, and $t = T$ computed electrostatically (red:solid) and electromagnetically (blue:dashed).

Chapter 6

Conclusions and Future Plans

In this dissertation, we have presented electromagnetic space-charge models of electron beams in the presence of conducting boundaries in accelerators. We utilized Green's function methods to derive analytical solutions of the electromagnetic space-charge potentials and fields in the pipe structures. We have developed a novel computational code, called IRPSS, to compute these fields numerically. Specifically, we calculated the space-charge fields in the RF photoinjector, and then simulated the beam dynamics near the cathode. The numerical results were compared with those of an electrostatic code. We found significant differences between electromagnetic and electrostatic space-charge fields. In addition, we also extended our Green's function techniques by including transverse currents. We applied this method to investigate the electromagnetic space-charge fields for a radially “breathing beam” oscillation. At the end of this chapter, we will provide future plans to enhance the IRPSS code for modeling the rf photoinjector and high-power microwave sources.

6.1 Space-Charge Modeling of the RF Photoinjector

In Chapter 3, we have presented analytical solutions of the electromagnetic fields inside of a pipe structure with the flat cathode at $z = 0$ using a compact Green's function method. These solutions include effects of image charges and currents due to the cathode boundary and the necessary causality condition due to the finite speed of light. The accuracy of this method is verified using a benchmark study.

As an example to model the rf photoinjector, we showed the exact solutions of the electromagnetic space-charge fields within the cylindrical pipe. The code, IRPSS, has an ability to calculate the space-charge fields in the rf photoinjector. We found the necessary numerical requirements for eigenmode summations and time integrations to achieve high accuracies, i.e., $< 1\%$ errors. To model a finite-size bunched beam, a multi-slice method was introduced.

In order to resolve the electromagnetic fields, the distribution function of the zero-thickness beam was expanded in terms of transverse eigenfunctions. We estimated the required eigenmode number for a given charge distribution. The minimum eigenmode number depends on the radial beam size of the system. For example, at least 2000 eigenmodes are needed to get accurate results for the BNL 2.856 GHz rf photoinjector. The time integrations are conducted with the time evolution of the beam. The numerical simulation showed that the time integration step, $c\Delta t'/a$, must be also much less than a/c .

Since the real beam has a finite longitudinal bunch length, the multi-sliced bunch model is introduced. Each slice with zero-thickness has an equal amount of charge, but total charge is conserved. We found the required number of slices to express the finite size beam. For a 9 ps bunch length withing the AWA gun, we modeled the

longitudinally uniform beam with the multi-sliced beam, using 41 slices.

6.2 Application to the RF Photoinjector

The computational code, IRPSS, was developed to solve the electromagnetic space-charge fields and to track the electron beam in the rf photoinjector. First, we examined how the electromagnetic space-charge fields differed from the electrostatic fields near the cathode.

The electrostatic space-charge fields were calculated in two ways: (1) the discretized bunch method with multi-slices, which is similar to the electromagnetic field calculations, and (2) the uniformly finite bunch with constant J_z . These two methods agreed very well, and verified our electrostatic results. The comparisons between electromagnetic and electrostatic forces showed that there are significant discrepancies in transverse space-charge force near the cathode, and the differences were decreased as the beam was moving away from the cathode.

In addition, we studied the effect of time-retardation in the rf photoinjector during the emission of the electron beam. This study was done by measuring the beamloss both numerically with electromagnetic and electrostatic space-charge field solvers and experimentally in the ANL AWA 1.3 *GHz* rf photoinjector. Discrepancies were found between two critical space-charge fields, especially, for beams with longer bunch length.

6.3 Transverse Current Modeling

Chapter 5 extended the previous Green's function technique including the effects of the transverse beam currents. We assumed that the beam is cylindrically symmetric and the geometry of the conducting cavity system is also cylindrically symmetric.

With the help of these symmetries, we expanded the beam charge and current densities, and the electromagnetic space-charge fields in terms of series of Bessel functions. These formed a set of differential equations from Maxwell's equations, and we found the solutions using the time-dependent Green's function methods. The Green's functions automatically satisfied the boundary conditions.

Using this formalism, we derived the analytical solutions of the electromagnetic space-charge fields in the presence of azimuthal beam currents or radial and longitudinal beam currents. As a numerical example, we computed the space-charge fields for a radially "breathing" bunched beam, which can be realizable in a klystron drift tube. When we compared the electromagnetic fields with those of the electrostatic method, the differences between these two fields were non-negligible. The main differences of the longitudinal space-charge fields occurred near the beam edge up to 20%. Moreover, the differences in the transverse space-charge fields were varying as the beam is radially moving inward or outward. These numerical comparisons tells us that our space-charge formalism may play an important role in modeling space-charge dominated beams in high-power microwave sources, such as a klystron.

6.4 Future Plans

In the modeling of rf photoinjectors, we simplified the geometry of the system only with the conducting cavity and the flat cathode. We are planning to extend the IRPSS code by including the effects of iris(es) or discontinuities of the cavity. These effects can be applied by various approaches, however, we are currently focused on the method developed by H. Bethe. This method includes the effects of the hole between two consecutive cavities using the perturbative approximations of field expansions. To the lowest order, the hole effects are assumed to be equivalent to oscillating electric and magnetic multipole moments. The superposition of the field expansion, which

is computed without iris(es), and the multipole moments will represent the total electromagnetic space-charge fields.

The space-charge field calculations with the IRPSS code in the current stage are less self-consistent since we used the prescribed beam trajectory, which is calculated in the presence of the external rf field. This assumption is valid when we examine the beam dynamics near the cathode. However, the beam distribution will be changed as the beam passes through the gun. We will improve the code to self-consistently calculate the trajectories due to both the external fields and the space-charge fields.

We are also planning to study how the beam dynamics can be affected due to the electromagnetic space-charge fields in the designs of magnetic focusing schemes for photoinjector guns, such as emittance compensation methods. This study will investigate how the fields, such as rf, solenoid, and space-charge fields, are coupled. More improved experimental measurements will be performed to see the time-retardation effects in the rf photoinjector.

In addition, we are developing space-charge field solvers, which can include arbitrary beam currents, for example, azimuthally varying currents. Moreover, we are also developing the analytical techniques for including more complicated conducting geometries, such as coaxial structures, and for various beam charge and current distributions, such as annular beams.

Appendix A

Electromagnetic Space-Charge Fields

In this chapter, we will derive the electromagnetic space-charge potentials and fields using Green's function methods for the circularly symmetric pipe with the flat cathode. We assume that the beam has only longitudinal currents. Then, the charge and current densities of the zero-thickness beam are given by

$$\rho(\mathbf{r}, t) = \frac{2Q}{\pi r_b^2} \left(1 - \frac{r^2}{r_b^2}\right) \Theta(r_b - r) \delta[z - z''(t)], \quad (\text{A.1a})$$

and

$$J_z(\mathbf{r}, t) = \frac{2Q}{\pi r_b^2} \left(1 - \frac{r^2}{r_b^2}\right) \Theta(r_b - r) \delta[z - z''(t)] \frac{dz''(t)}{dt}, \quad (\text{A.1b})$$

where Q is the bunch charge, r_b is the beam radius, and $z''(t)$ is the slice location at time t . We normalize the variables by the pipe radius, a , and the speed of light, c , such as, $\hat{r} = r/a$, $\hat{z} = z/a$, and $\tau = ct/a$. All normalized quantities are dimensionless.

A.1 Scalar and Vector Potentials

The scalar and vector potentials can be obtained by the Green's function methods:

$$\phi(\mathbf{r}, t) = \frac{1}{\epsilon_0} \int_{-\infty}^t \int G_\phi(\mathbf{r}, t; \mathbf{r}', t') \rho(\mathbf{r}', t') d^3r' dt', \quad (\text{A.2a})$$

and

$$A_z(\mathbf{r}, t) = \mu_0 \int_{-\infty}^t \int G_A(\mathbf{r}, t; \mathbf{r}', t') J_z(\mathbf{r}', t') d^3r' dt', \quad (\text{A.2b})$$

where

$$G_\phi = \frac{c}{2} \sum_{mn} \psi_{mn}(\mathbf{r}_\perp) \psi_{mn}^*(\mathbf{r}'_\perp) \left[J_0\left(j_{mn} \frac{\lambda_{0-}}{a}\right) \Theta(\lambda_{0-}^2) - J_0\left(j_{mn} \frac{\lambda_{0+}}{a}\right) \Theta(\lambda_{0+}^2) \right], \quad (\text{A.3a})$$

$$G_A = \frac{c}{2} \sum_{mn} \psi_{mn}(\mathbf{r}_\perp) \psi_{mn}^*(\mathbf{r}'_\perp) \left[J_0\left(j_{mn} \frac{\lambda_{0-}}{a}\right) \Theta(\lambda_{0-}^2) + J_0\left(j_{mn} \frac{\lambda_{0+}}{a}\right) \Theta(\lambda_{0+}^2) \right], \quad (\text{A.3b})$$

$$\psi_{mn}(\mathbf{r}_\perp) = \frac{1}{a\sqrt{\pi}} \frac{J_m(j_{mn}r/a) e^{im\theta}}{|J_{m+1}(j_{mn})|}, \quad (\text{A.3c})$$

and

$$\lambda_{0\pm}^2 = c^2(t - t') - (z \pm z')^2. \quad (\text{A.3d})$$

With the simple algebraic calculation, the scalar and vector potentials are given by

$$\begin{aligned} \phi(r, z, t) &= \frac{4cQ}{\pi\epsilon_0 r_b^2} \sum_{n=0}^{\infty} \frac{J_0(j_{0n} \frac{r}{a})}{j_{0n}^2 |J_1(j_{0n})|^2} \left[\frac{2}{j_{0n} r_b/a} J_1\left(j_{0n} \frac{r_b}{a}\right) - J_0\left(j_{0n} \frac{r_b}{a}\right) \right] \\ &\quad \times \int_{-\infty}^t dt' \left[J_0\left(j_{0n} \frac{\lambda_-}{a}\right) \Theta(\lambda_-^2) - J_0\left(j_{0n} \frac{\lambda_+}{a}\right) \Theta(\lambda_+^2) \right] \\ &= \frac{4Q}{\pi\epsilon_0 \hat{r}_b^2 a} \sum_{n=0}^{\infty} \frac{J_0(j_{0n} \hat{r})}{j_{0n}^2 |J_1(j_{0n})|^2} \left[\frac{2}{j_{0n} \hat{r}_b} J_1(j_{0n} \hat{r}_b) - J_0(j_{0n} \hat{r}_b) \right] \\ &\quad \times \int_{-\infty}^{\tau} d\tau' \left[J_0(j_{0n} \hat{\lambda}_-) \Theta(\hat{\lambda}_-^2) - J_0(j_{0n} \hat{\lambda}_+) \Theta(\hat{\lambda}_+^2) \right], \end{aligned} \quad (\text{A.4a})$$

and

$$\begin{aligned}
A_z(r, z, t) &= \frac{4cQ\mu_0}{\pi r_b^2} \sum_{n=0}^{\infty} \frac{J_0(j_{0n} \frac{r}{a})}{j_{0n}^2 |J_1(j_{0n})|^2} \left[\frac{2}{j_{0n} \frac{r_b}{a}} J_1(j_{0n} \frac{r_b}{a}) - J_0(j_{0n} \frac{r_b}{a}) \right] \\
&\times \int_{-\infty}^t dt' \left[J_0(j_{0n} \frac{\lambda_-}{a}) \Theta(\lambda_-^2) + J_0(j_{0n} \frac{\lambda_+}{a}) \Theta(\lambda_+^2) \right] \left[\frac{dz''(t)}{dt} \right]_{t=t'} \\
&= \frac{4cQ\mu_0}{\pi \hat{r}_b^2 a} \sum_{n=0}^{\infty} \frac{J_0(j_{0n} \hat{r})}{j_{0n}^2 |J_1(j_{0n})|^2} \left[\frac{2}{j_{0n} \hat{r}_b} J_1(j_{0n} \hat{r}_b) - J_0(j_{0n} \hat{r}_b) \right] \\
&\times \int_{-\infty}^{\tau} d\tau' \left[J_0(j_{0n} \hat{\lambda}_-) \Theta(\hat{\lambda}_-^2) + J_0(j_{0n} \hat{\lambda}_+) \Theta(\hat{\lambda}_+^2) \right] \left[\frac{d\hat{z}''(\tau)}{d\tau} \right]_{\tau=\tau'},
\end{aligned} \tag{A.4b}$$

where λ_{\pm}^2 and $\hat{\lambda}_{\pm}^2$ are given by

$$\lambda_{\pm}^2 = c^2 (t - t')^2 - [z \pm z''(t')]^2, \tag{A.5a}$$

and

$$\hat{\lambda}_{\pm}^2 = (\tau - \tau')^2 - [\hat{z} \pm \hat{z}''(\tau')]^2. \tag{A.5b}$$

The electromagnetic fields can be obtained from these potentials.

$$\begin{cases} \vec{E} = -\vec{\nabla}\phi - \frac{\partial \vec{A}}{\partial t}, \\ \vec{B} = \vec{\nabla} \times \vec{A}. \end{cases} \tag{A.6}$$

A.2 Transverse Electric and Magnetic Fields

Using Eqns. (A.4) and (A.6), it is easy to derive the transverse electric and magnetic fields, and they are given by

$$\begin{aligned}
E_r(r, z, t) &= -\frac{\partial \phi}{\partial r} \\
&= \frac{4Q}{\pi \epsilon_0 \hat{r}_b^2 a^2} \sum_{n=0}^{\infty} \frac{J_1(j_{0n} \hat{r})}{j_{0n} |J_1(j_{0n})|^2} \left[\frac{2}{j_{0n} \hat{r}_b} J_1(j_{0n} \hat{r}_b) - J_0(j_{0n} \hat{r}_b) \right] \\
&\times \int_{-\infty}^{\tau} d\tau' \left[J_0(j_{0n} \hat{\lambda}_-) \Theta(\hat{\lambda}_-^2) - J_0(j_{0n} \hat{\lambda}_+) \Theta(\hat{\lambda}_+^2) \right],
\end{aligned} \tag{A.7a}$$

and

$$\begin{aligned}
B_\theta(r, z, t) &= -\frac{\partial A_z}{\partial r} \\
&= \frac{4cQ\mu_0}{\pi\hat{r}_b^2 a^2} \sum_{n=0}^{\infty} \frac{J_1(j_{0n}\hat{r})}{j_{0n}|J_1(j_{0n})|^2} \left[\frac{2}{j_{0n}\hat{r}_b} J_1(j_{0n}\hat{r}_b) - J_0(j_{0n}\hat{r}_b) \right] \\
&\quad \times \int_{-\infty}^{\tau} d\tau' \left[J_0(j_{0n}\hat{\lambda}_-) \Theta(\hat{\lambda}_-^2) + J_0(j_{0n}\hat{\lambda}_+) \Theta(\hat{\lambda}_+^2) \right] \left[\frac{d\hat{z}''(\tau)}{d\tau} \right]_{\tau=\tau'}
\end{aligned} \tag{A.7b}$$

Using the relation, $c^2 = (\mu_0\epsilon_0)^{-1}$,

$$\begin{aligned}
cB_\theta(r, z, t) &= \frac{4Q}{\pi\epsilon_0\hat{r}_b^2 a^2} \sum_{n=0}^{\infty} \frac{J_1(j_{0n}\hat{r})}{j_{0n}|J_1(j_{0n})|^2} \left[\frac{2}{j_{0n}\hat{r}_b} J_1(j_{0n}\hat{r}_b) - J_0(j_{0n}\hat{r}_b) \right] \\
&\quad \times \int_{-\infty}^{\tau} d\tau' \left[J_0(j_{0n}\hat{\lambda}_-) \Theta(\hat{\lambda}_-^2) + J_0(j_{0n}\hat{\lambda}_+) \Theta(\hat{\lambda}_+^2) \right] \left[\frac{d\hat{z}''(\tau)}{d\tau} \right]_{\tau=\tau'}.
\end{aligned} \tag{A.8}$$

A.3 Longitudinal Electric Field

A.3.1 Derivation of E_z

The longitudinal electric field is evaluated from

$$E_z = -\frac{\partial\phi}{\partial z} - \frac{\partial A_z}{\partial t}. \tag{A.9}$$

And we will derive each term separately.

$$\text{I} \quad -\frac{\partial\phi}{\partial z}$$

Since the time integration variable t' is independent of z , it is easy to take a partial derivative of ϕ with respect to z , i.e.,

$$\begin{aligned}
-\frac{\partial\phi}{\partial z} &= -\frac{4cQ}{\pi\epsilon_0 r_b^2} \sum_{n=0}^{\infty} \frac{J_0(j_{0n}\frac{r}{a})}{j_{0n}^2 |J_1(j_{0n})|^2} \left[\frac{2}{j_{0n}r_b/a} J_1(j_{0n}\frac{r_b}{a}) - J_0(j_{0n}\frac{r_b}{a}) \right] \\
&\quad \times \int_{-\infty}^t dt' \frac{\partial}{\partial z} \left[J_0(j_{0n}\frac{\lambda_-}{a}) \Theta(\lambda_-^2) - J_0(j_{0n}\frac{\lambda_+}{a}) \Theta(\lambda_+^2) \right].
\end{aligned} \tag{A.10}$$

Using the chain rule and the relation, $dJ_0/dx = -J_1(x)$,

$$\begin{aligned} \frac{\partial}{\partial z} \left[J_0 \left(j_{0n} \frac{\lambda_{\pm}}{a} \right) \Theta(\lambda_{\pm}^2) \right] &= \frac{\partial \lambda_{\pm}}{\partial z} \frac{\partial}{\partial \lambda_{\pm}} \left[J_0 \left(j_{0n} \frac{\lambda_{\pm}}{a} \right) \Theta(\lambda_{\pm}^2) \right] \\ &= \frac{\partial \lambda_{\pm}}{\partial z} \left[-\frac{j_{0n}}{a} J_1 \left(j_{0n} \frac{\lambda_{\pm}}{a} \right) \Theta(\lambda_{\pm}^2) \right. \\ &\quad \left. + J_0 \left(j_{0n} \frac{\lambda_{\pm}}{a} \right) \delta(\lambda_{\pm}^2) 2\lambda_{\pm} \right], \end{aligned} \quad (\text{A.11})$$

where

$$\begin{aligned} \frac{\partial \lambda_{\pm}}{\partial z} &= \frac{\partial}{\partial z} \left\{ c^2 (t - t')^2 - [z \pm z''(t')]^2 \right\}^{1/2} \\ &= -\frac{2 [z \pm z''(t')]}{2 \{ c^2 (t - t')^2 - [z \pm z''(t')]^2 \}^{1/2}} = -\frac{[z \pm z''(t')]}{\lambda_{\pm}}. \end{aligned} \quad (\text{A.12})$$

Therefore,

$$\begin{aligned} -\frac{\partial \phi}{\partial z} &= -\frac{4cQ}{\pi \epsilon_0 r_b^2} \sum_{n=0}^{\infty} \frac{J_0(j_{0n} \frac{r}{a})}{j_{0n}^2 |J_1(j_{0n})|^2} \left[\frac{2}{j_{0n} \frac{r_b}{a}} J_1 \left(j_{0n} \frac{r_b}{a} \right) - J_0 \left(j_{0n} \frac{r_b}{a} \right) \right] \\ &\quad \times \int_{-\infty}^t dt' \left\{ [z - z''(t')] \left[-\frac{j_{0n}}{a \lambda_-} J_1 \left(j_{0n} \frac{\lambda_-}{a} \right) \Theta(\lambda_-^2) + 2J_0 \left(j_{0n} \frac{\lambda_-}{a} \right) \delta(\lambda_-^2) \right] \right. \\ &\quad \left. - [z + z''(t')] \left[-\frac{j_{0n}}{a \lambda_+} J_1 \left(j_{0n} \frac{\lambda_+}{a} \right) \Theta(\lambda_+^2) + 2J_0 \left(j_{0n} \frac{\lambda_+}{a} \right) \delta(\lambda_+^2) \right] \right\} \\ &= \frac{4Q}{\pi \epsilon_0 \hat{r}_b^2 a^2} \sum_{n=0}^{\infty} \frac{J_0(j_{0n} \hat{r})}{j_{0n}^2 |J_1(j_{0n})|^2} \left[\frac{2}{j_{0n} \hat{r}_b} J_1(j_{0n} \hat{r}_b) - J_0(j_{0n} \hat{r}_b) \right] \\ &\quad \times \int_{-\infty}^{\tau} d\tau' \left\{ [\hat{z} - \hat{z}''(\tau')] \left[-\frac{j_{0n}}{\hat{\lambda}_-} J_1(j_{0n} \hat{\lambda}_-) \Theta(\hat{\lambda}_-^2) + 2a^2 J_0(j_{0n} \hat{\lambda}_-) \delta(\hat{\lambda}_-^2) \right] \right. \\ &\quad \left. - [\hat{z} + \hat{z}''(\tau')] \left[-\frac{j_{0n}}{\hat{\lambda}_+} J_1(j_{0n} \hat{\lambda}_+) \Theta(\hat{\lambda}_+^2) + 2a^2 J_0(j_{0n} \hat{\lambda}_+) \delta(\hat{\lambda}_+^2) \right] \right\}. \end{aligned} \quad (\text{A.13})$$

$$\text{II} \quad -\frac{\partial A_z}{\partial t}$$

For this calculation, one needs to be careful since both the range of integration and integrands depend on the variable t .

$$\begin{aligned} -\frac{\partial A_z}{\partial t} &= -\frac{4cQ\mu_0}{\pi r_b^2} \sum_{n=0}^{\infty} \frac{J_0(j_{0n} \frac{r}{a})}{j_{0n}^2 |J_1(j_{0n})|^2} \left[\frac{2}{j_{0n} \frac{r_b}{a}} J_1(j_{0n} \frac{r_b}{a}) - J_0(j_{0n} \frac{r_b}{a}) \right] \\ &\quad \times \frac{\partial}{\partial t} \int_{-\infty}^t dt' \left[J_0(j_{0n} \frac{\lambda_-}{a}) \Theta(\lambda_-^2) + J_0(j_{0n} \frac{\lambda_+}{a}) \Theta(\lambda_+^2) \right] \left[\frac{dz''(t)}{dt} \right]_{t=t'}. \end{aligned} \quad (\text{A.14})$$

It is helpful to use the relation,

$$\frac{\partial}{\partial t} \int_{-\infty}^t dt' f(t, t') = f(t, t) + \int_{-\infty}^t dt' \frac{\partial}{\partial t} f(t, t'). \quad (\text{A.15})$$

Hence,

$$\begin{aligned} &\frac{\partial}{\partial t} \int_{-\infty}^t dt' \left[J_0(j_{0n} \frac{\lambda_{\pm}}{a}) \Theta(\lambda_{\pm}^2) \right] \left[\frac{dz''(t)}{dt} \right]_{t=t'} \\ &= \left[J_0(j_{0n} \frac{\lambda_{\pm}}{a}) \Theta(\lambda_{\pm}^2) \left[\frac{dz''(t)}{dt} \right]_{t=t'} \right]_{t'=t} \\ &\quad + \int_{-\infty}^t dt' \frac{\partial}{\partial t} \left[J_0(j_{0n} \frac{\lambda_{\pm}}{a}) \Theta(\lambda_{\pm}^2) \right] \left[\frac{dz''(t)}{dt} \right]_{t=t'} \\ &= \int_{-\infty}^t dt' \frac{\partial}{\partial t} \left[J_0(j_{0n} \frac{\lambda_{\pm}}{a}) \Theta(\lambda_{\pm}^2) \right] \left[\frac{dz''(t)}{dt} \right]_{t=t'}, \end{aligned} \quad (\text{A.16})$$

Using the chain rule and the property of the Bessel function,

$$\begin{aligned} \frac{\partial}{\partial t} \left[J_0(j_{0n} \frac{\lambda_{\pm}}{a}) \Theta(\lambda_{\pm}^2) \right] &= \frac{\partial \lambda_{\pm}}{\partial t} \frac{\partial}{\partial \lambda_{\pm}} \left[J_0(j_{0n} \frac{\lambda_{\pm}}{a}) \Theta(\lambda_{\pm}^2) \right] \\ &= \frac{\partial \lambda_{\pm}}{\partial t} \left[-\frac{j_{0n}}{a} J_1(j_{0n} \frac{\lambda_{\pm}}{a}) \Theta(\lambda_{\pm}^2) + J_0(j_{0n} \frac{\lambda_{\pm}}{a}) \delta(\lambda_{\pm}^2) 2\lambda_{\pm} \right], \end{aligned} \quad (\text{A.17})$$

where

$$\begin{aligned} \frac{\partial \lambda_{\pm}}{\partial t} &= \frac{\partial}{\partial t} \left\{ c^2 (t - t')^2 - [z \pm z''(t')]^2 \right\}^{1/2} \\ &= \frac{2c^2 (t - t')}{2 \left\{ c^2 (t - t')^2 - [z \pm z''(t')]^2 \right\}^{1/2}} = \frac{c^2 (t - t')}{\lambda_{\pm}}. \end{aligned} \quad (\text{A.18})$$

Therefore,

$$\begin{aligned}
-\frac{\partial A_z}{\partial t} &= -\frac{4cQ\mu_0}{\pi r_b^2} \sum_{n=0}^{\infty} \frac{J_0(j_{0n} \frac{r}{a})}{j_{0n}^2 |J_1(j_{0n})|^2} \left[\frac{2}{j_{0n} \frac{r_b}{a}} J_1(j_{0n} \frac{r_b}{a}) - J_0(j_{0n} \frac{r_b}{a}) \right] \\
&\quad \times \int_{-\infty}^t dt' c^2(t-t') \left\{ \left[\frac{j_{0n}}{\hat{\lambda}_-} J_1(j_{0n} \hat{\lambda}_-) \Theta(\hat{\lambda}_-^2) + 2a^2 J_0(j_{0n} \hat{\lambda}_-) \delta(\hat{\lambda}_-^2) \right] \right. \\
&\quad \left. + \left[\frac{j_{0n}}{\hat{\lambda}_+} J_1(j_{0n} \hat{\lambda}_+) \Theta(\hat{\lambda}_+^2) + 2a^2 J_0(j_{0n} \hat{\lambda}_+) \delta(\hat{\lambda}_+^2) \right] \right\} \left[\frac{dz''(t)}{dt} \right]_{t=t'} \\
&= \frac{4c^2Q\mu_0}{\pi \hat{r}_b^2 a^2} \sum_{n=0}^{\infty} \frac{J_0(j_{0n} \hat{r})}{j_{0n}^2 |J_1(j_{0n})|^2} \left[\frac{2}{j_{0n} \hat{r}_b} J_1(j_{0n} \hat{r}_b) - J_0(j_{0n} \hat{r}_b) \right] \\
&\quad \times \int_{-\infty}^{\tau} d\tau' (\tau - \tau') \left\{ \left[\frac{j_{0n}}{\hat{\lambda}_-} J_1(j_{0n} \hat{\lambda}_-) \Theta(\hat{\lambda}_-^2) - 2a^2 J_0(j_{0n} \hat{\lambda}_-) \delta(\hat{\lambda}_-^2) \right] \right. \\
&\quad \left. + \left[\frac{j_{0n}}{\hat{\lambda}_+} J_1(j_{0n} \hat{\lambda}_+) \Theta(\hat{\lambda}_+^2) - 2a^2 J_0(j_{0n} \hat{\lambda}_+) \delta(\hat{\lambda}_+^2) \right] \right\} \left[\frac{d\hat{z}''(\tau)}{d\tau} \right]_{\tau=\tau'}.
\end{aligned} \tag{A.19}$$

A.3.2 Analytic form of E_z

Finally, using Eqns. (A.13) and (A.19), the longitudinal electric field is given by

$$\begin{aligned}
E_z(r, z, t) = & \frac{4Q}{\pi\epsilon_0\hat{r}_b^2a^2} \sum_{n=0}^{\infty} \frac{J_0(j_{0n}\hat{r})}{j_{0n}^2|J_1(j_{0n})|^2} \left[\frac{2}{j_{0n}\hat{r}_b} J_1(j_{0n}\hat{r}_b) - J_0(j_{0n}\hat{r}_b) \right] \\
& \times \int_{-\infty}^{\tau} d\tau' \left\{ [\hat{z} - \hat{z}''(\tau')] \left[-\frac{j_{0n}}{\hat{\lambda}_-} J_1(j_{0n}\hat{\lambda}_-) \Theta(\hat{\lambda}_-^2) + 2a^2 J_0(j_{0n}\hat{\lambda}_-) \delta(\hat{\lambda}_-^2) \right] \right. \\
& \left. - [\hat{z} + \hat{z}''(\tau')] \left[-\frac{j_{0n}}{\hat{\lambda}_+} J_1(j_{0n}\hat{\lambda}_+) \Theta(\hat{\lambda}_+^2) + 2a^2 J_0(j_{0n}\hat{\lambda}_+) \delta(\hat{\lambda}_+^2) \right] \right\} \\
& + \frac{4c^2Q\mu_0}{\pi\hat{r}_b^2a^2} \sum_{n=0}^{\infty} \frac{J_0(j_{0n}\hat{r})}{j_{0n}^2|J_1(j_{0n})|^2} \left[\frac{2}{j_{0n}\hat{r}_b} J_1(j_{0n}\hat{r}_b) - J_0(j_{0n}\hat{r}_b) \right] \\
& \times \int_{-\infty}^{\tau} d\tau' (\tau - \tau') \left\{ \left[\frac{j_{0n}}{\hat{\lambda}_-} J_1(j_{0n}\hat{\lambda}_-) \Theta(\hat{\lambda}_-^2) - 2a^2 J_0(j_{0n}\hat{\lambda}_-) \delta(\hat{\lambda}_-^2) \right] \right. \\
& \left. + \left[\frac{j_{0n}}{\hat{\lambda}_+} J_1(j_{0n}\hat{\lambda}_+) \Theta(\hat{\lambda}_+^2) - 2a^2 J_0(j_{0n}\hat{\lambda}_+) \delta(\hat{\lambda}_+^2) \right] \right\} \left[\frac{d\hat{z}''(\tau)}{d\tau} \right]_{\tau=\tau'} \\
= & \frac{4Q}{\pi\epsilon_0\hat{r}_b^2a^2} \sum_{n=0}^{\infty} \frac{J_0(j_{0n}\hat{r})}{j_{0n}^2|J_1(j_{0n})|^2} \left[\frac{2}{j_{0n}\hat{r}_b} J_1(j_{0n}\hat{r}_b) - J_0(j_{0n}\hat{r}_b) \right] \\
& \times \int_{-\infty}^{\tau} d\tau' \left\{ \left\{ [\hat{z} - \hat{z}''(\tau')] - (\tau - \tau') \left[\frac{d\hat{z}''(\tau)}{d\tau} \right]_{\tau=\tau'} \right\} \right. \\
& \times \left[-\frac{j_{0n}}{\hat{\lambda}_-} J_1(j_{0n}\hat{\lambda}_-) \Theta(\hat{\lambda}_-^2) + 2a^2 J_0(j_{0n}\hat{\lambda}_-) \delta(\hat{\lambda}_-^2) \right] \\
& - \left\{ [\hat{z} + \hat{z}''(\tau')] + (\tau - \tau') \left[\frac{d\hat{z}''(\tau)}{d\tau} \right]_{\tau=\tau'} \right\} \\
& \left. \times \left[-\frac{j_{0n}}{\hat{\lambda}_+} J_1(j_{0n}\hat{\lambda}_+) \Theta(\hat{\lambda}_+^2) + 2a^2 J_0(j_{0n}\hat{\lambda}_+) \delta(\hat{\lambda}_+^2) \right] \right\}.
\end{aligned}
\tag{A.20}$$

Appendix B

Electrostatic Space-Charge Fields

B.1 Electrostatic Space-Charge Fields with Delta-Function Source

Using the Green's function, the electrostatic space-charge potential of the real charge disk in the beam rest frame can be calculated as (See p143 in Jackson):

$$\phi(r, z) = \frac{1}{\epsilon_0} \int d^3 r' G_\phi(\mathbf{r}; \mathbf{r}') \rho(\mathbf{r}'), \quad (\text{B.1})$$

where

$$G_\phi(\mathbf{r}; \mathbf{r}') = \frac{1}{2} \sum_{mn} \frac{\psi_{mn}(\mathbf{r}_\perp) \psi_{mn}^*(\mathbf{r}'_\perp)}{k_{\perp mn}} \exp \left[-\frac{j_{0n}}{a} |z - z'| \right], \quad (\text{B.2a})$$

$$\psi_{mn}(\mathbf{r}_\perp) = \frac{1}{a\sqrt{\pi}} \frac{J_m(j_{mn}r/a) e^{im\theta}}{|J_{m+1}(j_{mn})|}, \quad (\text{B.2b})$$

and

$$\rho(\mathbf{r}) = \frac{2Q}{\pi r_b^2} \theta(r_b - r) \left(1 - \frac{r^2}{r_b^2} \right) \delta(z - z_0). \quad (\text{B.2c})$$

As seen in $\rho(\mathbf{r})$, a disk beam is located at $z = z_0$, and the beam motion is stationary. Since the image disk is located at $z = -z_0$, the scalar potential is given by the

superposition of potentials of real and image disks:

$$\begin{aligned} \phi(\mathbf{r}, t) = & \frac{4Qa}{\pi\epsilon_0 r_b^2} \sum_n \frac{J_0(j_{0n}r/a)}{j_{0n}^3 |J_1(j_{0n})|^2} \left[\frac{2}{j_{0n} \frac{r_b}{a}} J_1\left(j_{0n} \frac{r_b}{a}\right) - J_0\left(j_{0n} \frac{r_b}{a}\right) \right] \\ & \times \left\{ \exp\left[-\frac{j_{0n}}{a} |z - z_0|\right] - \exp\left[-\frac{j_{0n}}{a} |z + z_0|\right] \right\}. \end{aligned} \quad (\text{B.3})$$

Since the beam is at rest in this frame, the vector potential A_z is zero.

The scalar and vector potentials in the laboratory frame can be calculated with the Lorentz transformations, as

$$\phi' = \gamma(\phi + c\beta \cdot \mathbf{A}), \quad (\text{B.4a})$$

$$A'_z = \gamma\left(A_z + \frac{\beta}{c}\phi\right), \quad (\text{B.4b})$$

where unprimed potentials are in the rest frame, and primed potentials are in the lab frame. From these potentials, the electrostatic space-charge fields in the accelerating frame can be derived, i.e.,

$$\begin{aligned} E'_r = \gamma E_r = & -\gamma \frac{\partial \phi}{\partial r} \\ = & \frac{4Q\gamma}{\pi\epsilon_0 r_b^2} \sum_n \frac{J_1(j_{0n}r/a)}{j_{0n}^2 |J_1(j_{0n})|^2} \left[\frac{2}{j_{0n} \frac{r_b}{a}} J_1\left(j_{0n} \frac{r_b}{a}\right) - J_0\left(j_{0n} \frac{r_b}{a}\right) \right] \\ & \times \left\{ \exp\left[-\frac{j_{0n}}{a} \gamma |z - z_0|\right] - \exp\left[-\frac{j_{0n}}{a} \gamma |z + z_0|\right] \right\}. \end{aligned} \quad (\text{B.5a})$$

and

$$\begin{aligned} B'_\theta = & \frac{\beta\gamma}{c} E_r = \frac{\beta}{c} E_r \\ = & \frac{1}{c} [\beta_{\text{real}} E_{r,\text{real}} + \beta_{\text{image}} E_{r,\text{image}}] \\ = & \frac{4cQ\mu_0\beta\gamma}{\pi r_b^2} \sum_n \frac{J_1(j_{0n}r/a)}{j_{0n}^2 |J_1(j_{0n})|^2} \left[\frac{2}{j_{0n} \frac{r_b}{a}} J_1\left(j_{0n} \frac{r_b}{a}\right) - J_0\left(j_{0n} \frac{r_b}{a}\right) \right] \\ & \times \left\{ \exp\left[-\frac{j_{0n}}{a} \gamma |z - z_0|\right] + \exp\left[-\frac{j_{0n}}{a} \gamma |z + z_0|\right] \right\}. \end{aligned} \quad (\text{B.5b})$$

The γ factor in front of z is for the Lorentz transformation of z -direction. In the B'_θ calculation, the image disk is moving in the opposite direction, hence, its β has

the opposite sign. We assumed that the beam is moving only in the z -direction, i.e., $\partial\beta/\partial\mathbf{r}_\perp = 0$. Hence, $\partial\gamma/\partial r = 0$, but $\partial\gamma/\partial z \neq 0$. The Lorentz transformation of the fields (See p558 in Jackson) are

$$\mathbf{E}' = \gamma(\mathbf{E} + \beta \times \mathbf{B}) - \frac{\gamma^2}{\gamma + 1} \beta(\beta \cdot \mathbf{E}), \quad (\text{B.6a})$$

and

$$\mathbf{B}' = \gamma(\mathbf{B} - \beta \times \mathbf{E}) - \frac{\gamma^2}{\gamma + 1} \beta(\beta \cdot \mathbf{B}). \quad (\text{B.6b})$$

Therefore,

$$E'_r = \gamma(E_r - c\beta B_\theta), \quad (\text{B.7a})$$

$$B'_\theta = \gamma\left(B_\theta - \frac{\beta}{c}E_r\right), \quad (\text{B.7b})$$

and

$$E'_z = E_z, \quad (\text{B.7c})$$

and E_z is not changed during the transformation:

$$E'_z = \frac{4Q}{\pi\epsilon_0 r_b^2} \sum_n \frac{J_0(j_{0n}r/a)}{j_{0n}^2 |J_1(j_{0n})|^2} \left[\frac{2}{j_{0n} \frac{r_b}{a}} J_1\left(j_{0n} \frac{r_b}{a}\right) - J_0\left(j_{0n} \frac{r_b}{a}\right) \right] \\ \times \begin{cases} \left\{ \exp\left[-\frac{j_{0n}}{a}\gamma|z - z_0|\right] - \exp\left[-\frac{j_{0n}}{a}\gamma|z + z_0|\right] \right\} & \text{for } z \geq 0 \\ \left\{ -\exp\left[-\frac{j_{0n}}{a}\gamma|z_0 - z|\right] - \exp\left[-\frac{j_{0n}}{a}\gamma|z + z_0|\right] \right\} & \text{for } z < 0 \end{cases}. \quad (\text{B.8})$$

B.2 Electrostatic Fields with a Constant J_z

In this section, we assume that the bunch has a finite size, i.e., it is not broken up into a number of slices, and the current density is constant through the bunch. This is helpful for forming an analytical electrostatic result. Then, the charge density is given by

$$\rho(\mathbf{r}) = \frac{Q}{\pi r_b^2 \sqrt{z_2 - z_1}} \left(1 - \frac{r^2}{r_b^2}\right) \Theta(r_b - r) \left[\Theta(z - z_1) - \Theta(z - z_2)\right], \quad (\text{B.9})$$

where Q is the total bunch charge, r_b is the beam radius, and z_1 and z_2 are the locations of the tail and head of the bunch at a specific time, respectively. Using Eqns. (B.1), (B.2), and (B.9), the scalar potential is computed as

$$\begin{aligned}
 \phi(\mathbf{r}) &= \frac{Q}{\pi\epsilon_0 a r_b^2} \frac{1}{\sqrt{z_b}} \sum_n \frac{J_0(j_{0n}r/a)}{j_{0n}J_1^2(j_{0n})} \\
 &\quad \times \int_0^{z_b} dz' \frac{1}{\sqrt{z'}} \exp\left[-\frac{j_{0n}}{a}|z-z'|\right] \int_0^{r_b} dr' r' \left(1 - \frac{r'^2}{r_b^2}\right) J_0\left(j_{0n}\frac{r'}{a}\right) \\
 &= \frac{2aQ}{\pi\epsilon_0 r_b^2} \sum_n \sqrt{\frac{\pi}{j_{0n}z_b/a}} \frac{J_0(j_{0n}r/a)}{j_{0n}^3 J_1^2(j_{0n})} \left[\frac{2}{j_{0n}r_b/a} J_1\left(j_{0n}\frac{r_b}{a}\right) - J_0\left(j_{0n}\frac{r_b}{a}\right) \right] e^{-\frac{j_{0n}}{a}z} \\
 &\quad \times \begin{cases} \text{Erfi}\left(\sqrt{\frac{j_{0n}}{a}}z_b\right) \\ \left\{ \text{Erfi}\left(\sqrt{\frac{j_{0n}}{a}}z\right) + e^{2\frac{j_{0n}}{a}z} \left[\text{Erf}\left(\sqrt{\frac{j_{0n}}{a}}z\right) - \text{Erf}\left(\sqrt{\frac{j_{0n}}{a}}z_b\right) \right] \right\} \end{cases},
 \end{aligned} \tag{B.10}$$

for $z_1 = 0$ and $z_2 = z_b$. In Eqn. (B.10), a is the cavity radius, $\text{Erf}(z)$ is the error function, and $\text{Erfi}(z)$ are the imaginary error function. The error functions are defined by

$$\text{Erf}(z) = \frac{2}{\sqrt{\pi}} \int_0^z dt e^{-t^2}, \tag{B.11a}$$

and

$$\text{Erfi}(z) = -i\text{Erf}(iz), \tag{B.11b}$$

where $i = \sqrt{-1}$.

In order to include the image charge effect due to the cathode, the potential with the additional bunch with the opposite charge in the negative z -direction will be added such that,

$$\phi_{\text{total}} = \phi_{\text{real}} + \phi_{\text{image}}. \tag{B.12}$$

Since the longitudinal electrostatic space-charge field is invariant during the Lorentz

transformation, $E'_z = E_{z,\text{rest}} = -\partial\phi/\partial z$ in the laboratory frame and is given by

$$E'_z = \frac{2Q}{\pi\epsilon_0 r_b^2} \sum_n \sqrt{\frac{\pi}{j_{0n} z_b/a} \frac{J_0(j_{0n} r/a)}{j_{0n}^2 J_1^2(j_{0n})}} \left[\frac{2}{j_{0n} r_b/a} J_1\left(j_{0n} \frac{r_b}{a}\right) - J_0\left(j_{0n} \frac{r_b}{a}\right) \right] e^{-\frac{j_{0n}}{a} z} \times \begin{cases} \left\{ \left[\text{Erfi}\left(\sqrt{\frac{j_{0n}}{a}} z_2\right) - \text{Erfi}\left(\sqrt{\frac{j_{0n}}{a}} z_1\right) \right] - \left[\text{Erf}\left(\sqrt{\frac{j_{0n}}{a}} z_2\right) - \text{Erf}\left(\sqrt{\frac{j_{0n}}{a}} z_1\right) \right] \right\} & \text{for } z > z_2 \\ \left\{ \left[\text{Erfi}\left(\sqrt{\frac{j_{0n}}{a}} z\right) - \text{Erfi}\left(\sqrt{\frac{j_{0n}}{a}} z_1\right) \right] - \left[\text{Erf}\left(\sqrt{\frac{j_{0n}}{a}} z_2\right) - \text{Erf}\left(\sqrt{\frac{j_{0n}}{a}} z_1\right) \right] - \exp\left(2\frac{j_{0n}}{a} z\right) \left[\text{Erf}\left(\sqrt{\frac{j_{0n}}{a}} z_2\right) - \text{Erf}\left(\sqrt{\frac{j_{0n}}{a}} z\right) \right] \right\} & \text{for } z_1 < z < z_2 \\ \left[-1 - \exp\left(2\frac{j_{0n}}{a} z\right) \right] \left[\text{Erf}\left(\sqrt{\frac{j_{0n}}{a}} z_2\right) - \text{Erf}\left(\sqrt{\frac{j_{0n}}{a}} z_1\right) \right] & \text{for } z < z_1 \end{cases} \quad (\text{B.13})$$

B.3 Electrostatic Spacecharge Fields with the finite size bunch length

In this section, the bunch has a finite length in the longitudinal direction as

$$\rho_m(z, t) = \frac{8Q}{\pi a^2 L} \frac{a^2}{r_b^2} \frac{1}{j_{0m}^2 J_1^2(j_{0m})} \left[\frac{2}{j_{0m} r_b/a} J_1\left(j_{0m} \frac{r_b}{a}\right) - J_0\left(j_{0m} \frac{r_b}{a}\right) \right] \times \left[\Theta\left(z + \frac{L}{2}\right) - \Theta\left(z - \frac{L}{2}\right) \right]. \quad (\text{B.14})$$

Then, the electrostatic potential is given by:

$$\phi = \frac{4aQ}{\pi\epsilon_0 r_0 L} \sum_m \frac{J_0(j_{0m} r/a)}{j_{0m}^3 J_1^2(j_{0m})} \frac{a^2}{r_0^2} \left[\frac{2}{j_{0m} r_0/a} J_1\left(j_{0m} \frac{r_0}{a}\right) - J_0\left(j_{0m} \frac{r_0}{a}\right) \right] \times \begin{cases} \left[-e^{-\frac{j_{0m}}{a}(z+\frac{L}{2})} + e^{-\frac{j_{0m}}{a}(z-\frac{L}{2})} \right] & \text{for } z > \frac{L}{2} \\ \left[2 - e^{-\frac{j_{0m}}{a}(z+\frac{L}{2})} - e^{\frac{j_{0m}}{a}(z-\frac{L}{2})} \right] & \text{for } |z| \leq \frac{L}{2} \\ \left[e^{\frac{j_{0m}}{a}(z+\frac{L}{2})} - e^{\frac{j_{0m}}{a}(z-\frac{L}{2})} \right] & \text{for } z < -\frac{L}{2} \end{cases} \quad (\text{B.15})$$

From the electrostatic potential,

$$E_z = -\frac{\partial\phi}{\partial z} = -\frac{Q}{\pi\epsilon_0 a L} \sum_m \frac{a}{r_0} \frac{J_0(j_{0m}r/a)}{j_{0m}^2 J_1^2(j_{0m})} \frac{a^2}{r_0^2} \left[\frac{2}{j_{0m}r_0/a} J_1\left(j_{0m}\frac{r_0}{a}\right) - J_0\left(j_{0m}\frac{r_0}{a}\right) \right] \\ \times \begin{cases} \left[e^{-\frac{j_{0m}}{a}(z+\frac{L}{2})} - e^{-\frac{j_{0m}}{a}(z-\frac{L}{2})} \right] & \text{for } z > \frac{L}{2} \\ \left[e^{-\frac{j_{0m}}{a}(z+\frac{L}{2})} - e^{\frac{j_{0m}}{a}(z-\frac{L}{2})} \right] & \text{for } |z| \leq \frac{L}{2} \\ \left[e^{\frac{j_{0m}}{a}(z+\frac{L}{2})} - e^{\frac{j_{0m}}{a}(z-\frac{L}{2})} \right] & \text{for } z < -\frac{L}{2} \end{cases} . \quad (\text{B.16})$$

Bibliography

- [1] L.R. Elias *et al*, “Observation of Stimulated Emission of Radiation by Relativistic Electrons in a Spatially Periodic Transverse Magnetic Field,” *Phys. Rev. Lett.* **36** 717 (1976).
- [2] M. Dohlus, P. Schmüser and J. Rossbach, “Introduction to Ultraviolet and X-Ray Free Electron Lasers, (Springer, 2008).”
- [3] P. Oddone, in *Proc. UCLA Workshop: Linear Collider $B\bar{B}$ Factory Conceptual Design*.
- [4] J. Bagger *et al*, “The Case for a 500 GeV e^+e^- Linear Collider,” Chap. 2 in *Linear Collider Physics Resource Book for Snowmass 2001*
- [5] K.-J. Kim *et al*, “Synchrotron Radiation and Free Electron Lasers,” *USPAS Lecture Notes*, unpublished.
- [6] S.Y. Lee, “Accelerator Physics, 2nd ed. (World Scientific, 2006).”
- [7] S. Schreiber, “Performance of the TTF Photoinjector for FEL Operation,” *Proc. of the workshop, “The Physics and Applications of High Brightness Electron Beams,”* 2002.
- [8] K.-J. Kim, “High-Brightness Electron Beam for X-Ray FELs,” in *proceedings of COOL’03*.

- [9] U.S. Linear Collider Technology Options Study, Mar. 1, 2004. A summary may be found at <http://www.interactions.org/pdf/ITRPexec.pdf>
- [10] R.L. Sheffield *et al*, “The Los Alamos Photoinjector Program,” Nucl. Instr. Meth. A **226** (1988) 272.
- [11] K.-J. Kim, “RF and Space-Charge Effects in Laser-Driven RF Electron Guns,” Nucl. Instr. and Meth. A **275** (1989) 201.
- [12] B.E. Carlsten, “New photoelectric injector design for the Los Alamos National Laboratory XUV FEL accelerator,” Nucl. Instr. and Meth. A **285** (1989) 313.
- [13] I.M. Kapchinsky , “ Limitations of Proton Beam Current in a Strong Focusing Linear Accelerator Associated with the Beam Space Charge,” in Proc. of the Conference on High Energy Accelerators and Instrumentations, (1959).
- [14] F.J. Sacherer, “Transverse Space-Charge Effects in Circular Accelerators,” Ph.D. Thesis (1968).
- [15] L. Serafini *et al*, “Envelope Analysis of Intense Relativistic Quasilaminar Beams in RF Photoinjectors: A Theory of Emittance Compensation,” Phys. Rev. E **55** (6) 7565, 1997.
- [16] L.M. Young (documentation by J.H. Billen), “PARMELA”, report LA-UR-96-1835, Los Alamos, 1996 (rev. 2004).
- [17] L. Gianessi *et al*, “TREDI: Fully 3D Beam Dynamics Simulation of RF Guns, Bendings and FELs,” Nucl. Instr. Meth. A **436** (1999) 443
- [18] L. Fröhlich, “ASTRA user guide”, 2008.
- [19] MAFIA, Computer Simulation Technology, GmbH (Darmstadt, Germany), <http://www.cst.de>

- [20] I. Zagorodnov *et al*, “TE/TM Field Solver for Particle Beam Simulations without Numerical Cherenkov Radiation,” *Phys. Rev. ST Accel. Beams* **8**, 042001 (2005)
- [21] M. Hess *et al*, “A Green’s Function Based Space-Charge Field Solver for Electron Source Simulations,” *Phys. Rev. ST Accel. Beams* **10**, 054201 (2007)
- [22] E. Colby *et al*, “Simulation Issues for RF Photoinjectors” in ICAP’02 proceedings.
- [23] A. Candel *et al*, “Parallel Higher-Order Finite Element Method for Accurate Field Computations in Wakefield and PIC Simulations” in ICAP’06 proceedings.
- [24] J.-M Dolique and M. Coacolo, “Relativistic Acceleration and Retardation Effects on Photoemission of Intense Electron Short Pulses” in PAC’91 proceedings.
- [25] W. Salah *et al*, “Theoretical Approach of the Photoinjector Exit Aperture Influence on the Wake Field Driven by an Electron Beam Accelerated in an RF Gun of Free-Electron Laser ELSA,” *Nucl. Instr. Meth. A* **447** (2000) 309.
- [26] W. Salah, “Analytical and Numerical Investigations of the Evolution of Wake Fields of Accelerated Electron Beams Encountering Cavity Discontinuities in Laser-Driven RF Free-Electron Laser Photoinjector,” *Nucl. Instr. Meth. A* **533** (2004) 248.
- [27] P. Schoessow *et al*, “The Argonne Wakefield Accelerator Overview and Status”, in PAC’03 proceedings.
- [28] K.S Yee, “Numerical Solution of Initial Boundary Value Problems involving Maxwell’s Equations in Isotropic Media,” *IEEE Trans. Antennas Propagat.* **14** 302 (1966).

- [29] K.R. Crandall (unpublished); a description of SCHEFF may be found in T. P. Wangler, RF Linear Accelerators (Wile, 2nd ed. 1998), pp. 270272.
- [30] J. Qiang *et al*, “High-Resolution Parallel Particle-In-Cell Simulations of Beam Dynamics in the Spallation Neutron Source Linac,” Nucl. Instr. Meth. A **457** (2001) 1.
- [31] B.E.C. Koltenbah *et al*, “Space Charge Calculations of Elliptical Cross-Section Electron Pulses in PARMELA,” Nucl. Instr. and Meth. A **429** (1999) 281.
- [32] P. Lapostolle *et al*, “A Modified Space Charge Routine for High Intensity Bunched Beams,” Nucl. Instr. Meth. A **379** (1996) 21.
- [33] Los Alamos Accelerator Code Group, “Reference Manual for the POISSON/SUPERFISH Group of Codes,” Los Alamos National Laboratory document LA-UR-87-126.
- [34] J.D. Jackson, “Classical Electrodynamics, 3rd ed. (Wiley, 1989).”
- [35] M.N.O Sadiku, “Numerical Techniques in Electromagnetics, 2nd ed. (CRC, 2000).”
- [36] S. Humphries, Jr. “Field Solutions on Computers (CRC, 1997).”
- [37] G. Barton, “Elements of Green’s Functions and Propagations: Potentials, Diffusion, and Waves (Oxford Univ. Press, New York, 1989).”
- [38] I.S. Gradshteyn and I.M. Ryzhik, “Table of Integrals, Series, and Products, 6th ed. (Academic London, 2000).”
- [39] T.P. Wangler, “RF Linear Accelerators, 2nd ed (Wiley-VCH, 2008).”

- [40] K. Batchelor *et al*, “Development of a High Brightness Electron Gun for the Accelerator Test Facility at Brookhaven National Laboratory,” in EPAC’88 proceedings.
- [41] H.A. Bethe, “Theory of Diffraction by Small Holes,” *Phys. Rev.* **66** 163 (1944).
- [42] M. Hess *et al*, “Advanced Electromagnetic Analysis of Electron Source Geometries,” in PAC’05 proceedings.
- [43] M. Hess *et al*, “A Multislice Approach for Electromagnetic Green’s Function Based Beam Simulations,” in PAC’07 proceedings.
- [44] C.S. Park *et al*, “Computational Requirements for Green’s Function Based Photocathode Source Simulations,” in PAC’07 proceedings.
- [45] C.S. Park *et al*, “Time-Retardation Effect Causing Beamloss in the RF Photoinjector,” in PAC’09 proceedings.
- [46] C.S. Park *et al*, “The Effects of Electromagnetic Space-Charge Fields in RF Photocathode Guns,” submitted to *Nucl. Instr. Meth. A*.
- [47] MicroWave Studio, Computer Simulation Technology, Germany, <http://www.cst.de>
- [48] CERN Program Library, <http://cernlib.web.cern.ch/cernlib/>
- [49] Z.M. Yusof *et al*, “Schottky-Enabled Photoemission in a rf Accelerator Photoinjector: Possible Generation of Ultralow Transverse Thermal-Emittance Electron Beam,” *Phys. Rev. Lett.* **93** 114801 (2004).
- [50] M. Hess *et al*, “Exact Space-Charge Field Solutions for Cylindrically Symmetric Beam Currents in a Circular Conductor Pipe,” submitted to *Phys. Rev. ST Accel. Beams*

-
- [51] G.N. Watson, “A Treatise on the Theory of Bessel Functions, 2nd ed. (Cambridge Univ. Press, 1966).”

CURRICULUM VITAE

Chong Shik Park

Indiana University Cyclotron Facility
Milo B. Sampson Ln. Bloomington, IN 47408
Tel: 812-855-5189 (Office)
Email: *chspark@indiana.edu*

Education

DEGREE	MAJOR	INSTITUTION
Ph.D. (08/2009, expected)	Accelerator Physics	Indiana University
B.S. (02/2003)	Physics	Korea University, South Korea

Fellowships

- PAC'09 Student Travel Grant
- Out Standing Student Award, Second International Accelerator School for Linear Colliders, Erice, Italy
- PAC'07 Student Travel Grant
- National Atomic Energy Scholarship, from Ministry of Science and Technology of Korea, 12/2004 - 12/2006

Professional Experience

- Indiana University Cyclotron Facility, Research Associate, 01/2005 - Present
- Indiana University, Bloomington, Associate Instructor, 08/2007 - 12/2007
- Korea Institute of Radiological And Medical Sciences (KIRAMS), Research Assistant, 12/2002 - 12/2004

USPAS Participations

YEAR	COURSES (INSTRUCTORS)
2001/Winter	Accelerator Fundamentals (undergraduate) (Michael Syphers)
2002/Winter	Accelerator Physics (Gerald Dugan)
2003/Summer	Accelerator Physics (S.Y. Lee)
2004/Winter	Classical Mechanics and EM for Accelerators and Beams (Helmut Wiedemann)
2004/Summer	The SNS - I, Front End and Linac (Thomas Wangler and James Billen)
2004/Summer	The SNS - II, Ring and Transport Systems (Jie Wei and Yannis Papaphilippou)
2005/Winter	Advanced Beam Dynamics (Bruce Carlsten and Steve Russell)
2005/Winter	Computational Methods in Beam Dynamics (Robert Ryne)
2005/Summer	Computational Methods in Electromagnetism (Kwok Ko and Zenghai Li)
2006/Winter	High Current Beam Physics in Induction Accelerators (George Caporaso and Yu-Jiuan Chen)
2006/Winter	Fundamentals of Ion Sources (Ian Brown and Xavier Godechot)
2006/Summer	Beam Physics with Intense Space Charge (John Barnard and Steven Lund)
2007/Winter	Collective Effects and Wakefields (Roger Jones)
2007/Winter	Modern Computational Accelerator Physics (Panagiotis Spentzouris and James Amundson)
2007/Summer	Beam Experiments and Measurements at the NSCL (Marc Doleans, Guillaume Machicoane, Walter Hartung, and Eduard Pozdeyev)
2007/Summer	Fundamentals of Low-Beta Linear Accelerators with Simulation Lab (John Staples and George Gillespie)
2008/Winter	Synchrotron Radiation and Free Electron Lasers (Kwang-Je Kim, Yin-e Sun, and Zhirong Huang)
2009/Winter	Special Topics in Accelerator Physics (Alex Chao and Yunhai Cai)

Publications and Presentations

- **C.S. Park** and M. Hess “The Effects of Electromagnetic Space-Charge Fields in RF Photocathode Guns,” submitted to Nucl. Instr. Meth. A.
- M. Hess and **C.S. Park**, “Exact Space-Charge Field Solutions for Beam Currents in a Circular Conductor Pipe,” submitted to Phys. Rev. ST Accel. Beams.
- **C.S. Park** and M. Hess, “Time-Retardation Effect Causing Beamloss in the RF Photoinjector,” in PAC’09 proceedings.
- M. Hess and **C.S. Park**, “A Dispersion Free Three-Dimensional Space-Charge Modeling Method,” in PAC’09 proceedings.
- **C.S. Park** and M. Hess, “Studies of Electromagnetic Space-charge Fields in RF Photocathode Guns,” in EPAC’08 proceedings.
- S. Y. Lee, J. Kolski, Z. Liu, X. Pang, **C.S. Park**, W. Tam, and F. Wang, “Low energy electron storage ring with tunable compaction factor,” Rev. Sci. Instrum. **78**, 075107 (2007)
- M. Hess and **C.S. Park**, “A Multislice Approach for Electromagnetic Green’s Function Based Beam Simulations,” in PAC’07 proceedings.
- **C.S. Park** and M. Hess, “Computational Requirements for Green’s Function Based Photocathode Source Simulations,” in PAC’07 proceedings.
- M. Hess, **C.S. Park** and D. Bolton, “A Green’s Function Based Space-Charge Field Solver for Electron Source Simulations,” Phys. Rev. ST Accel. Beams **10**, 054201 (2007)
- M. Hess and **C.S. Park**, L. Zhu, and D. Bolton, “Electromagnetic Green’s Function Based Simulations of Photocathode Sources,” in LINAC’06 proceedings.
- M. Hess and **C.S. Park**, “Advanced Electromagnetic Analysis of Electron Source Geometries,” in PAC’05 proceedings.
- J.-S. Chai, Y.-S. Kim, T.K. Yang, D.H. An, I.S. Jung, H.S. Chang, G.B. Kim, J.S. Kang, **C.S. Park**, M.G. Hur, B.H. Hong, S.S. Hong, S.W. Kim, M.Y. Lee, W.T. Hwang, J.H. Kim, H.H. Shim, W.Y. So, M. Sekiguchi, “Development and Status Report of Medical Cyclotron at KIRAMS,” in Cyclotrons’04 proceedings.

- **C.S. Park**, J.S. Kang, D.H. An, J.S. Chai, M. Sekiguchi, “Beam Dynamics Study of High Intensity Compact Cyclotron for Neutron Generator at KIRAMS,” in Cyclotrons’04 proceedings.